Chem. Rev. **2004,** *104,* 459–508

Quantum Chemical Studies of Intermediates and Reaction Pathways in Selected Enzymes and Catalytic Synthetic Systems

Louis Noodleman,*,† Timothy Lovell,†,‖ Wen-Ge Han,† Jian Li,‡ and Fahmi Himo§

Department of Molecular Biology TPC-15, The Scripps Research Institute, 10550 North Torrey Pines Road, La Jolla, California 92037, Johnson & Johnson Pharmaceutical Research and Development LLC, Welsh and McKean Roads, P.O. Box 776, Spring House, Pennsylvania 19477, and Theoretical Chemistry, Department of Biotechnology, Royal Institute of Technology, ALBANOVA, S-106 91 Stockholm, Sweden

Received August 11, 2003

Contents

1. Introduction 459
2. Methods and Models 461
   2.1. Electronic Structure Issues 461
   2.2. Construction of Active Site Models 463
   2.3. Geometry Optimization for the Ground State, Intermediates, and Transition States 464
   2.4. Representations of the Protein/Solvent Environment 464
3. Protein Tyrosine Phosphatases (PTPase) 468
4. Hammerhead Ribozyme 472
5. Click Chemistry 474
   5.1. Tetrazole Formation Catalysis by Bronsted Acid 474
   5.2. Zinc Catalysis 476
6. Manganese, Iron, and Copper Zinc Superoxide Dismutases 478
   6.1. MnSOD and FeSOD 479
   6.2. CuZnSOD 482
7. Nitrogenase 484
8. Iron–Oxo Mössbauer Parameters 492
9. Methane Monooxygenase 493
10. Ribonucleotide Reductase 496
11. Lipoxygenase 500
12. Summary and Outlook 503
13. Acknowledgments 504
14. References 504

1. Introduction

Metalloenzymes catalyze many difficult and critical reactions in biological systems.[1] The ability of these biological catalysts to perform these reactions under mild conditions with selectivity and stability of the catalytic center generally exceeds chemists' current capabilities in developing related synthetic catalysts. Of known proteins, about 40% contain metal ions based on recent analysis of the protein data bank (PDB).[2] Fe, Zn, Mn, and Cu are the transition metals that occur most frequently among the catalytic sites in metalloenzymes, and Mg is prominent among the nontransition metals.[1,2]

Fe has been implicated in early electron transfer going back to prebiotic processes of geological and perhaps biological significance, including the light driven generation of H_2 gas which could serve as reducing equivalents for organic synthesis, other direct oxidative or reductive reactions catalyzed by ferrous iron in water and by iron−oxo (or hydroxo) and iron−sulfur minerals, and formation of banded iron−oxo deposits.[3] For example, it has been shown experimentally that carboxylic acids can be generated by reduction of CO_2 by magnetite (Fe_3O_4) but not by Fe(II) in water alone.[4] Similarly, a stoichiometric reaction starting from FeS and H_2S generates FeS_2 (pyrite) and $HCOO^- + H_2O$ from bicarbonate (HCO_3^-).[5,6] Such stoichiometric reactions can be considered as precursors to catalytic reactions once a mechanism is found for regenerating the initial form of the catalyst.

Fe, Mn, and Cu are redox active and can bind to a variety of different ligands. In biological systems, metal ion oxidation states Fe(II,III,IV), Mn(II,III,IV), and Cu(I,II) are most prominent; the spin states of Fe and Mn are also variable, with high-spin mainly preferred.[1] In many dinuclear or polynuclear enzymes and related electron-transfer proteins, these metal sites can also be spin-coupled.[7] By contrast, Zn(II) is redox inactive, although its Lewis acid character allows it to participate in many reactions involving charge flow.[8] In some Zn−Fe and Cu−Zn enzymes, metal sites are linked electronically by bridging groups.[9,10] Mg(II) is a hard divalent cation with a strong affinity for water and phosphate coordination, and a catalyst for many hydrolysis reactions.[11] All of these metals, in the 2+ or higher oxidation states, can promote the acidification of H_2O and for Fe(III,IV), Mn(III,IV) of OH^- as well.[12] Some of the main ligand players on this stage are carboxylates (Asp,Glu), thiolate (Cys), imidazole (His), phenol (Tyr), and guanidinium (Arg), which are highly versatile. The first four can undergo protonation/deprotonation, while Arg can act as a cationic assistant to metal centers.[12] The role of Arg has been demonstrated in carboxypeptidase A, alkaline phosphatase, and liver alcohol dehydrogenase. We will see later in the section on protein tyrosine phosphatases

---

* To whom correspondence should be addressed. E-mail: lou@scripps.edu. Fax: +1-858-784-8896.

† The Scripps Research Institute.

‡ Johnson & Johnson Pharmaceutical R and D LLC.

§ Royal Institute of Technology.

‖ Present address: AstraZeneca R and D Molndal, SE-431 83, Molndal, Sweden.

10.1021/cr020625a CCC: $48.50

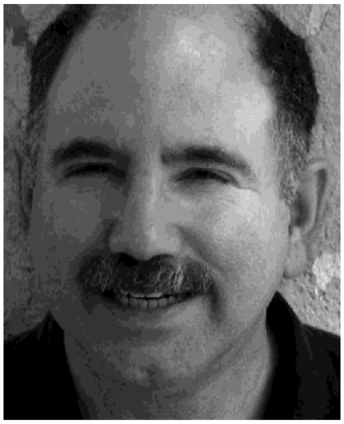

Louis Noodleman was born in Dayton, Ohio, (1950) grew up in Ohio and Virginia, and received his college education starting at Virginia Polytechnic Institute and then at the Massachusetts Institute of Technology (MIT), B.S., in Physics, 1971, and Ph.D. in Materials Science, 1975, with K. H. Johnson. He won the departmental John Wulff teaching award for graduate students at MIT. He conducted postdoctoral work at the University of British Columbia, Vancouver, Canada, as a Killam fellow with N. L. Paddock, and subsequently at the University of Washington, Seattle with J. G. Norman, Jr., in Chemistry, and with J. Bassingthwaighte, in Bioengineering, and at the Vrije Universiteit (VU), Amsterdam, Netherlands, with E. J. Baerends. He then spent one year as a visiting Associate Professor of Physics at the Centre d'Etudes Nucleaires, Grenoble and the University of Grenoble, France, in Bernard Lamotte's spectroscopy group. After returning to the U.S., he joined The Scripps Research Institute where he is currently an Associate Professor. He recently served on the Editorial Advisory Board of the *Journal of Bioinorganic Chemistry*. At the University of Washington and at VU, Amsterdam, he developed a connection between density functional theory and the theory of broken symmetry, which he and collaborators applied to iron–sulfur clusters and proteins. His current research interests include electron-transfer and proton-transfer energetics, reaction pathways in metalloenzymes, optical, Mössbauer, and ENDOR spectroscopy, magnetism in transition metal complexes, photochemistry, and click chemistry. He is interested in fundamental problems including the foundations of density functional theory, the correlation problem, and the uses of the broken symmetry and spin concepts in physics, chemistry, and biology. In his spare time, he and his wife Peggy enjoy playing with their daughter Julia and watching her draw.

that Arg can promote catalytic activity independent of metals as well when assisted by Asp, Cys, and other amino acid residues acting in concert. Carboxylates and coordinated water or hydroxyl can also show considerable geometric flexibility.[13] Cysteine thiolate is a soft ligand due to the sulfur, which exhibits strong covalency and charge transfer particularly with Fe.[7,12] Cysteine can be in the anionic or neutral (protonated) form. Like tyrosine, Cys can form radicals in some cases.[14,15] An unusual example of versatility is observed in the enzymes galactose oxidase and cytochrome *c* oxidase, where tyrosine side chains at the active site are modified by covalent linkage to the cysteine and histidine side chains, respectively.[15a−d] This covalent linkage, in conjunction with coordination to the metal ion (Cu(II)), may modulate the energetics of tyrosine radical formation during the catalytic cycle.[15a−d]

Our goal in this review is to develop some general themes for catalytic reaction pathways in enzymes and synthetic systems via several examples, relating electron transfer, proton transfer, and charge flow to energetics and structural transformations. Most of the examples will be drawn from reactions of metalloenzymes, but we will also examine a single nonmetal containing enzyme (protein tyrosine phosphatase), a hydrolytic ribozyme (hammerhead ribozyme where the catalytic center is an aquated Mg(II) ion), and Lewis acid- and Bronsted acid-catalyzed synthetic reactions utilizing click chemistry. In both enzymatic and effective synthetic catalysts, the match between substrate and catalyst leads to both control and reactivity.

In click chemistry, the substrates are selectively reactive because they possess particular common

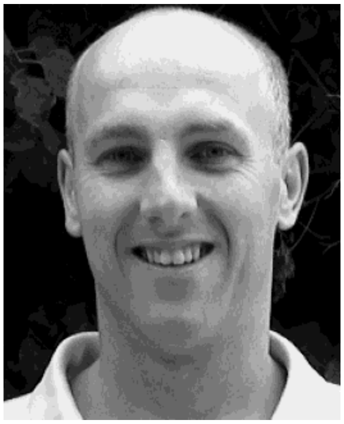

Prior to and during his undergraduate education, Timothy Lovell aspired, and still does, to be a professional golfer. After completing his undergraduate degree in Chemistry at Bath University (U.K.) with Robert J. Deeth, he was awarded an E.P.S.R.C. (U.K.) overseas scholarship to travel to the Australian National University in Canberra, where he obtained his Ph.D. in computational chemistry under the supervision of Robert Stranger. He then spent 5 years at The Scripps Research Institute (USA) with Louis Noodleman and David A. Case, and later, also with Ruben A. Abagyan. Consequently, his research interests at Scripps have been broad and various, encompassing quantum chemistry, and catalysis in biology, organic chemistry, and organometallic chemistry, as well as a recent expansion into computational biology, bioinformatics, and structure-based drug discovery. His most current appointment is in the department of computational medicinal chemistry at AstraZeneca's research center of excellence in Mölndal, in southern Sweden. When not involved in research and spending time with his family, Koko, Ami, and Hugo, he is honing his golf skills in preparation for an assault on the U.S.P.G.A. Senior tour.

Wenge Han (B.S. in Applied Physics, and M.S. in Solid State Physics from Tianjin University, P. R. China, and Ph.D. in Biophysics from University of Heidelberg, Germany) did her doctoral research with Professor Sándor Suhai at the German Cancer Research Center on biomolecular systems using ab initio, DFT, and QM/MM methods. She joined Professor Noodleman's group in 1999 as a postdoctoral research associate. She has worked on the active site property studies for Mn- and Fe–SODs, MMO intermediate state Q, and RNR intermediate state X. She has also worked on the theoretical study of photoexcitation and emission properties of solvatochromic dyes.

Jian Li was born in Guangdong, China. He studied chemistry and obtained his B.S. and Ph.D. at Peking University (with Guang-Xian Xu and Min-Bo Chen). After 2 years as a young faculty member at Peking University, he was awarded an Alexander von Humboldt Fellowship to work at the University of Hanover, Germany (with Karl Jug), and a NSERC Fellowship to work at the University of Calgary, Canada (with Tom Ziegler). He spent another year to study relativistic quantum chemistry at the University of Helsinki, Finland (with Pekka Pyykko). He joined the Scripps Research Institute and worked in the laboratory of David A. Case and Louis Noodleman on theoretical study of metalloproteins. He moved to pharmaceutical industry, first with the Texas Biotechnology Corp. and currently with Johnson & Johnson Pharmaceutical Research and Development L.L.C. as a Senior Scientist. His interests have varied over the years from quantum chemical calculation of organometallic compounds, to theoretical study of metalloproteins, to computer-assisted drug discovery.

Fahmi Himo received his undergraduate degree in physics from Stockholm University. In 2000, he graduated from the same university with a thesis entitled: Quantum Chemical Studies of Radical Enzymes. This work was supervised by Per Siegbahn and Leif Eriksson. He then spent 2 years as a Wenner-Gren postdoctoral fellow at the Scripps Research Institute in La Jolla, California, working with Louis Noodleman, David Case, and Barry Sharpless. He is currently working as an assistant professor at the Royal Institute of Technology in Stockholm, Sweden. The main theme of his research is catalysis. High-level quantum chemical methods are used to study problems in enzymatic and organometallic catalysis.

functional groups, so that certain metal ions in solution (and other Lewis acids) are effective catalysts. These multiply bonded substrates are largely unreactive in most biological systems unless the protein cavity has a shape that is highly complementary to the assembled substrates. Because many derivatives of the two combining reactants can be prepared synthetically, both appropriate reactivity and high selectivity become feasible. Both in vivo and in vitro applications have been realized.

There are a number of general themes in this review: (1) Where and how does proton transfer facilitate bond cleavage, and how is this linked to charge transfer? (2) How are electron transfer and proton transfer coupled or gated? (3) How do the catalytic metal sites and amino acid residues provide orientation and guidance for the substrate along reaction pathways? (4) What are the comparative roles of active site flexibility versus rigidity, and how do these and related factors affect mechanism? When is flexibility important, and when is it counterproductive? What are the roles of substrate and protein strain? (5) What are the important protein environmental influences from the first coordination shell, second (or third) coordination shell, and the more extended protein/solvent environment? What are the "sensitive features" of the coordination environment that can account for effective or ineffective catalysis?

We will analyze reaction mechanisms in some detail for a number of illustrative examples; however, we will not be comprehensive in covering metalloenzyme catalysis because there are excellent reviews on related subjects, particularly on radical enzymes.[15d−f] Our group has also written a number of recent reviews covering the electronic structure, properties, and energetics of iron−sulfur proteins,[16,17] structural, energetics, and reaction path issues for a number of metalloenzymes,[18] and applications of density functional theory.[19] In the specific areas of this review, we will focus on newer developments in these fields while trying to maintain coherence with important earlier work and fundamental concepts. Also, for many of the systems we will discuss, the catalytic reaction pathways are only partially understood, and certain steps are missing or possess uncertainties. There is considerable scope for further theoretical and experimental work on all of the systems analyzed here.

The main subjects are: (1) protein tyrosine phosphatases, nonmetal containing enzymes which hydrolyze tyrosine phosphate monoesters; (2) hammerhead ribozyme, which hydrolytically cleaves a phosphodiester backbone in RNA; (3) click chemistry, where Zn, Lewis acids, or Bronsted acids catalyze ring formation from multiply bonded precursors (azides, nitriles, and acetylenes); (4) MnSOD, FeSOD, and CuZnSOD which dismute superoxide to molecular oxygen and hydrogen peroxide; (5) the nature of the catalytically active site and the reaction pathways of the nitrogenase MoFe protein, where dinitrogen is reduced catalytically to ammonia; (6) intermediates of iron−oxo dimer enzymes (MMO, RNR); and (7) the reaction pathways of lipoxygenase, which are a class of Fe-containing enzymes that catalyze the hydroperoxidation of fatty acids.

2. Methods and Models

2.1. Electronic Structure Issues

The principal computational tools used here are density functional theory (DFT) methods either with the hybrid (B3LYP) potential[20] or with "pure" DFT (typically these are of generalized gradient approximation (GGA) type) exchange-correlation potentials, particularly Becke−Perdew86 (BP86)[21,22] or Perdew−Wang91 (PW91).[23] We have also used the more rapid local VWN−Stoll[24] exchange-correlation potential productively in the PTPase work, calibrating reaction energies there versus B3LYP, PW91, and MP2.[25]

Hybrid potentials (of which B3LYP is one example) are derived from a total energy equation where the exchange-correlation energy is a linear combination of the Hartree−Fock exchange energy and "pure" DFT-GGA exchange and correlation energies.[19−26] The coefficients of these terms are typically determined from fits to thermochemical data. Application of the variational principle yields a set of mean field one-electron equations giving finally one-electron energies and orbitals as well as the corresponding self-consistent-field (SCF) potential(s). These SCF potentials are orbital dependent for hybrid potentials, while for "pure" DFT-GGA methods, all one-electron orbitals with the same spin share the same SCF potential. However, the SCF potential for α spin electrons can be different from the SCF potential for β spin electrons. For a discussion of both the fundamental and the practical aspects of using DFT methods, we refer to a very extensive literature.[19,26]

We want to concentrate on a few significant points. DFT methods can be used for calculations on large systems with good accuracy for structures, properties, and energetics.[19,27] This applies even to transition metal complexes,[18,19,27−29] and the typical quantitative accuracy of these methods is often quite good for identifying and systematizing important energetic features of metal-containing enzymes, and for distinguishing feasible versus unlikely reaction pathways. A rough rule is to expect reaction energies and barriers intrinsically accurate to about 2−5 kcal/mol for B3LYP and somewhat larger for GGA-DFT (BP86, BLYP, PW91, BPW91).[19,28] Reaction energies and barriers for transition metal complexes typically involve bond making or breaking of only a few bonds, or reorganization of noncovalent interactions, which can also be reasonably strong. Typical barrier or reaction energies are often 0−50 kcal/mol; these are much less than total atomization energies, or dissociation energies for the complex as a whole, and so are the expected errors. Very often, the construction of the quantum mechanical model cluster (i.e., deciding what to include or exclude from the cluster), and finding a good representation of the surrounding protein and solvent environment, or solvent and counterions for synthetic systems, is equally important. Further, for transition metal complexes, the basis set must be of high quality, at least double or triple ζ plus polarization on the metal, and double ζ on the ligands.[30]

Many transition metal complexes have high-spin (HS) metal sites, and spin-polarized methods are required with different SCF potentials for different spin. These distinguish between the orbitals and corresponding electron densities of the α (spin-up) versus β (spin-down) electrons, and the one-electron energies ϵ_i for the orbitals are also spin dependent.[16] These electronic spin polarization effects can be very large when there are high-spin metal sites (as in many Fe and Mn enzymes) and can profoundly change the energy level scheme as confirmed by photoelectron and optical spectroscopies.[31] The α versus β densities may be different either locally or globally. For high-spin states of the molecule as a whole, a single simple spin unrestricted DFT calculation may suffice: this covers a single spin-polarized metal site, or a number of parallel spin sites including spin delocalization to ligands. However, dinuclear and polynuclear transition metal complexes are often antiferromagnetically (AF) coupled, and metal−ligand radical complexes can also be spin-coupled.[16,18] In this case, the AF-coupled state is represented by a "broken symmetry" (BS) state, where the α and β electron densities occupy different regions of space, and the spin sites are oppositely aligned. The energy and properties of the BS state can then be compared to the corresponding HS state where the spin vectors of the sites are parallel aligned, also called the F (ferromagnetically coupled) state. For a Heisenberg exchange coupling Hamiltonian of the form, $H_{\text{spin}} = -2J\boldsymbol{S_1}\cdot\boldsymbol{S_2}$, the energy difference between the HS and BS states is

$$E(\text{HS}) - E(\text{BS}) = -4JS_1S_2 \qquad (1)$$

This differs in general from the corresponding difference between the HS state (total $S = S_t = S_{\max}$) and the pure low-spin state (total $S = S_t = S_{\min}$), because the BS state is not a pure spin state, but is instead a specific weighted average of the pure spin states. Further, from the energy difference $E(\text{HS}) - E(\text{BS})$, the Heisenberg coupling parameter J can be calculated and used to generate the entire spin state ladder, which lies between $S_{\min} = |S_1 - S_2|$ and $S_{\max} = |S_1 + S_2|$ in integer intervals. The relative energy of each pure spin state $E(S_t)$ is given by

$$E(S_t) = -JS_t(S_t + 1) \qquad (2)$$

All of the results above apply in the "weak coupling regime" which is typical for dinuclear and polynuclear F- or AF-coupled complexes. Further, the results above are readily generalized to polynuclear spin-coupled complexes; in that case, there may be several different BS states to consider, representing different spin alignments, and replacing a far larger number of pure spin states of the spin-coupled system.

We note also that the individual metal site spins can also be variable, ranging from HS to intermediate-spin (IS) or low-spin (LS), depending on the ligand field and other electronic influences, which changes the quantum numbers S_1, S_2. The total system energy difference between high-spin and broken symmetry states (or between the high-spin and "true" AF-coupled $E(S_{\min})$) can be a chemically significant quantity, of order 2−16 kcal/mol for oxo, hydroxo, or water bridged Fe(III)−O−Fe(III), or Fe(IV)−O−Fe(IV), and this can have important implications for reaction pathways.

The phenomenon of valence delocalization introduces additional complexity in mixed-valence dimers, or for mixed-valence pairs of sites in polynuclear complexes, when the site geometries are similar and the metal site energies are nearly equal.[27] For each of the states of the Heisenberg spin ladder, there is then an additional resonance delocalization splitting term, which is linearly dependent on the total dimer spin (S_{12}) of the mixed-valence pair, as $B(S_{12} + {}^1/_2)$. The energy of bonding or antibonding electron delocalization is dependent on the spin alignment of the mixed-valence pair. This phenomena, called “resonance delocalization coupling” or “double exchange” or “spin-dependent-electron-delocalization”, occurs often in polynuclear complexes, particularly of 3Fe4S and 4Fe4S type where there are mixed-valence pairs of Fe sites. It is more rare in dimers, but a number of cases have been spectroscopically confirmed. For the large $MoFe_7S_9X$ supercluster in the nitrogenase catalytic site, the current evidence supports some delocalization over multiple sites, but probably less than in 4Fe4S complexes. Additional studies are needed here in view of the newly discovered central ligand X. The identity of ligand X and the oxidation states and reactions of the MoFe superclusters will be analyzed later.

2.2. Construction of Active Site Models

Active site models include at least the first coordination sphere for the metal site and often considerably more within the “quantum cluster” region. The problem of full geometry optimization is briefly analyzed below. Performing partial geometry optimization is also quite feasible by related methods, either with some atoms frozen in Cartesian space, or by converting to internal coordinates, and then freezing appropriate internal degrees of freedom. There can be a number of reasons for doing this. Certainly, the size of the geometry optimization problem is considerably reduced; this saves computer time, and one may know that certain degrees of freedom will not change much. Another reason is that one may want to embed the quantum cluster in a more extended protein (or synthetic) environment, and so freezing certain atoms in a frame, or utilizing internal coordinate constraints, may be needed to be compatible with the surrounding protein atom framework (known experimentally, for example). These mixed constrained/free clusters are used frequently, and geometry optimization is entirely feasible.[32] While the forces in the unconstrained directions are zero at extrema, the forces in the constrained directions are ill-defined, and therefore obtaining frequencies, and clearly identifying minima versus transition states, is not feasible by frequency calculations. Another way of getting at transition states and reaction paths is to use linear transit methods between minima to obtain approximate saddle points, and then to refine these where needed by detailed transition state searching (see below).[33] Alternatively, one can start by guessing the position of transition states lying between selected intermediates. This guess is often based on the extended Hammond postulate which says that the transition state of a reaction is closer in the position of its reaction coordinate to the (initial or final or intermediate) state having the higher energy.[34] The Hessian matrix is defined as the matrix of second derivatives of the total energy with respect to the geometric coordinates and is highly geometry dependent. Because transition state searches require a good quality initial Hessian matrix, and are finally successful only when one finds the “right region” in the multidimensional conformational space, linear or quadratic transit methods are very useful. Also, all minima (or extrema, including saddle points, transition states) are determined by a “local” variational equation to obtain a zero value for the gradient vector (the gradient of the total energy with respect to geometry), and extrapolation is required, so searching by guess or transit paths is required in practice. The “local model” is usually a multidimensional quadratic function and cannot represent the true complexity of the potential energy (PE) surface. Further, the PE surface is typically more complicated near transition states than near intermediates.

The use of prior structural information is certainly valuable and often essential, where at least the “resting state” structure is available from medium or high-resolution X-ray crystallography.[35] In some cases, X-ray structures of intermediates or states complexed to inhibitors are available.[36] Also, spectroscopic evidence may provide valuable (partial) structural information where X-ray structures are absent and can complement and (even correct) X-ray structures in many cases.[37] All of these methods relieve the working scientist from the intractability of global searches for the lowest of multiple minima or multiple transition states in large molecules. Even a medium-sized molecule can have over 100 conformational minima connected by several hundred transition states.[38] Having protein structures of good quality (about 2 Å resolution) available solves for the minima of the “soft modes” in the protein conformational space and provides the extended protein/solvent framework in which to embed the active site transition metal complex or “quantum cluster”. Still it should be remembered that X-ray structures can have both some heterogeneity of structure as well as structural uncertainties.[39] The structure may correspond to a mixture of redox states, a mixture of protonation states, or a mixture of tautomeric or conformational states. There may be uncertainties about redox and/or protonation states as well.[18,19,37]

The question of whether the X-ray structure that is observed from the crystallized protein is the relevant “catalytically active” form of the protein is highly complex and very system dependent. We cite a few relevant examples to illustrate the possibilities. MnSOD and FeSOD are found either in dimeric or in tetrameric form.[40] The dimeric interface between the A and B chains in these proteins contains a Glu−His hydrogen bond where the His is a ligand to the Mn or Fe. This appears to be very significant catalytically based on DFT/electrostatic redox potential calculations, and in accord with the common appearance of Glu−His−Metal and Asp−His−Metal motifs in metalloproteins.[41,42] Further, this dimer interface provides access to the O_2^- substrate to get near the active site pocket. In other cases, the X-ray crystal structure may display highly interesting, although nonphysiological, interactions, even fairly close to the active site transition metal complex. A very recent example is a very-high resolution (1.3 Å) structure of the water-soluble Rieske iron−sulfur protein fragment from a thermophilic eubacterium expressed in

E. coli.[43] The A and B molecules, each containing an $(Cys)_2FeS_2Fe(His)_2$ cluster, display H-bonding of shared protons between the His ligands from each molecule. By contrast, the full cytochrome bc_1 complex is still a dimer, but it is enormous.[44] Each half contains two heme *b* centers and a heme c_1 center in addition to one Rieske protein. Here, the Rieske iron−sulfur centers do not contact one another during the physiological redox and proton pumping cycle. Instead, they H-bond to hemes and/or to ubiquinones, and the Rieske protein fragments are evidently highly mobile during the catalytic cycle. The full complex is embedded in a membrane, but with a water-soluble part as well, and the resolution of the relevant X-ray structure is not as high (3.5 Å). A third example is the X-ray structure of the hydroxylase component of methane monooxygenase. Here, the available protein structures are of medium resolution (about 2 Å).[45,46] This resolution is good enough to obtain a general layout of the active site diiron cluster with respect to the remaining protein, but not sufficient to define the protonation state(s) of the bridging solvent-based (water or hydroxyl or oxo) ligands. Here, optical spectroscopy and DFT calculations help to define the active site coordination environment.[47,48] A general problem, cited in all of this literature, is the movement of protein side chains, which may or may not have a unique conformation within an X-ray structure. Here again, spectroscopy and quantum chemical calculations may help to sort out the problem. Also, solvent molecules may enter or leave the active site (or change protonation states), and these can play a mechanistic role. While medium-resolution X-ray structures (about 2 Å) are often adequate for constructing reasonable active site models and including the remaining protein environment, very-high-resolution structures (1.3 Å or lower) are highly desirable, particularly if the state in the X-ray structure can be closely monitored by spectroscopy.

Another point to remember in some mixed quantum/classical electrostatics models is that when the model of the surrounding environment allows for the evaluation of interaction energies but does not include analytic gradients, frequency calculations and precise transition state searches cannot be done. However, approximate transition states can be found by linear transit and related two-dimensional grid searching, and these can be quite valuable (see the discussion of Poisson−Boltzmann models in section 2.4).

2.3. Geometry Optimization for the Ground State, Intermediates, and Transition States

If the quantum cluster is not too large, it is often feasible to perform full geometry optimizations on the ground state, intermediates, and transition states.[49] One finds where the gradients of the potential energy surface are zero (that is, the forces are zero). Most DFT programs can calculate energy gradients analytically, but analytic second derivatives are not available. Instead, an approximate inverse of the Hessian matrix is constructed and updated, particularly by the BFGS (Broyden−Fletcher−Goldfarb Shanno) method.[50] In the Newton method, the quadratic function approximating the potential energy surface is used to extrapolate the point where the gradient vector will be zero. Because the quadratic model surface is only an approximation to the actual surface, and because the Newton method requires analytic second derivatives, more flexible quasi-Newton methods are typically used.[50] In quasi-Newton methods, the energy minimization is performed along a line between the current and previous point, and after the approximate inverse Hessian is updated, the inverse Hessian matrix and gradient vector are used to take the following step, possibly with a smaller step size than in the Newton method. If convergence in the gradient and geometric displacement is not obtained, this process is performed iteratively.

Frequency calculations can be used to confirm that the ground state and intermediates are true minima within the framework of the Born−Oppenheimer surface of energy $E(\{R_j\})$ versus geometry $\{R_j\}$ (where $\{R_j\}$ denotes the set of nuclear position coordinates $j = 1,....,M$ for M nuclei), and because the Hessian (converted to the equivalent mass-weighted coordinate force constant matrix F) is positive definite for minima (after diagonalization), all eigenvalues λ from the equation[51]

$$|F - \lambda I| = 0 \tag{3}$$

are positive, and the normal-mode frequencies $\nu(i)$ (also positive) are given by $\nu(i) = [\lambda(i)]^{1/2}/2\pi$. This matrix equation has exactly one negative eigenvalue $(\lambda(k))$ for transition states corresponding to a first-order saddlepoint and to one imaginary normal-mode frequency $\nu(i) = [\lambda(i)]^{1/2}/2\pi$ for the normal mode $i = k$ along the reaction coordinate, the other frequencies remaining positive as before. The vibrational zero-point energy is an important contributor to a number of phenomena. The zero-point energy is particularly important for deprotonation energies,[52] but also proton-transfer energies and barriers, proton tunneling, and kinetic isotope effects both for protons and for heavier atoms.[34,53] This energy is simply

$$E_\nu(T = 0) = \sum_i (^1/_2)h\nu(i) \tag{4a}$$

More generally, the temperature-dependent vibrational energy is

$$E_\nu(T) = \sum_i (\langle n_i \rangle + {}^1/_2)h\nu(i) \tag{4b}$$

where the sum is over the normal modes i, and where $\langle n_i \rangle$ is the mean excitation of the vibrational harmonic oscillator of mode i, given by Bose−Einstein statistics

$$\langle n_i \rangle = 1/(e^{h\nu(i)/kT} - 1) \tag{5}$$

2.4. Representations of the Protein/Solvent Environment

There are several ways to represent the protein and solvent environment, which differ in assumptions, accuracy, and ease or difficulty of computation. The models and related problems include the following:

(1) Gas-Phase Calculations with or without Constraints. A “large enough” quantum model system is then needed. The choice of a physically realistic quantum model system becomes more difficult if the active site quantum cluster has a net charge or is quite polar (for example, having charged parts).

(2) Stability and Convergence. Many active site complexes in electron-transfer proteins and enzymes are multiply charged anions. Dinuclear and polynuclear iron−sulfur clusters are the clearest and most dramatic examples, because these are often multiply charged ($Fe_2S_2(SR)_4{}^{2-,3-}$, $Fe_4S_4(SR)_4{}^{2-,3-}$ and simpler analogues $Fe_4S_4(X)_4{}^{2-}$, $X = Cl^-$, Br^-).[7] In this respect, they (and related synthetic complexes) share common features with “textbook” dianions and trianions $CO_3{}^{2-}$, $SO_4{}^{2-}$, $PO_4{}^{3-}$.[54] While all of these systems are stable in condensed phases, they are unlikely to be stable in the gas phase because of the strong electrostatic repulsion of the excess electrons. The strength of this repulsion from classical electrostatics is roughly proportional to $Q^2/2R$, where Q is the total cluster charge and R is the average radius, and this simple electrostatic contribution to the ionization potential (IP) in the gas phase becomes more negative as $(2Q + 1)/2R$ (where Q is a negative integer, representing the cluster charge prior to loss of an electron, and the numerator is in units of e^2 where e is the electron charge). Clearly, the cluster becomes more unstable to loss of an electron as the cluster becomes more negatively charged.[55] Such clusters in the gas phase are also often unstable to loss of a ligand, or in the case of Fe_4S_4 $(X)_4{}^{2-}$, $X = Cl^-$, Br^-, to symmetric fission into two equal dinuclear fragments, $2[Fe_2S_2X_2{}^-]$.[56] From the experimental photoelectron spectroscopy, the first IP of $Fe_4S_4(X)_4{}^{2-}$, $X = Cl^-$, Br^-, is near 1 eV (positive), so these states are stable. However, with less electronegative terminal ligands, $X = SCH_3{}^-$, our recent DFT calculations give an IP of nearly 0 eV (slightly negative), so this cluster is unstable (or possibly marginally stable). For the $Fe_4S_4(X)_4{}^{3-}$, $X = SCH_3{}^-$, cluster, we calculate IP = −4 eV, which is very unstable.[57]

It is surprising then that some multiply charged anions can be observed even when their measured ionization potentials are negative.[58] This has been seen by photodetachment photoelectron spectroscopy. It reflects the metastable character of these states. While one-electron loss is energetically favorable, the excess electron must surmount a repulsive Coulomb barrier arising from the outer shell of anions. Wang et al.[58] have studied the behavior of the copper phthalocyanate tetrasulfonate tetraanion in some detail $[Cu(II)Pc(SO_3)_4]^{4-}$; the electron binding energy is negative (−0.9 eV), while the repulsive Coulomb barrier of the outer $(SO_3)^-$ groups is positive (3.5 eV), so that the photoelectron kinetic energy exceeds the energy of the incoming photon by 0.9 eV. At photon energies below 3.5 eV, electron tunneling through the Coulomb barrier is seen. We raise these issues not only because of the increasing role of electrospray ionization of large systems which can be combined with photoelectron spectroscopy detection. These metastable states also have computational analogues as demonstrated by Stefanovich and co-workers.[59] They have shown that negative ionization potentials can be calculated for a number of small multiply charged anions in the gas phase even with IPs as negative as −5 or −6 eV. These states are greatly stabilized in solvent, giving positive IPs in water. We have made and reported similar calculations on dinuclear and polynuclear iron−sulfur clusters over many years.[57,60] What then accounts for the ability to calculate these states, despite their instability toward loss of an electron?[61] The resolution to this paradox lies in the Coulomb repulsive barrier, and in the fact that the continuum orbital into which the excess electron must “leak” has to be represented by a set of very diffuse functions, equivalent to plane waves or augmented plane waves. Even quite good (but not perfect) basis sets cannot represent the continuum electron, and a metastable state confining the excess electron is constructed. The energy and charge distribution in this state are generally very reasonable, because after the solvation energy due to the solvent cage is included, the IPs in solvent are reasonably close to those seen experimentally.[57,59,60c] Solvent, counterions, or a protein environment rich in hydrogen bonds create a stabilizing environment while not changing the electron density in a major way.

Multiply charged anions do not, however, constitute the only stability problem for transition metal active sites. DFT calculations on active site cluster models, whether having a net positive or net negative charge, are susceptible either to oscillations and/or to giving an incorrect ground-state electronic structure in many cases unless care is taken and the physical origin of the problem identified. We will discuss two frequent problems that we have found in our recent calculations on FeSOD,[42] the 2Fe2S Rieske center,[62] and the FeMo cofactor center of nitrogenase.[63] During the self-consistent-field (SCF) process, it is easy for anionic side chains, particularly carboxylates and thiolates, to lose electrons to the metal ion (for Fe(III), in particular) and produce ligand radical states. These can appear to be the ground state even when they are not according to a proper test of total energies of alternative states. This problem often occurs when the cluster model does not contain the H-bonds to the side chains stabilizing the anionic form of the ligands. The cluster model can then be expanded to include the required H-bonds. Alternatively, level-shifting and orbital following procedures can be used to force the “hopefully correct” electronic structure for the SCF ground state. After one has found an SCF solution for one electronic state (corresponding to one specific orbital occupation scheme), the total energy of this state can be compared to those for alternative electronic states (corresponding to different orbital occupancies), and then the “correct ground state” can be determined at least for the specified exchange-correlation potential used. Orbital level shifting is usually turned off as self-consistency is approached to test the stability of the “trial electronic ground state” as compared to others. However, this procedure sometimes leads to renewed oscillations between electronic states. The “correct ground state" may well have some empty one-electron energy levels which lie below the filled energies, giving a "non-Fermi" occupation scheme. It becomes important to recognize when this is occurring, and how to deal with this problem in general.

This second problem of oscillations between filled and empty levels has its origin in the way energy levels are ordinarily filled within the SCF scheme in density functional calculations. It is typical and convenient to use the "aufbau" or building principle, which implies that the one-electron energy levels (derived from the solutions of the Kohn−Sham equations for a given exchange-correlation potential) are ordered by increasing energy, and filled in that order with integer occupation numbers (1 or 0 for occupied or empty spin−orbitals). However, the difference in orbital energies between an occupied and an empty orbital ϵ_j ($n_j = 0$) − ϵ_i ($n_i = 1$) (where n_i, n_j are occupation numbers for the active initial and final orbitals (i,j) of the excitation) can be a poor approximation to the one-electron excitation energy between states if the orbitals have very different spatial extent. A very good approximation to the total energy difference for a one-electron excitation is the Slater transition state energy,[64] defined as ϵ_j ($n_j = {}^1/_2$) − ϵ_i ($n_i = {}^1/_2$), with all other occupation numbers unchanged. If two energy levels are close and/or oscillating with changes in occupation numbers, the Slater transition state energy can be computed. This value will report which electronic state has the lower energy with good reliability and is stable against state-to-state oscillation because both orbitals have equal occupation numbers. The major case where this problem occurs is when an empty metal d orbital is close in energy to a filled ligand orbital (or conversely). The ϵ_j for that metal level (being the more localized) then drops substantially when the orbital is empty and rises substantially when it is filled, while the more delocalized ligand level ϵ_i (n_i) changes much less. The Slater transition state is also a good "halfway point" for trying to converge and compare different SCF states. It can then be followed by level shifting with more confidence that the "correct levels" are being shifted away. Our group prefers this approach to "orbital smearing" using variable occupation numbers, where the physical meaning is much less clear despite its utility.[49b] State crossings or near avoided crossings between different electronic states can occur with variations in molecular geometry as well.[65] For example, a "ligand radical state" with a reduced metal ion may lie close to the "ligand anion state" with an oxidized metal ion.[66] In "valence tautomeric complexes", these distinctive electronic ground states may each occur under different conditions of temperature and pressure due to their differing entropies and volumes. A proper physical analysis of these problems should include an assessment of spectroscopic properties as well as geometries and energies because the electronic states can be very close to one another.[29]

(3) Inclusion of an "Average" Polar Environment Using a Continuum Solvation Model, Treating Interaction Energies Either at the Single Point Quantum Level (after the "Gas-Phase" Geometry Optimization on the Quantum Cluster) or with Subsequent Geometry Optimization Including Solvation. One of the most popular models of this type is COSMO (conductor like screening model for two dielectric media, quantum cluster plus solvent),[67] which has good accuracy for polar solvent media, when the quantum cluster charge and polarity is not too high. The protein and solvent are not explicitly represented; rather an average dielectric constant is chosen for the dielectric medium. COSMO starts from a solvent model with a dielectric constant ϵ equal to infinity, and then rescales this back to a finite dielectric using a well-known rescaling formula: $f(\epsilon) = (\epsilon - 1)/(\epsilon + x)$. The variable x is adjustable: for a finite charge in a spherical cavity, $x = 0$, while for a dipole in a cavity, $x = {}^1/_2$. For large ϵ, x becomes much less important, and COSMO is most accurate for large ϵ in any event. One great advantage of COSMO is that geometry optimization can be performed with COSMO as a part of the potential, and this option is available in a number of computer programs, including Gaussian and ADF.[49]

(4) Poisson−Boltzmann-Based Models. These models are used to represent the energetic interaction of the active site with the protein and solvent. They can be used as "classical electrostatic models",[68] but we will discuss their use in combination with quantum models for the active site.[25,60b]

The goal is to derive potentials at the active site and corresponding interaction energies with the active site cluster by solving the linearized Poisson−Boltzmann equation, which takes the form:

$$\nabla\epsilon(r)\nabla\phi(r) - \epsilon(r)\kappa^2\phi(r) = -4\pi\rho(r) \qquad (6)$$

Here, κ is the inverse salt-screening length, which is a function of ionic strength in the solvent region. (The simpler Poisson equation is obtained for $\kappa = 0$.) The charge distribution $\rho(r)$ constitutes the source, and for any such distribution and spatial variation of the dielectric constant $\epsilon(r)$, the corresponding potential $\phi(r)$ throughout space can be determined by finite difference methods on a grid. The complete system is divided into a "quantum cluster" and "the environment". The total system is partitioned into three regions with different charge distributions and dielectric properties: a high dielectric constant is used for the region of bulk solvent ($\epsilon_s = 80$ for water), a lower dielectric constant is used for the protein region (typically $\epsilon_{\text{protein}} = 4$ to represent both electronic polarizability and some internal polarization within the protein, as expected for side-chain and main-chain motions responding to charges), and a vacuum dielectric constant $\epsilon_{\text{cluster}} = 1$ is used within the active site cluster, because the cluster is represented quantum mechanically. The protein region contains a partial charge representation of the protein derived from force field or solvation models in the literature. For the quantum cluster, an electrostatic potential (ESP) due to the total charge distribution is constructed in a medium field region outside a van der Waals envelope surrounding the cluster, but within a given range (typically 5 Å from any atom). For the electrostatic target potential, a set of "best fit" charges, called the ESP charges, are then found which best match the target potential.[52,60c,69] Starting with the cluster ESP charges as the source, the total potential is calculated $\phi_{\text{dielectric,cluster}}$. However, part of this is just the vacuum Coulomb potential $\phi_{\text{vac,Coul}}$, which is already included in the gas-phase Hamiltonian. The dielectric response potential to the cluster charges is then $\phi_{\text{react}} = \phi_{\text{dielectric,cluster}} - \phi_{\text{vac,Coul}}$. By contrast, the potential due to the protein charge distribution ϕ_{prot} contains also its Coulomb potential because the protein charges act on the cluster charge distribution.

For the combined DFT-PB method, the simplest model is the single step rigid charge model.[17] Here, all of the generating charges are point charges (either cluster ESP charges or protein charges) and the total interaction energy is calculated as the sum of the reaction field and the protein field energies $E_{\text{pr}} = E_{\text{react}} + E_{\text{prot}}$.

$$E_{\text{pr}} = {}^{1}/_{2}\sum q_i^{\text{ESP}}\phi(r(i))_{\text{react}} + \sum q_i^{\text{ESP}}\phi(r(i))_{\text{prot}} \quad (7\text{a})$$

The sum is over all cluster point charges at their respective atom centers (nuclei). The first term is the cluster reaction field energy due to the interaction of the cluster charges with their own polarization response throughout the three dielectric regions. The second term is the protein field energy which is the dielectric screened Coulomb interaction energy between the protein charges and the cluster charges. The first term contains the factor $^{1}/_{2}$ which accounts in the framework of linear response theories (including linearized Poisson−Boltzmann) for the work of polarizing the linear dielectric media.

In the more complete self-consistent-reaction-field (SCRF) method, the full electron density distribution is used in quadratures, and the reaction-field potential produced by the cluster charges is iterated to self-consistency along with the quantum electron density (and its ESP charge representation).[25,52,60b,70] The total interaction energy E_{pr} can be partitioned into three terms:

$$E_{\text{pr}} = E_{\text{prot}} + E_{\text{react}} + E_{\text{strain}} \quad (7\text{b})$$

The first two terms have meanings similar to those in the simpler rigid charge model, but now use final self-consistent charge densities and potentials and proper quadratures. The final term E_{strain} is new and represents the “electronic strain” or energy cost for shifting the cluster electron density from its “gas-phase” value. SCRF methods strongly stabilize anions (and their energy levels) due to solvent and protein interactions.

One major advantage of Poisson−Boltzmann (PB)-based methods is that a statistical mechanical evaluation of the protonation state of the various titrating residues of the protein versus pH can be carried out prior to a quantum mechanical calculation. Monte Carlo and related methods can be used to reduce the $(2)^N$ scaling of this problem when there are many (N) titrating sites.[71] Another advantage, which also carries over into the combined QM−Poisson−Boltzmann methods, is that the protein field interaction energy with the quantum cluster can be partitioned into terms from the individual protein residues (or into main-chain versus side-chain terms) when the linearized PB equation is used. This greatly facilitates energy analysis and has been used extensively for designing calculations with larger quantum clusters from prior calculations with smaller QM regions plus an electrostatic PB representation of the remaining protein/solvent. The QM-electrostatic region boundary is typically represented using a link atom approach, similar to that often used in QM-molecular mechanics (see below). For both QM-PB and QM-MM, charge transfer across the boundary is not properly treated because this is intrinsically quantum mechanical in nature; Pauli repulsion between QM and PB or MM atoms is either omitted or treated with a simplified classical force field approach. However, combined QM-PB or QM-MM approaches are clearly more rapid than the equivalent fully quantum mechanical representation of the problem. For QM-PB, the dielectric constant for the protein region can represent both electronic polarization and orientational polarization, which roughly reflects protein dynamics, rather than a single structural minimum.

(5) QM-MM Method. An alternative approach to represent the protein and solvent environment is the hybrid quantum mechanical (QM)-molecular mechanical (MM) method.[72] Just like the continuum dielectric method described previously, this method partitions the whole system into two regions: an active region and the rest of the system. The active region includes a chemically active part such as the catalytic site of the enzyme and is treated with quantum mechanics. The rest is treated with an empirical force field. The whole system is described by a mixed Hamiltonian:[73]

$$H = H_{\text{QM}} + H_{\text{MM}} + H_{\text{QM-MM}} \quad (8)$$

H_{QM} represent the quantum mechanical Hamiltonian, and H_{MM} is the classical Hamiltonian. Various levels of quantum mechanical Hamiltonians can be applied, from semiempirical MNDO, AM1, PM3, and tight-binding, to Hartree−Fock (HF), post-HF, to density functional methods. H_{MM} takes into account bond stretching, bending, torsion, and van der Waals as well as electrostatic interactions. The $H_{\text{QM-MM}}$ term describes the coupling between QM and MM regions, which depends on the treatment of junction atoms and bonds. Several approaches have been developed to tackle this issue. The simplest way is introducing “link” atoms into the QM region to saturate the free valences of the junction atoms along the chemical bonds cut by QM-MM partitioning.[74,75] A more rigorous treatment is the hybrid orbital method in which the junction QM atoms are described by a set of hybrid orbitals and the ones pointing from the QM atoms to MM atoms are kept frozen during the SCF calculation.[76] This method can be implemented and generalized in different contexts.[77] A variant of the traditional QM-MM method is the effective fragment potential (EFP) method.[78] In this scheme, the Coulombic, induction, and repulsive interactions of the classical region are represented by an effective potential and are included in the quantum mechanical Hamiltonian. Furthermore, an ONIOM scheme has been proposed in which the single-layer QM/MM partition is extended to multilayer, and different levels of quantum mechanical Hamiltonian can be applied to different regions.[79,80]

One advantage of the QM-MM approach is that the computational effort can be focused on the active region of the system where quantum phenomena such as bond-breaking/bond-forming and electron/proton transfer occur, whereas the effects of surrounding environments are taken into account by fast but less accurate approaches. In this context, the geometry constraint from the protein environment to the active site cluster is automatically implemented during the geometry optimization step. The accuracy of the QM-MM calculation relies not only on the level of the quantum mechanical Hamiltonian, but also on the quality of the classical force field. Two of the shortcomings in many classical force fields are the point charge model for the electrostatic potential and the lack of polarization. Development of a polarizable force field[81] and integration of the electrostatic potential with a Poisson−Boltzmann (PB) or General Born (GB) model[82] are still the subjects of ongoing investigation. Nonetheless, the QM-MM method has been widely applied to study the solvation effect on protein structures[83] and the mechanisms of many catalytic reactions in solution phase or in protein environments,[84] and the results have been reviewed elsewhere.[85]

(6) Car−Parrinello Molecular Dynamics. The fluctuation of protein conformation and side-chain orientation has profound effects on the thermodynamics and kinetics of enzyme catalytic reactions. Traditionally, simulation of protein dynamics has been dominated by the molecular dynamics (MD) method based on the classical force field, which was hard to extend to the quantum region. Parametrization according to quantum mechanical calculations will provide reasonable force field parameters for the system under study.[86] In the core of the MD method is the calculation of forces acting on the nuclei for the propagation of the nuclear trajectories. The calculation can be easily done with classical molecular mechanics, but is prohibitively expensive with quantum mechanics for the larger systems such as proteins. Car−Parrinello molecular dynamics (CPMD), however, opened an avenue to carry out quantum MD simulation, especially under the density functional theory framework.[87] This was achieved by a revolutionary approach that solves the electronic wave function and the forces acting on the nuclei simultaneously. The approach is based on the fact that the variational principle is simply a minimization procedure and the parameters in the electronic wave function may be treated as similar to the other dynamical variables nuclear positions, in the Lagrangian. The electronic structure problem and the dynamics of the atoms are hence included in a set of Newtonian equations of motion and can be solved concurrently with the steepest descent method. In this way, the full dynamic time evolution of a structure is computed without resorting to a predefined potential energy surface (PES). The PES is calculated on-the-fly as the nuclear trajectory is generated. The implementation of CPMD was empowered by the pseudopotential approach using plane wave basis sets.[88]

CPMD has been applied to many systems including a wide range of biological systems such as metalloenzymes where the metal−protein interactions are hard to capture by a classical force field and the catalytic procedures involve bond-breaking and bond-forming, as well as proton and electron transfer. These applications have been reviewed thoroughly in several recent reviews.[89] Combining CPMD with QM-MM methods extends the horizon of CPMD simulation to more realistic complex systems.[90] Recent work from QM-MM CPMD simulations includes identification of the likely location of Cu^{2+} binding in proteins and the mechanism of cis−trans photoisomerization of the covalently bound chromophore in rhodopsin. The model system in the later study consists of chromophore, protein, and membrane mimetic environment, and the whole system is 24 000 atoms.[89a] However, many challenges still have to be met before the CPMD method can become as popular and powerful as the classical MD method.

3. Protein Tyrosine Phosphatases (PTPase)

Protein tyrosine phosphatases (PTPases) are enzymes central in regulating many cellular processes, particularly in response to extacellular signals.[91] PTPases are complementary in their function to protein tyrosine kinases, because in PTPases, a phosphate group is hydrolyzed catalytically from a tyrosine side chain, while in kinases, phosphate is added to the side chain.[92] A proper level and timing of tyrosine phosphorylation is critical for regulating cell growth, differentiation, metabolism, and progression through the cell cycle, as well as cell-to-cell communication and cell death versus survival.[93,94]

PTPases constitute a large and diverse superfamily of enzymes, which include both cytosolic and membrane-bound receptor enzymes.[93,95] The different subfamilies are diverse in sequence, molecular weight, and specificity (dual specificity enzymes can hydrolyze phosphoserine and phosphothreonine as well as phosphotyrosine), but there is considerable experimental evidence that PTPases exhibit a common mechanism with related common structural features.

Although these enzymes operate without metal ion cofactors, tyrosine phosphatases are extremely efficient enzymes, showing maximum catalytic rate constants (k_{cat}) 10 orders of magnitude greater than the corresponding rate constants for uncatalyzed hydrolysis of phosphate monoesters.[81] While there is general agreement about the mechanism of the uncatalyzed reactions, there is considerable dispute about the mechanism of the enzymatic reaction. We were drawn to the study of PTPases both because of their biological importance and because the proposed catalytic mechanisms based on theoretical and experimental studies displayed sharp contrasts.[25,96] Central to this dispute is the apparent high charge of the free substrate (a dianion) and the question of whether or how this charge persists (or is altered) first in the Michaelis complex, and then in forming the first stable intermediate. It is known that the reaction proceeds through a Tyr-phosphate-cysteine intermediate with a direct P−S bond. If the cysteine is a 1^- anion,[93] the reaction takes the form:

$$\begin{gathered}\mathrm{ES^- + ROPO_3{}^{2-} \rightleftharpoons [ES\text{--}PO_3OR]^{3-}} \\ \text{(Michaelis complex, Mechanism A)}\end{gathered} \tag{9}$$

$$\begin{gathered}\mathrm{ECOOH + [ES\text{--}PO_3OR]^{3-} \rightarrow} \\ \mathrm{ECOO^- + ESPO_3{}^{2-} + RO\mathit{H}} \\ \text{(formation of the phosphocysteine intermediate,} \\ \text{Mechanism A}\end{gathered} \tag{10}$$

Here, E denotes the single enzyme that contains both the relevant cysteine (S) and the aspartic acid (COOH), S^- is the catalytic cysteine thiolate side chain, and $[\mathrm{ES\text{- -}PO_3OR}]^{3-}$ is the Michaelis complex that is formed initially. $(\mathrm{OR})^-$ is the tyrosine anion $\mathrm{TyrO^-}$ which in the complete biological system is a residue within the protein that is the substrate for the reaction. Kinetic assays are often performed with simpler substrate analogues, particularly nitrophenyl phosphate. The second reaction shows that a conserved general acid (aspartate) protonates tyrosine to produce the neutral form (ROH), which is the leaving group. To complete the catalytic cycle, the final product results from hydrolysis of the $\mathrm{ESPO_3{}^{2-}}$ intermediate by water, giving

$$\begin{gathered}\mathrm{ESPO_3{}^{2-} + ECOO^- + H_2O \rightarrow} \\ \mathrm{ES^- + HPO_4{}^{2-} + ECOOH} \\ \text{(final hydrolytic cleavage of the phosphocysteine} \\ \text{intermediate}\end{gathered} \tag{11}$$

Reactions 10 and 11 above show the mechanism only in a broad sense: while analysis of the pH dependence of experimental kinetics and the theoretical electrostatics calculations of Dillet et al.[96] favor the charged forms indicated in these equations, Aqvist's group,[97] based on their theoretical/computational studies, have proposed the following alternative mechanism for formation of the first intermediate (Mechanism B)

$$\begin{gathered}\mathrm{ES^- + [ROPO_3H]^- \rightleftharpoons [ES\text{--}PO_3HOR]^{2-}} \\ \text{(Michaelis complex)}\end{gathered} \tag{12}$$

$$\begin{gathered}\mathrm{ECOOH + [ES\text{-}PO_3HOR]^{2-} \rightarrow} \\ \mathrm{ECOO^- + ESPO_3H^- + ROH} \\ \text{(phosphocysteine intermediate)}\end{gathered} \tag{13}$$

Mechanism B can be compared to Mechanism A, the important difference being that there is an early protonation of the substrate at a nonbridging phosphate oxygen at or before the formation of the Michaelis complex, and the proton added remains in the phosphocysteine intermediate. A closely related variant of this mechanism (Mechanism B′) assumes that the cysteine starts in the neutral form, and then transfers its proton to the substrate in the Michaelis complex.

$$\mathrm{ESH + [ROPO_3]^{2-} \rightleftharpoons ES^- + [ROPO_3H]^-} \tag{14}$$

After this, Mechanism B follows as discussed above.

As we shall see, the difference in charge between Mechanism A and Mechanisms B and B′ leads to very different reaction barriers and pathways. In the following analysis, we will focus on the formation of the covalent phosphocysteine intermediate rather than the final hydrolysis step. Depending on the specific enzyme studied, either of these can be the rate-limiting step, and both are biochemically significant, with the formation of the first intermediate constituting the first irreversible step of the reaction.

In a series of mechanistic studies, Aquist et al.[97] used the empirical valence bond method to examine the reaction mechanism of PTPases and concluded that mechanisms B and B′ are energetically most favorable. Mechanism B (or B′) does seem intuitively reasonable because the nucleophilic attack of the $\mathrm{CysS^-}$ anion on the phosphorus of the substrate should be easier if the substrate were a monoanion, as in Mechanism B, or after the activation step in Mechanism B′, as compared to the dianionic substrate of Mechanism A, where greater charge−charge repulsion would be expected. However, eqs 9 and 10 or eqs 12 and 13 alone do not uncover the actual sequence and timing of the proton transfer from the general acid to the tyrosine anion, or the role of other protein residues at or near the active site.

Gao and co-workers[98] used an AM1/MNDO semiempirical quantum mechanics treatment of thiolate, substrate, and general acid in the context of the protein environment to explore the reaction pathway, concluding in favor of mechanism A. The protein environment was described by molecular mechanics using the PARAM22 force field in CHARMM, so there was a significant representation of the surroundings. However, this group did not predict the protonation of the tyrosine anion that is needed for completion of the first half of the reaction.

Czyryca and Hengge[99] used a large quantum cluster of nearly 300 atoms to model the reaction pathway assuming Mechanism A with a PM3 semiempirical Hamiltonian. Their focus was on the structural transformation along the reaction pathway. They predicted a dissociative transition state for the formation of the intermediate. The phosphoryl transfer was predicted to be concerted, but with a "very loose" transition state, and where the bond-breaking and bond-forming processes occur concurrently. Even with such a large cluster model, extensive electrostatic interactions beyond the quantum cluster and long-range solvation effects are very significant due to the large charge on the substrate and charges also on a number of protein residues. Further, a number of protein dipolar groups are aligned near the substrate reaction site to stabilize the substrate and thiolate charges. There are two transition states seen using coordinate driving by incrementally stretching the P−O bond and optimizing the remainder of the structure. These transition states occur at P−O bond lengths of 2.2 and 2.6 Å; for the latter, the calculated P−S bond length is 3.3 Å, which is a reasonable geometry for a very "loose" transition state. While geometrically sensible, the predicted transition state energy barrier is very low, about 3 kcal/mol, which is much smaller than that experimentally observed in a different PTPase (about 14 kcal/mol).[100]

Despite their extensive structural diversity, all PTPases share a common active site sequence, consisting of (H/V)CX_5R(S/T) residues, which is called the phosphate binding loop or "P-loop". This loop contains the invariant cysteine nucleophile, a serine or theonine that H-bonds to it, and an arginine nearby. In another region where there is little sequence similarity among PTPases, there is a general acid, which is always Asp, that resides in a similar position with respect to the substrate binding site in all cases.

Dillet et al.[96] have used Poisson−Boltzmann electrostatics calculations to examine the expected protonation states of the titratable residues in a variety of PTPases. They have found that the nucleophilic Cys is always in the anionic form in both the free unliganded enzyme and the Michaelis complex. The pK_a of the general acid Asp is always shifted up from its reference value in the unliganded enzyme and becomes even more basic in the Michaelis complex. (That is, the Asp tends to be protonated even at higher pH, a typical range being 5.4−9.1.) Figure 1 shows schematically the expected form of the Michaelis complex (adapted from Figure 3 of Zhang[94]) showing how the dipoles of the P-loop can stabilize the bound substrate along with the arginine cation, and showing also the positions of the conserved cysteine and the aspartate general acid. Dillet et al. found that the dipoles of the P-loop and a number (2−7) of positively charged side chains from Arg, His, and Lys make major contributions in stabilizing the Cys anion state, counteracting both the phenyl phosphate substrate dianion and the cost of burying charge within the protein which would favor the neutral Cys form. However, these charges and dipoles act fairly locally so that the Asp general acid pK_a stays high. Experimental support for these results derives from the pH dependence of the k_{cat}/K_m ratio, which indicates apparent pK_a's for the free enzymes, and from the pH dependence of k_{cat}, which indicates the apparent pK_a's of the Michaelis complex for those enzymes where the formation of the phosphoenzyme intermediate is rate limiting.[93,94,101] In these cases, the concentration of the Michaelis complex will greatly exceed that of the phosphoenzyme intermediate. Additional support for the protonation state of Asp and its role as a general acid catalyst comes from mutational studies in a low molecular weight phosphatase.

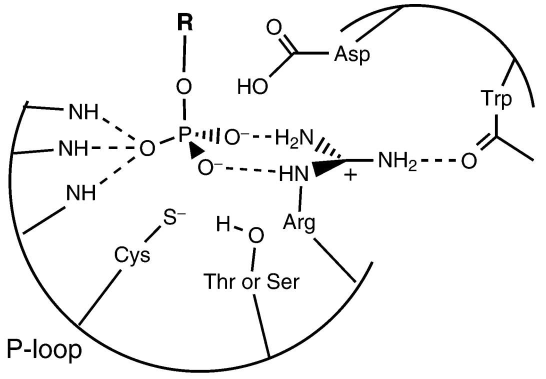

E-$ROPO_3^{2-}$

Figure 1. The active site of protein tyrosine phosphatase with bound substrate (adapted from Figure 3 of ref 94).

In recent work, our group[25] used a combination of DFT methods (Vosko−Stoll exchange-correlation potential) along with a self-consistent-reaction-field approach for the extended protein−solvent environment to evaluate the comparative reaction pathways of Mechanism A versus B for the low molecular weight (bovine) phosphatase. In this way, the effect of the charges and dielectric media outside the quantum region can be included in the description of the reaction path energetics, and the quantum cluster can polarize in response to the protein and reaction field potentials. The large extended electrostatic effects indicated by Dillet's prior electrostatics calculations can be treated along with bond-breaking and bond-making processes. The quantum cluster used is depicted in Figure 2. The P-loop dipoles reside in the electrostatic "protein" region, while the Asp129, Arg18, Cys12, Ser19 side chains, and model phenyl phosphate substrate form the quantum cluster.

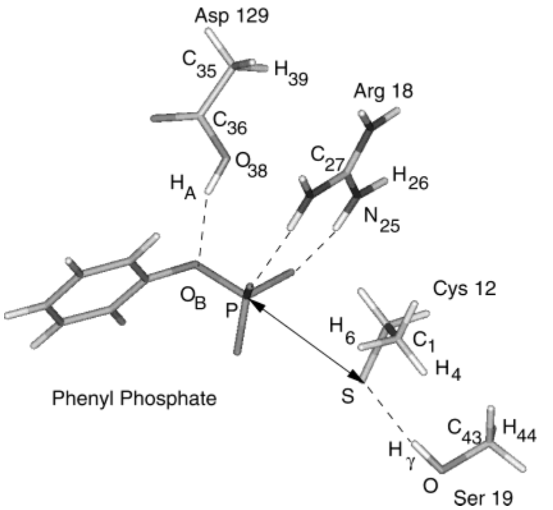

Figure 2. Schematic of the quantum cluster for the active site of bovine phosphatase. The P−S distance is the reaction coordinate.[25]

The energetic pathway for Mechanism A along the reaction coordinate, taken as the P−S distance as the intermediate is formed, is shown in Figure 3, and the Michaelis complex and the transition state structure are shown in Figure 4.

The general acid Asp129 transfers a proton to the phenoxide group early, so that this process is nearly completed in the transition state. A "loose" transition state geometry is seen with a metaphosphate ion passing between the phenol and the Cys anion. This result agrees with the analysis of observed bridging and nonbridging O kinetic isotope effects, indicating a rather "free" metaphosphate ion, but without a stable intermediate for the reaction. With Mechanism A, the catalytic pathway has not changed the basic mechanism of phosphate monoester hydrolysis, but it has made it much more efficient. (We will also

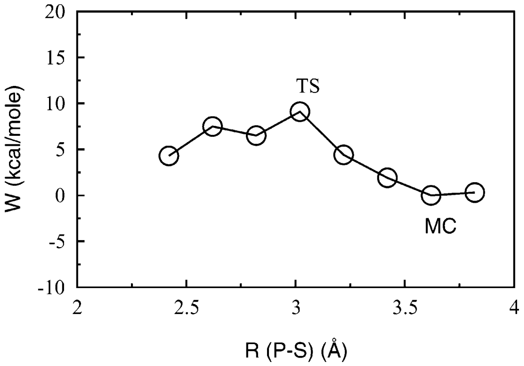

Figure 3. Mechanism A energetics along the reaction coordinate. The transition state (TS) and Michaelis complex (MC) points are appropriately labeled. The forward direction of the reaction corresponds to the right-to-left direction along the plot.[25]

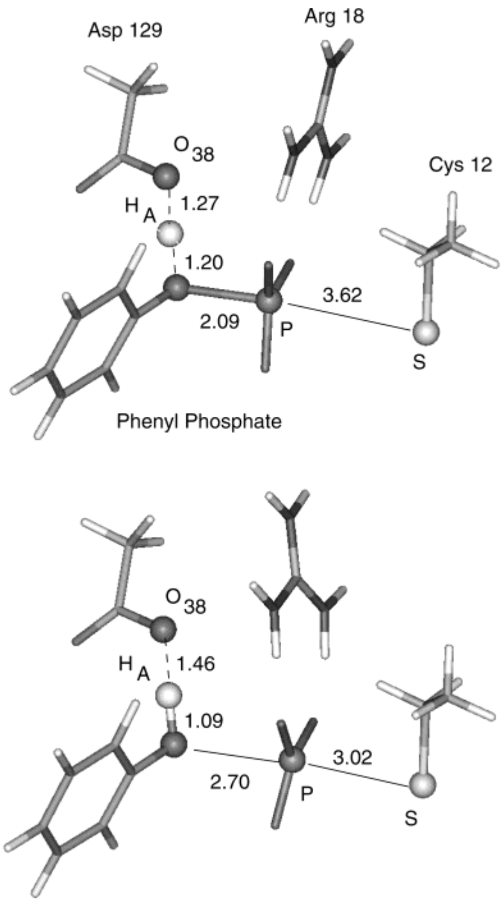

Figure 4. Michaelis complex (top figure) and transition state (bottom figure) structures for mechanism A. For clarity, the Ser 19 residue has been deleted.[25]

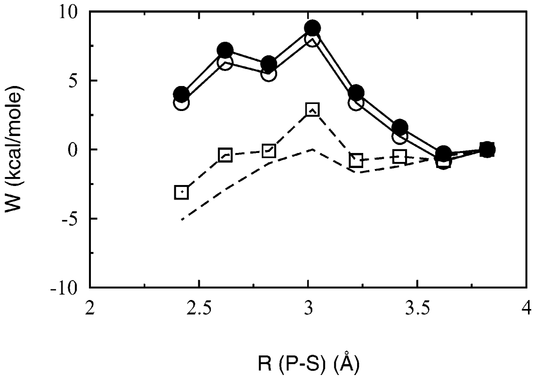

Figure 5. Comparison of different models for environment effects in mechanism A. ●, full-SCRF; ○, SCRF scheme terminated after one cycle; □, electron density as in the gas phase (initial cycle); bare dashed line, initial cycle with interaction calculated with point charges rather than quadrature over density.[25]

see below that Mechanism B is much poorer at lowering the transition state.)[92,99] The computed barrier height for Mechanism A is about 9.1 kcal/mol, which is somewhat lower than the experimental barrier of about 14 kcal/mol (see Figure 5). This agreement is reasonable given that zero-point vibrational energies and entropic terms were neglected, the size and complexity of this system, and that the experimental energy profile was obtained with *p*-nitrophenyl phosphate as a substrate, rather than phenyl phosphate. The role of the Arg cation is very interesting; it stays highly charged and shows some mobility, moving in concert with the PO_3^- group as the P−S bond is formed. One can think of the Arg cation as a "molecular guidewire", providing electrostatic guidance for the "free range of motion" of the PO_3^-. The arginine charge and mobility clearly facilitate the reaction, but charge transfer with the PO_3^- is limited. In fact, we may well have underestimated the mobility of the Arg because Arg was truncated at the $N(\epsilon)-C(\delta)$ linkage and $C(\delta)$ was replaced by a linking H. However, the resulting N−H bond was allowed to rotate about the H pivot, and the C−N−H bond angle was unconstrained. The Arg is also more highly charged (as is the PO_3^- group and the Cys thiolate) after the SCRF procedure than for the "bare cluster" (gas phase) calculation all the way along the reaction path, which is indicative of the positive potential exerted by the protein and reaction field, particularly from the P loop. (There are few charged residues near the active site in this low molecular weight phosphatase, in contrast to other PTPases where several positively charged residues act in concert with the P loop.) The gas-phase cluster calculation yields essentially no barrier at all from the Michaelis complex to the transition state. Further, if the Poisson−Boltzmann energy quadrature is calculated using the gas-phase electronic density and added to the gas-phase energy, the barrier is quite low, only 4 kcal/mol. This result is similar to the low barrier seen by Czyryca and Hengge, who had a large cluster, but no extended protein environment.[99] The structural implications and energetics of Mechanism B are shown in Figures 6and 7. An associative mechanism is clearly indicated with a very late proton transfer to the leaving phenoxide and an associative distorted trigonal bipyramidal complex in the transition state. With the late proton transfer to the phenoxide, there is no advantage to less charged starting structure. Our predicted barrier height is 22 kcal/mol for Mechanism B, which is 8 kcal/mol higher than experiment and 13 kcal/mol higher than the mechanism A results. A similar energy profile is displayed by Mechanism A if the generalized acid Asp is removed, which is likely related to the late proton transfer in Mechanism B.

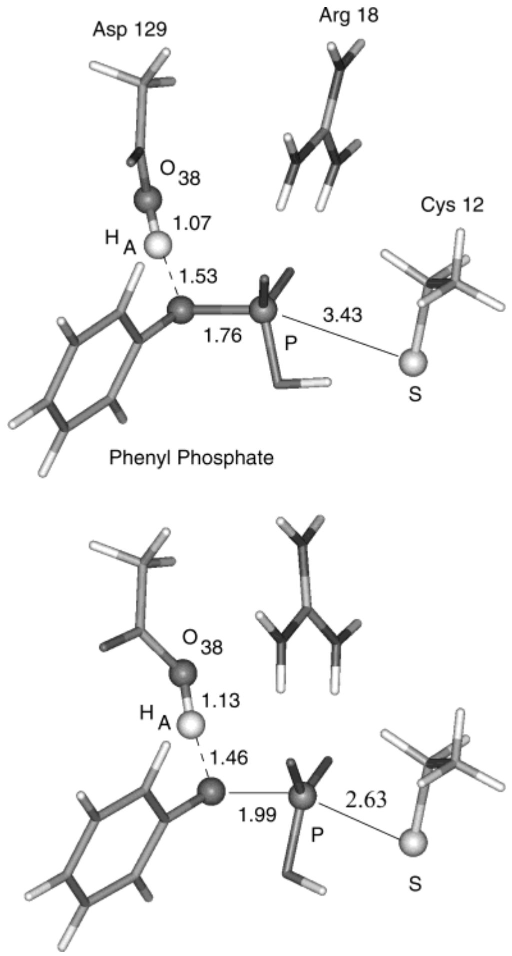

Figure 6. Michaelis complex (top figure) and transition state (bottom figure) structures for mechanism B. The rest is as in Figure 4.[25]

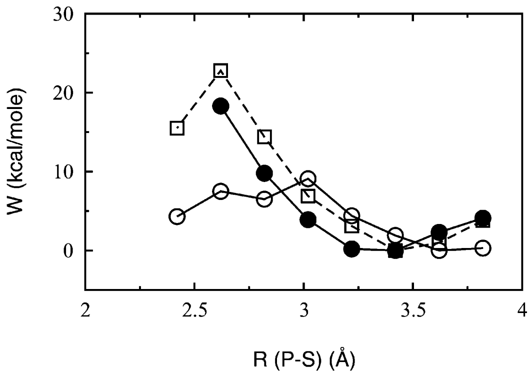

Figure 7. Energetics along the reaction coordinate for mechanism A in the absence of acid catalysis. For comparison, the profiles for mechanisms A and B are also shown. ●, mechanism A without acid catalysis; ○, mechanism A; and □, mechanism B.[25]

Mechanism A (eqs 9,10) is a more accurate representation of the reaction pathway than is Mechanism B (eqs 12,13,14). The DFT energy barrier from the SCRF calculation is much lower for the modified Mechanism A than for Mechanism B. Consistently, the experimental kinetic isotope effects (KIEs) favor Mechanism A because the KIEs clearly indicate a dissociative transition state involving a metaphosphate (PO_3^-) as does the DFT/electrostatics calculated pathway. Further, the pH profile for formation of the Michaelis complex implies that the substrate is a dianion, as in Mechanism A, and not a monoanion as in Mechanism B or B′. An essential feature of Mechanism A is that the Michaelis complex depicted in eq 9 and the transition state (Figure 4) are not associative because the aspartic acid transfers the proton early to the tyrosine (leaving group). A pentacoordinate Tyr−phosphate thiolate complex never forms.

In summary, in PTPases, we can see how a sophisticated and highly charged and polar protein structure allows the first step of a very efficient phosphate hydrolysis to occur. Our studies of the final hydrolytic step of the phosphocysteine intermediate are also nearing completion. The Arg cation acts in some ways as a metal cation, but it receives a great deal of help from the P loop, the conserved Asp and Cys, and other groups. In the following section, we will see how a simple Mg(2+) cation with its hydration shell performs in catalyzing hydrolysis of phosphodiesters.

4. Hammerhead Ribozyme

Since their discovery some 20 years ago, the study of ribozymes has become enormously active in the fields of molecular biology and biomedical science. Ribozymes are catalytic RNAs that can promote chemical reactions in the absence of proteins. These catalytic RNAs may have played a role in self-replication early in evolution. Some ribozymes are self-splicing introns. These will catalyze the cleavage and removal of the intervening sequence (the intron) from an RNA transcript, and then ligate the message from the flanking exons. This process is extremely important for the regulation and function of messenger and ribosomal RNAs in eukaryotic organisms.[102] Ribozymes can also be engineered to cleave other target RNA molecules, and, consequently, they are now widely accepted as agents capable of inhibiting gene expression. They are therefore, naturally, also associated with very promising links to candidates in gene therapy.

The hammerhead ribozyme is a small RNA molecule that makes up the genome of several plant viruses, viroids, and satellite RNAs.[103] For the cleavage of the phosphodiester backbone, a divalent metal ion is required as a cofactor to promote activity under physiological conditions.[104] The metal ion typically utilized by the organisms to activate the phosphate group of the phosphodiester linkage leading to hydrolysis is Mg^{2+}, although other metal ions have been shown to promote catalysis in vitro.[105]

The mechanism of nucleophilic displacement at the phosphorus has been proposed to be of S_N2(P) type, with an in-line geometry, where the approach of the 2′-oxygen to the phosphorus is at a 180° angle relative to the leaving 5′-oxygen,[106] leading to inversion of configuration about the phosphorus (Scheme 1).[107]

It has been shown experimentally that a metal ion ligates to the *pro*-R_P oxygen of the $-O-(PO_2^-)-O-$ group undergoing reaction, a feature crucial in the metal ion catalysis of phosphodiesters, as cancellation of the negative charge allows for nucleophilic addition to phosphorus (Scheme 2).[104,107a,b,108] Furthermore, pH titration experiments indicate that a single deprotonation event is required for cleavage.[105c,109,110]

Scheme 1

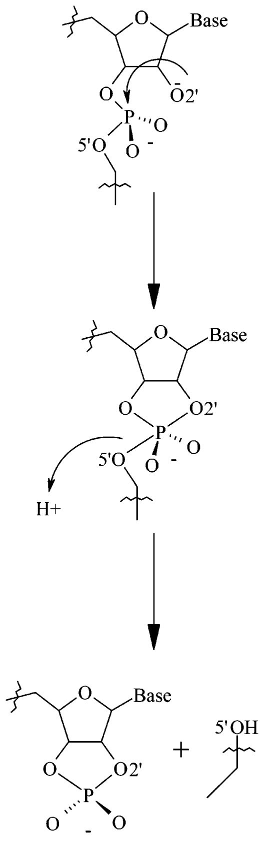

Scheme 2

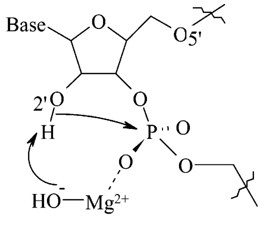

General Base

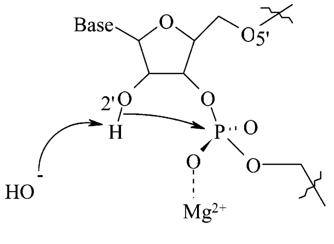

Specific Base

The metal ion can provide a ligated hydroxide to remove the proton from the 2′-hydroxide to generate the nucleophile (general base catalysis), or the nucleophile can be generated by a lyate HO$^-$ (specific base catalysis) and the metal ion has an alternate role in the reaction. Of these metal ion binding sites, at least one appears necessary to achieve proper folding and to stabilize or position other essential functional groups, while one or more additional divalent metal ions participate in the cleavage reaction.[105d] This divalent metal ion, or possibly another, can provide the necessary stabilization to the leaving group either by direct interaction with the leaving group oxygen or by orienting a water molecule such that a proton can be donated to this group. The way in which stabilization of the leaving group is achieved is a subject of debate,[111] and despite the numerous experiments performed on many different hammerhead ribozyme motifs, the precise details of the mechanism of hydrolysis and the number of metal ions essential to the cleavage reaction are not known.

There are a number of crystal structures of the hammerhead ribozyme that contain inhibitor, substrate, or modified substrate complexes,[112] and each has provided invaluable structural information and insight into the metal ion binding sites. None of these crystal structures, however, shows the 2′-hydroxyl group poised for an in-line displacement of the 5′-leaving group.

Several studies have used quantum chemical methods to investigate various aspects of the phosphodiesters hydrolysis and to model the mechanism in the hammerhead ribozyme.[113] A transition state has been located depicting the P—O bond cleavage as the rate-determining step along the reaction coordinate, but this transition state was characterized by rotations of P—O bonds, an event that is highly improbable in the hammerhead ribozyme system. Lyne and Karplus suggested that the pK_a values of ionizable groups at the active site of the ribozyme might aid in indicating possible mechanistic pathways and in inferring the nature of the chemically active species.

Incorporation of explicit water molecules has resulted in an improved representation of the computational model in theoretical investigations of acid-catalyzed phosphodiester hydrolysis.[114] Using Car—Parinello combined DFT-molecular dynamics calculations, Boero et al. examined reaction mechanisms for a model phosphodiester in a system which also contained 62 water molecules. For this ribose-phosphodiester in water, as a 1$^-$ anion, the authors found a very high reaction barrier (~57 kcal/mol) when the system was driven through the P—O2′ bond formation reaction coordinate. When Mg^{2+} was incorporated in the system as Mg^{2+}(H$_2$O)$_5$, Boero et al. find that the Mg^{2+} ion is ineffective in phosphodiester hydrolysis, although the activation energy for deprotonating the O2′ is lowered.

Very recently, DFT calculations were used to examine the effect of general base catalysis (Scheme 2) in the hammerhead ribozyme self-cleavage reaction.[115] A neutral chemical model was used, consisting of a mixed phosphodiester of methanol and 3,4-dihydroxytetrahydrofuran (charge = −1) with a [Mg^{2+}(HO$^-$)(H$_2$O)$_4$]$^{1+}$ bound to the *pro*-R_P oxygen, as shown in Scheme 3. The idea was to establish whether the presence of a single hydrated metal ion would be sufficient to enable catalysis and promote cleavage of the P—OCH$_3$ bond, the latter being commonly accepted as the rate-determining step in the reaction. This chemical model incorporates the basic features and necessary functional groups to adequately model the proposed hydrolysis reaction.[114,116]

Scheme 3

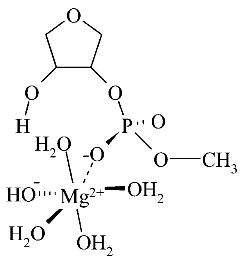

A distinct, although short-lived, trigonal bipyramidal (TBP) pentacoordinated intermediate could be identified along the reaction coordinate. The transition state leading to the intermediate (TS1) was calculated to be +18.6 kcal/mol higher in energy relative to the reacting species and corresponds to the transfer of the proton from O2′ to the Mg^{2+}-bound OH^- and simultaneous nucleophilic attack of the O2′ on the scissile phosphate. The furanose ring spans one apical and one equatorial position in accord with the proposed mechanism for hydrolysis in cyclic phosphate esters.[117] In this asymmetric transition state structure, the O2′−P attack distance is 2.06 Å and the O2′−P−OCH_3 angle for nucleophilic displacement is 157.5°. The phosphorus and equatorial oxygen atoms are nearly planar (+5.8° phosphorus deviation above plane) in contrast to that observed in the reactant (+24.0° deviation). Optimized geometries of the key structures along the reaction pathway are presented in Figure 8.

The energy of the TBP intermediate was found to be almost identical to the TS1 energy (18.6 kcal/mol above that of the reactant). It is characterized by an O2′−P distance of 1.98 Å, a P−OCH_3 distance of 1.80 Å, and an O4−P−OCH_3 angle of 157.4°. The deviation of the phosphorus from the plane defined by the equatorial oxygen atoms is +4.0°, indicating inversion of configuration about the phosphorus has not yet occurred. It is interesting here to note that a similar pentacoordinated intermediate, formed in the β-phosphoglucomutase reactions, was identified by means of X-ray crystallographic techniques by Allen and co-workers.[118]

The intermediate is very unstable. A second transition state (TS2) corresponding to a P−OCH_3 bond breaking coupled to the transfer of a proton from Mg^{2+}-bound water to the methanol leaving group is calculated to be only 2.2 kcal/mol higher than the intermediate energy (20.8 kcal/mol higher than the reactant). TS2 is an asymmetric transition state with an O2′−P distance of 1.84 Å, a P−OCH_3 bond distance of 1.96 Å, and an O2′−P−OCH_3 angle of displacement is 157.8°, slightly larger than in TS1 and the intermediate structure. The O5′−P bond breaking appears to be late, while the first proton transfer is early. The final product is calculated to be 2.3 kcal/mol lower than the starting reactant structure. The structures of the reactant, TS1, the TBP intermediate, TS2, and the final product are shown in Figure 8. Relevant distances are indicated.

The rate-determining step in the hammerhead reaction has been determined to be the departure of the 5′O^- leaving group.[105c,d,107a] This step corresponds to the highest point (TS2) on the potential energy surface in our calculations. The calculated overall energy barrier of ca. 21 kcal/mol is consistent with the reported value of the rate of reaction of approximately 1 min^{-1} (~20 kcal/mol) found in vitro for the hammerhead ribozyme.[119,120]

The potential energy surface, displayed in Figure 9, suggests further that the lifetime of the intermediate structure is very limited, amounting to a kinetically insignificant[121,122] species along the reaction pathway. From TS1 to TS2, substantial changes in geometry occur with only a small change in energy (~2 kcal/mol). It can be seen that the structure of TS1 corresponds to the transition state for endocyclic cleavage, while the structure of TS2 corresponds to that for exocyclic cleavage. Therefore, this reaction does not appear to proceed by a simple concerted mechanism.

Metal-ligated hydroxide is a requirement to create the nucleophile for initial reaction to take place, while metal-liganded water provides the critical proton to the leaving group, consistent with experimental[105a,b,107a,b,108] and molecular dynamics studies.[123,124] The energy associated with the highest lying transition state, TS2, shows that one metal ion is sufficient to catalyze the self-cleavage of the hammerhead ribozyme. The possibility of two metal ions participating in the cleavage reaction, however, cannot be eliminated.

5. Click Chemistry

5.1. Tetrazole Formation Catalysis by Bronsted Acid

Tetrazole chemistry is gaining increasing attention due to its wide-ranging applications. Tetrazoles are, for instance, used in pharmaceuticals as lipophilic spacers and carboxylic acid surrogates,[125,126] in specialty explosives,[126] photography, and information recording systems,[127] in addition to being precursors to a variety of nitrogen-containing heterocycles.[128]

The most direct method to form tetrazoles is via the formal [2+3] cycloaddition of azides and nitriles. Depending on the nature of the azide species, evidence in the literature indicates that the mechanism of the reaction is different.

With organic azides, only certain highly activated nitriles are competent dipolarophiles.[129] In these cases, the reaction is regioselective, and only the 1-alkylated product is observed.[130] It is accepted that in these cases the reaction proceeds via a traditional [2+3] mechanism (see Scheme 4).

A mechanistically more interesting case is the addition of azide salts and nitriles to give 1*H*-tetrazoles. It has long been known that simple heating of certain azide salts with a nitrile in solution (typically 100−150 °C) produces the corresponding tetrazole in high yield (see Scheme 5). This variant is much more synthetically useful, as the scope of nitriles that are competent reactants in this reaction is very broad, in contrast to the case of organic azides. In addition, a wide variety of metal−azide complexes are competent azide donors.

Mechanistically, these cases are considerably more complicated. Several possible reaction pathways can

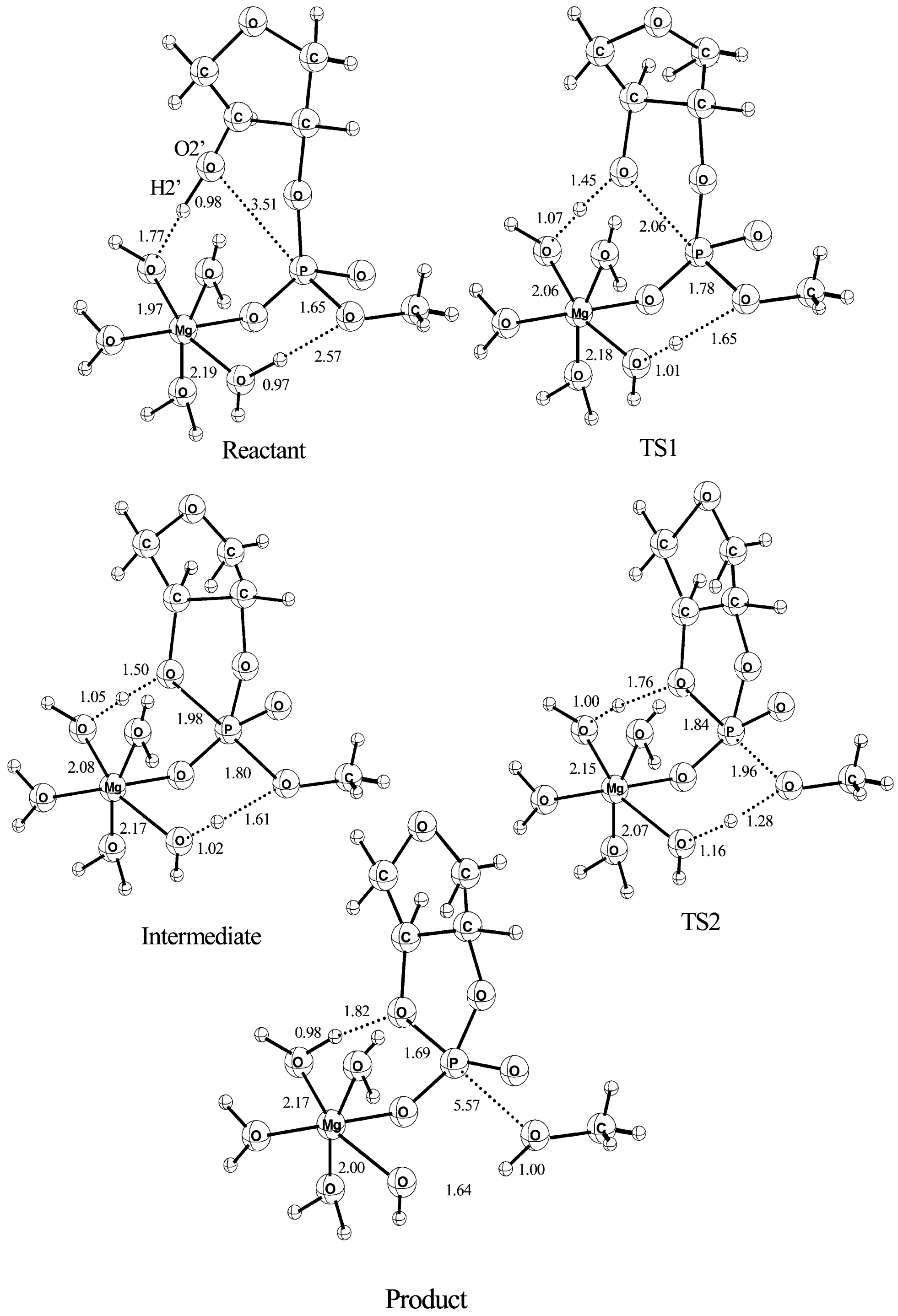

Figure 8. Geometries of key structures along the reaction pathway of the hammerhead ribozyme cleavage reaction.

be envisioned. Claims have been made for both an anionic two-step mechanism[131] and a concerted [2+3] cycloaddition,[132] but the data are not conclusive. Moreover, there is evidence against both of these mechanisms. For example, while protic ammonium salts of azide are competent azide donors, tetraalkylammonium salts were *not*, refuting the strictly anionic two-step mechanism.[132a] Also, while virtually all nitriles are engaged by ammonium azide salts at elevated temperature, organic azides only react with the most activated nitriles.[133] The fact that these azide salts and organic azides are electronically very similar, yet have significantly different reactivities, indicates that different mechanisms are likely in effect.

Density functional theory calculations using the hybrid functional B3LYP have been performed to study different mechanisms of tetrazole formation, including concerted cycloaddition and stepwise addition of neutral or anionic azide species.[134] In particular, the question of how the availability of a proton catalyzes this reaction was addressed.

It was shown that the activation barriers for the concerted cycloaddition with both the organic (neutral) and the anionic azide strongly depend on the nature of the substituent of the nitrile, that is, the

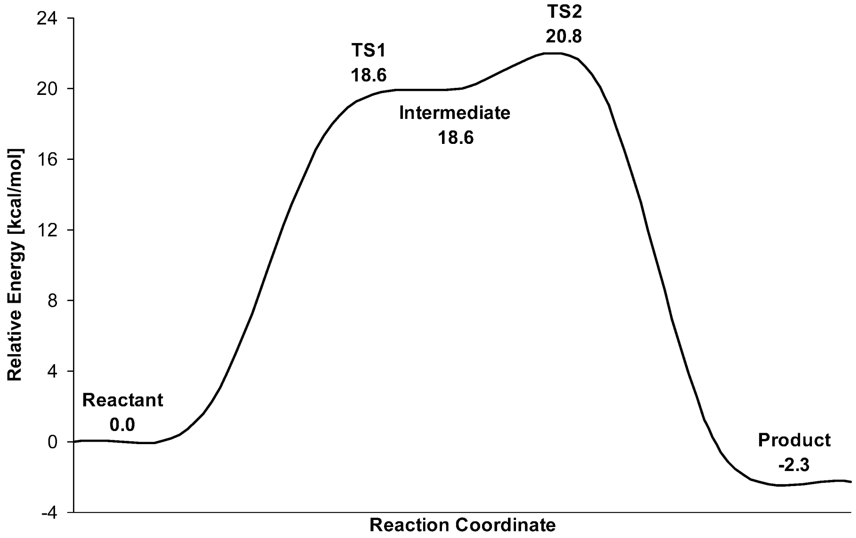

Figure 9. Potential energy curve for the hammerhead ribozyme reactions.

Scheme 4. [2+3] Cycloaddition of Nitriles and Azides

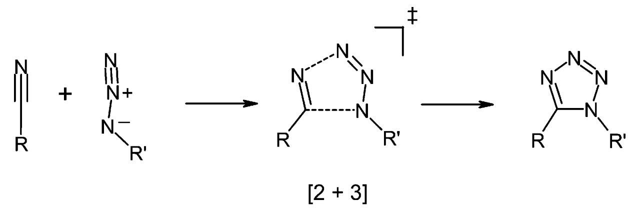

Scheme 5. Tetrazole Formation by Addition of Azide Salts to Nitriles

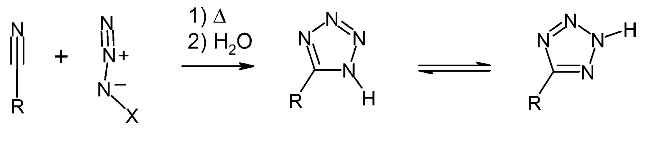

R = C, N, S
X = H, HNR_3, M

level of activation of the nitrile (see Figure 10). For example, while CH_3CN has a calculated barrier of 31.6 kcal/mol for the [2+3] cycloaddition to CH_3N_3, the more activated CH_3SO_2CN has a significantly lower barrier of 20.4 kcal/mol.

As mentioned above, only ammonium salts of azide that contain a proton are competent dipoles; tetrabutylammonium azide does not work, indicating a specific role for the proton. The calculations suggest that, when a proton is available, the reaction proceeds through a stepwise mechanism as shown in Scheme 6. In this mechanism, the azide anion and the proton source attack the nitrile simultaneously to yield a protonated intermediate (intermediate P). The activation of the nitrile by the proton facilitates the attack of the azide on the carbon of the nitrile. From intermediate P, simple 1,5 cyclization (TS2) occurs to give the 1*H*-tetrazole. In this way, the high barrier associated with the [2+3] cycloaddition is broken up into two steps, each with a smaller barrier, which is a common theme in catalytic processes.

In the calculations, the ammonium salt was modeled as a simple NH_4^+ species. The optimized structures of TS1, intermediate P, and TS2 are displayed in Figure 11. TS1 was found to be ca. 21 kcal/mol high with acetonitrile as the dipolarophile, intermediate P is ca. 3 kcal/mol higher than the reacting species, while TS2 is only ca. 15 kcal/mol higher than the intermediate. The barriers of this pathway are to be compared to the barriers of the neutral cycloaddition (31.6 kcal/mol) or the anionic cycloaddition (33.8 kcal/mol), see Figure 12.

5.2. Zinc Catalysis

It has been shown that zinc salts are excellent catalysts for the tetrazole reaction.[135] They work well even in aqueous media, allowing for an environmentally friendly large scale protocol to 1*H*-tetrazoles.[136] In these cases, simple heating (80−170 °C) of an aqueous reaction mixture of nitrile, sodium azide, and catalytic zinc salt provides the 1*H*-tetrazole in good yield following acidic work up.

DFT calculations were performed to uncover the catalytic role of the zinc ion.[137] Several possibilities were considered. First, the azide anion (N_3^-) may be bound to Zn, and the acetonitrile performs the cycloaddition without coordinating to Zn (optimized transition state structure in Figure 13A). This barrier turned out to be rather high, 35.6 kcal/mol, providing no reduction as compared to the uncatalyzed situation (31.6 kcal/mol for cycloaddition of CH_3CN and CH_3N_3 and 33.8 kcal/mol for cycloaddition of CH_3CN and N_3^-).

Second, the acetonitrile may be bound to the zinc ion, and the azide comes in from outside (transition state in Figure 13B). The calculated barrier for this reaction is 28.7 kcal/mol, representing a lower barrier as compared to the reactions without the Zn. Third, both the azide and the nitrile molecules may be bound to the zinc ion (Figure 13C). The barrier was found to be 27.3 kcal/mol, quite similar to the second case. These results suggest that the critical element of the catalysis is the activation of the nitrile by coordination to the metal ion. Hence, the Zn ion plays a role similar to that of the proton in the acid-catalyzed reaction discussed above.

To test this hypothesis and to further isolate the effect of zinc, we considered the intramolecular

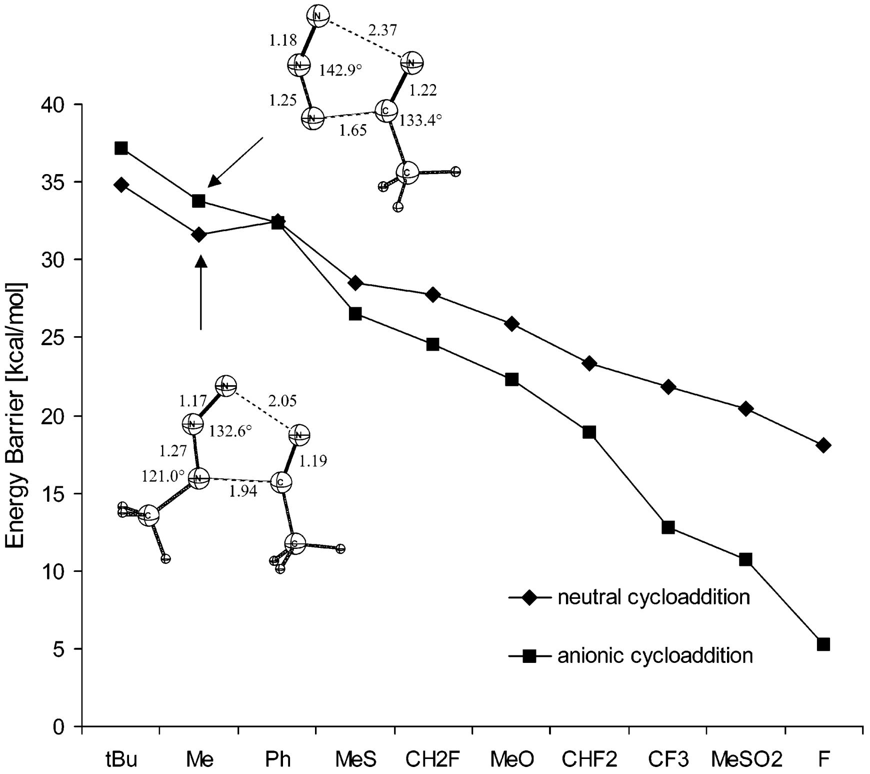

Figure 10. Calculated barriers for the [2+3] cycloaddition reaction of nitrile and azide as a function of nitrile substituent. Inserted are two typical transition state structures.

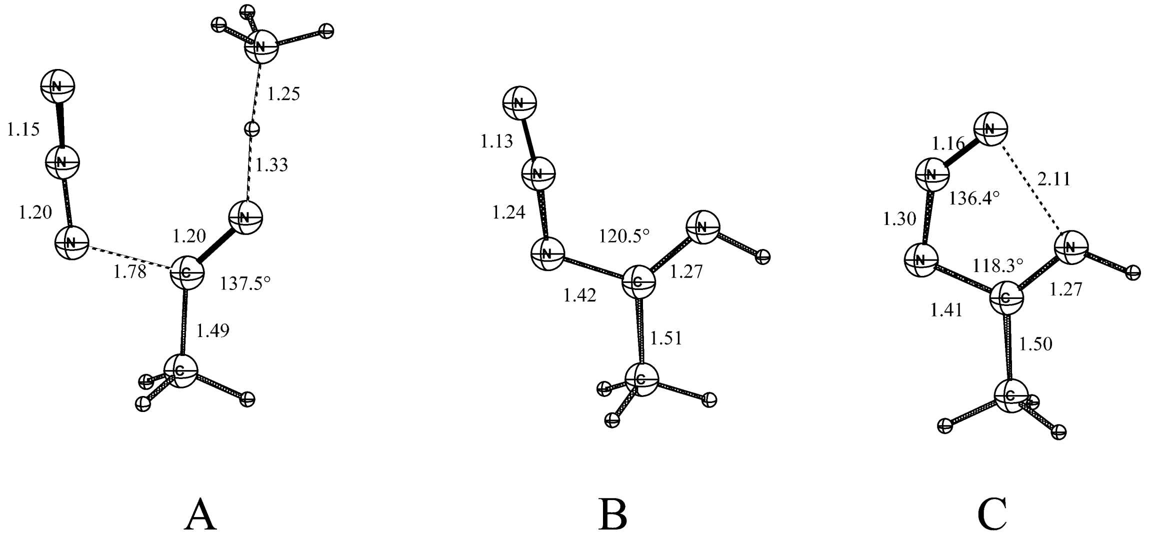

Figure 11. Optimized structures of TS1 (A), intermediate P (B), and TS2 (C) of the mechanism displayed in Scheme 6. Here, R = Me and R′ = H.

Scheme 6. Suggested Mechanism for Tetrazole Formation by Addition of Azide Salts to Nitriles, Catalyzed by the Presence of Protons

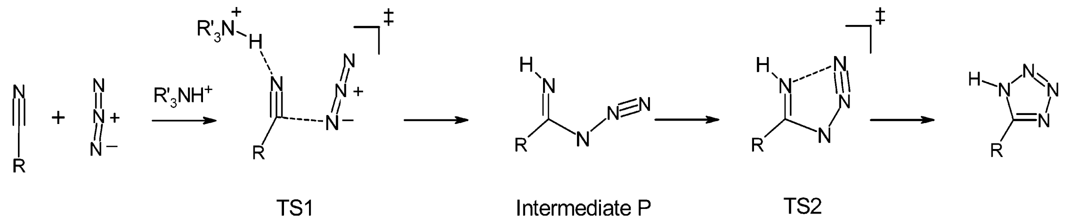

cycloaddition of the azidocyanamide shown in Scheme 7. This system was chosen to eliminate the effects of the charged inorganic azide species, as well as covalent coordination of the zinc and azide.

In the calculations, the Zn ion reduced the barrier by 5.3 kcal/mol, giving a barrier of 26.3 as compared to 31.6 kcal/mol (Table 1). From kinetic experiments, a reduction of 5.9 kcal/mol was measured, which is

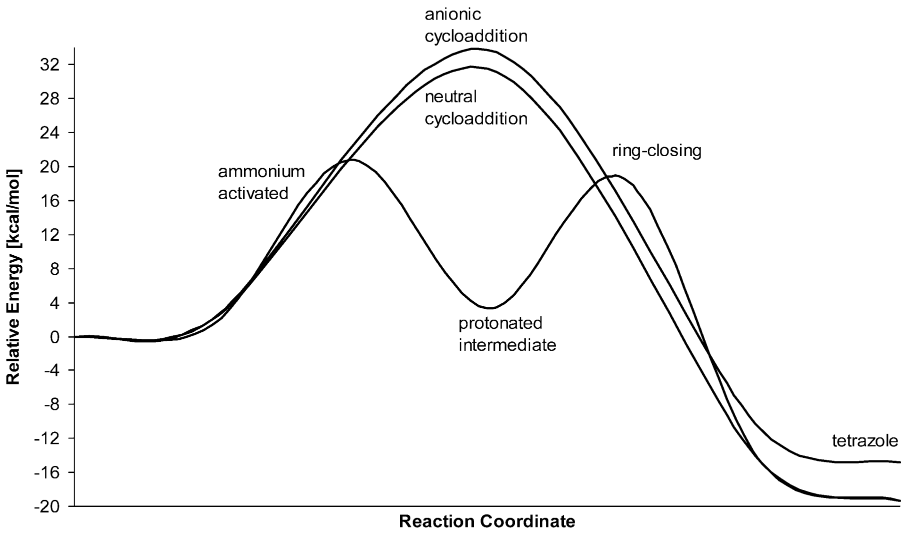

Figure 12. Comparison of the energies obtained for the various mechanisms for the formation of tetrazole from azide and acetonitrile.

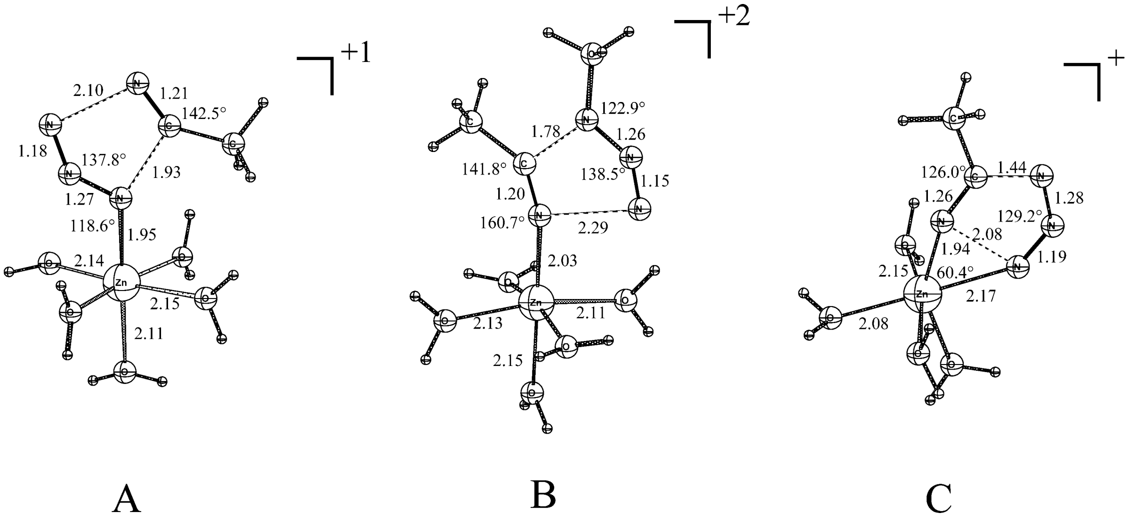

Figure 13. Optimized transition state structures for different possible scenarios of Zn-catalyzed tetrazole formation. (A) Azide coordinated to Zn, nitrile attacks from outside. (B) Nitrile coordinated to Zn, azide attacks from outside. (C) Both nitrile and azide coordinated to Zn. The calculated barriers are 35.6, 28.7, and 27.3 kcal/mol for A, B, and C, respectively.

Scheme 7. Intramolecular Tetrazole Formation Studied To Isolate the Zn Effect

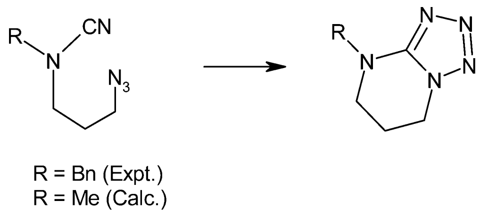

Table 1. Computational and Experimental Results of the Intramolecular [2+3] Cycloaddition of Scheme 7

additive	$\Delta H^{\ddagger}$ (kcal/mol) calculations	experiments temperature (°C)	half life (h)	$\Delta G^{\ddagger}$ (kcal/mol)
none	31.6	140	24	35.2 ± 0.2
$ZnBr_2$	26.3	75	18	29.3 ± 0.2
$AlCl_3$	19.1	23	24	25.0 ± 0.2

in excellent agreement with the theoretical value. This supports the hypothesis that the coordination of the nitrile to the Zn is the major factor responsible for catalysis.

To examine whether the Lewis acidity of the Zn is the factor responsible for the catalysis, a more potent Lewis acid was considered, $AlCl_3$. It proved to be a more powerful catalyst, with a calculated reduction of the barrier by as much as 12.5 kcal/mol (Table 1). Experimentally, this reduction was measured as 10.2 kcal/mol, again in excellent agreement with the theoretical prediction. Optimized transition state structures for the uncatalyzed, Zn-, and $AlCl_3$-catalyzed reactions are shown in Figure 14.

6. Manganese, Iron, and Copper Zinc Superoxide Dismutases

Superoxide dismutase (SOD) catalyzes the dismutation of superoxide anion radicals to hydrogen peroxide and molecular oxygen, and thus protects living cells from toxic oxygen metabolites.[138] SODs form an important part of biological defenses against toxic oxygen intermediates and radical damage. Although their biological roles are not completely understood, SODs have been shown to prevent inflammation and

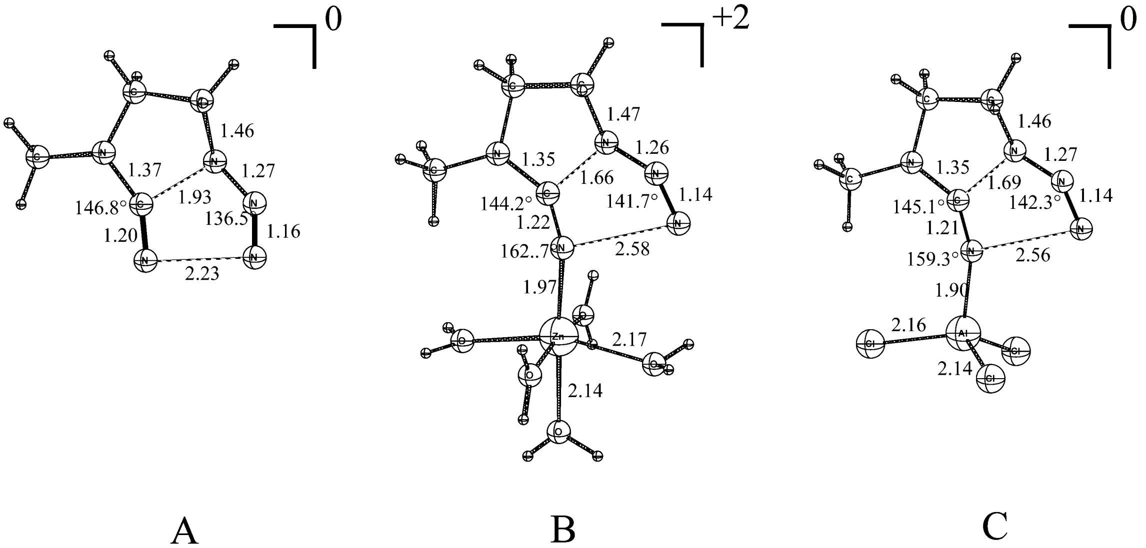

Figure 14. Optimized transition state structures for [2+3] intramolecular cycloaddition reactions. (A) uncatalyzed, (B) Zn-catalyzed, and (C) $AlCl_3$-catalyzed. Calculated barriers are 31.6, 26.4, and 19.1 kcal/mol, respectively.

oxidative damage and are involved in anticancer and antiaging mechanisms.[139] Four types of SODs are known according to the redox-active metal involved: copper−zinc-, iron-, manganese-, and nickel-containing forms.[140] Mutational defects in CuZnSODs have been associated with familial amyotropic lateral sclerosis (FALS), and defects in MnSOD have been associated with neurodegenerative diseases and cancers.[141,142] CuZnSODs are generally found in the cytosol and peroxisomes of eukaryotic cells (and also in the periplasmic space in some bacteria), FeSODs are found in prokaryotes and plants, and MnSODs are found in prokaryotes and in the mitochondria of higher organisms. Because mitochondria use over 90% of the cell's oxygen, the mitochondrial electron transport chain produces a large quantity of oxygen radicals, and MnSOD is a primary biological defense against radical damage.[139,142,143]

All of these enzymes function by dismuting the superoxide anion through the net reaction:

$$2O_2^{\bullet -} + 2H^+ \rightarrow H_2O_2 + O_2 \qquad (15)$$

We have focused on the comparative redox properties and associated catalytic cycles of Mn, Fe, and CuZn SODs. First, we used small models containing mainly the first-shell side-chain structures for MnSOD from human and bacterial *T. thermophilus* enzymes[41,144] and CuZnSOD from bovine erythrocyte.[145] Models have been enlarged to include the second-shell H-bonding partners for FeSOD from *E. coli*,[42] MnSODs from *T. thermophilus*, *E. coli*, and human mitochondria,[42] and the MnSOD mutant Q143N from human mitochondria.[42] We have established a combined density functional (DF)/electrostatics method for the coupled redox potentials (that is, a one-electron redox event coupled with a single protonation or proton transfer) of these systems. Recently, we obtained the coupled redox potentials for Mn- and FeSOD based on analysis of the measured kinetic rate constants of Mn- and FeSODs. This scheme is a valuable and practical alternative to direct electrochemical measurements of redox potentials in SODs (see ref 42 for details). We have examined some aspects of the catalytic reaction pathways for Mn, Fe, and CuZn SODs involving electron and proton transfer based on both experimental data and DFT electrostatic calculations.

6.1. MnSOD and FeSOD

MnSODs and FeSODs are normally grouped into one class because of their identical set of coordinating ligands, similarities in sequence and protein structure, particularly for the first- and second-shell residues around the active site, and similar catalytic pathways for superoxide dismutation.

Letting "M" represent Mn or Fe, a general reaction scheme outlining the catalytic dismutation of superoxide ion ($O_2^{\bullet -}$) via alternating reduction of the M^{3+} and oxidation of the M^{2+} SOD enzyme is given below:[40,42,146]

$$M^{3+} + O_2^{\bullet -} + H^+ \rightarrow M^{2+} + O_2 \qquad (16)$$

$$M^{2+} + O_2^{\bullet -} + H^+ \rightarrow M^{3+} + H_2O_2 \qquad (17)$$

The actual reaction pathway is, however, more complicated. The reactions are represented in Scheme 8 (the upper part (I) represents reaction 16, and the lower half represents reaction 17). An inactive form (X) of MnSOD has been observed to occur during the oxidative addition of $O_2^{\bullet -}$ to the Mn^{2+} center. Based on Michaelis−Menten kinetics, the inactive form only becomes relevant at high $O_2^{\bullet -}$ concentrations, and it slowly interconverts back to the active form.[147]

Scheme 8

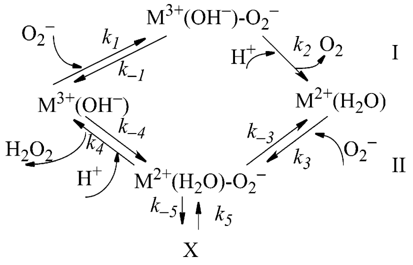

The complete Mn- and FeSOD protein is a tetramer, comprising two subunits related by a dyad axis. Each subunit consists of two chains, and each chain contains one metal active center. The resting forms of Mn- and FeSODs have active sites (see Figure 15) organized as approximate trigonal bipyramids with three histidines, one aspartate, and one hydroxyl (or water) ligand forming a five-coordinate metal site with one empty site. Our DF/electrostatics calculations show that the oxidized and reduced Mn- and FeSODs are in the [Mn^{3+}- and $Fe^{3+}(OH^-)$] and [Mn^{2+}- and $Fe^{2+}(H_2O)$] forms, respectively. In the 5−6−5 coordination reaction scheme proposed by Lah et al.[40] for FeSOD (and applied also to MnSOD), the reaction in the first and second step proceeds by addition of $O_2^{\bullet-}$ to the empty (sixth) site, with inner sphere electron transfer to or from the metal ion.

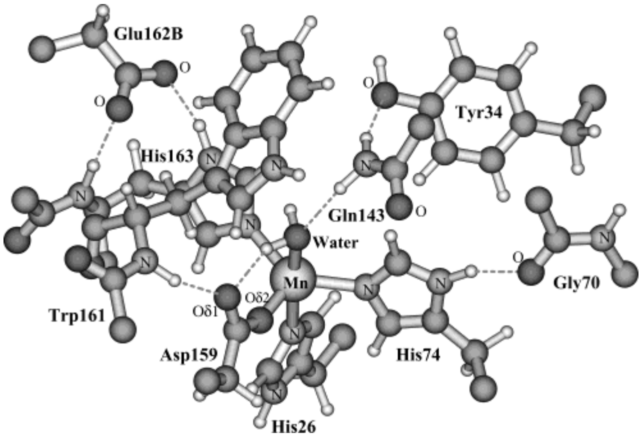

Figure 15. The active site of Mn- and FeSODs. Labels are for wild-type human MnSOD.

In the first half cycle of Scheme 8 (eq 16), a superoxide anion $O_2^{\bullet-}$ first binds at the sixth ligand site and shares an electron with the M^{3+} center of $M^{3+}(OH^-)$SOD. It then donates this electron to the metal center and leaves as an O_2 molecule. The rate constants describing the combination and the decomposition of $M^{3+}(OH^-)-O_2^{\bullet-}$ are k_1 and k_2, respectively. Bull et al.[147a] obtained (see Table 2) $k_1 = 1.5 \times 10^9$ M^{-1} s^{-1} and $k_2 = 2.5 \times 10^4$ s^{-1} for the catalysis by *T. thermophilus* MnSOD, and Hsu et al.[148] reported $k_1 = 2 \times 10^9$ M^{-1} s^{-1} and $k_2 = 8 \times 10^4$ s^{-1} for the catalysis by wild-type human MnSOD (hMnSOD). The large values of k_1 are near the diffusion-controlled limit. All kinetic studies for MnSODs show that k_2 is relatively small, with the back reaction (k_{-1}) competing with product dissociation (k_2). We propose that the superoxide anion $O_2^{\bullet-}$ cannot donate the electron to the M^{3+} center and leave as an O_2 molecule immediately upon binding, because the presence of the negatively charged $-OH^-$ ligand inhibits this electron transfer. After binding with $O_2^{\bullet-}$, the metal center becomes less positive. Consquently, the $M-OH^-$ distance becomes longer, and the net negative charge on group $-OH^-$ pulls the metal and its ligands toward the side chain of Gln (see Figure 15, Gln143 in hMnSOD). Our DFT geometry optimizations show that the average H-bonding distances (between heavy atoms) of $HO^-\cdots N$-Gln are 3.08 and 3.44 Å, respectively, in the oxidized resting form $Mn^{3+}(OH^-)$ and $Fe^{3+}(OH^-)$ SODs.[164] This H-bond is much shorter on average by 0.44 and 0.48 Å, respectively, in the $Mn^{2+}(OH^-)$ and $Fe^{2+}(OH^-)$ SODs.[42] Finally, we proposed that the reaction involves successive proton transfer along a H-bonding chain. The proton $H_{\epsilon 22}$ on the side chain of Gln (143 in hMnSOD) will transfer to the $-OH^-$ ligand, the H on the hydroxyl group of the Tyr34 side chain will go to $N_{\epsilon 2}$ of Gln143, and the O(Tyr34) site will extract a proton from its surrounding water molecules. With a water molecule now bound as the fifth ligand, the $-O_2^{\bullet-}$ group will easily transfer an electron to the metal center and leave as an O_2 molecule, giving the $M^{2+}(H_2O)$ form of MSOD depicted in the first half of Scheme 8.

Table 2. Rate Constants for Catalysis by MnSOD from *T. thermophilus*, and by the Wild-Type Mutant Y143F and Q143N MnSODs from Human Mitochondria[a]

rate constants	MnSOD *T. thermophilus*[b]	human wild type[c]	human Y34F[d]	human Q143N[e]
k_1 (M^{-1} s^{-1})	1.5×10^9	2×10^9	2×10^9	2×10^9
k_{-1} (s^{-1})	3.5×10^4	2×10^4	1×10^3	1.5×10^6
k_2 (s^{-1})	2.5×10^4	8×10^4	5×10^3	6×10^2
k_3 (M^{-1} s^{-1})	1.5×10^9	2×10^9	2×10^9	2×10^9
k_{-3} (s^{-1})	3.5×10^4	2×10^4	1×10^3	1.5×10^6
k_4 (s^{-1})	2.5×10^4	8×10^4	1×10^4	6×10^2
k_{-4} (M^{-1} s^{-1})	3.0×10^2	3×10^2	1×10^3	1×10^3

[a] See Scheme 8 for notations. [b] Taken from ref 147a, pH 9.3 at 2 °C. [c] From ref 148, pH 9.4 at 20 °C. [d] From ref 151, pH 9.6 at 20 °C. [e] From ref 152, pH 9.4 at 5 °C.

The assumption of proton transfer when $O_2^{\bullet-}$ binds to the $M^{3+}(OH^-)$ center is also consistent with spectroscopic data on the azide adducts of Mn^{3+}SOD.[149,150] The Mn^{3+}SOD−azide complex exhibits temperature-dependent absorption and circular dichroism (CD) spectra (thermochromism) changes from a lower temperature six-coordinate form to a higher temperature five-coordinate form. It was proposed that azide binding causes a proton to be transferred either to the hydroxyl group, forming a water molecule, or to be further transferred to reside on the aspartic acid.[150] The five-coordinate form may therefore result either from desolvation of the water molecule or from dissociation of the protonated carboxylate group.

In the second half of Scheme 8 (reaction 17), a superoxide anion $O_2^{\bullet-}$ first binds to the M^{2+} ion of $M^{2+}(H_2O)$SOD. The kinetic rate constant for this step is the same as k_1 ($k_3 = k_1$) (see Table 2), within the limits of the kinetic simulations. The superoxide then either leaves as $O_2^{\bullet-}$ (rate constant k_{-3}) or abstracts two protons (probably one from the ligand H_2O and one from the second-shell residue Tyr) and dissociates as a H_2O_2 (rate constant k_4). For both *T. thermophilus* and the wild-type hMnSODs, $k_4 = k_2$ from kinetics analysis, and both are relatively small. As in the first half of the cycle, the transfer of protons also controls the rate for generating the product H_2O_2.

An inactive form (X) of MnSOD has been observed in the second half of the catalytic cycle, as depicted in Scheme 8.[147] During our DFT geometry optimizations on the larger $Mn^{3+}(H_2O)$SOD active site clusters,[42] we found that one of the protons of the water ligand, which originally H-bonded to the atom $O_{\delta1}$ of the Asp ligand (see Figure 15), gradually moved closer to $O_{\delta1}$ and finally transferred to $O_{\delta1.}$ After transfer, this proton remained H-bonded to the oxygen atom of the OH^- ligand. The $Mn^{3+}-O_{\delta2}$(Asp) distance then becomes the longest of the metal–ligand distances in the optimized $Mn^{3+}(H_2O)$ cluster.[42] No such proton transfer was observed during the geometry optimizations for the $Fe^{3+}(H_2O)$SOD active site cluster.[42] We therefore propose that the inactive $Mn^{2+}-O_2^{\bullet-}$ complex is formed after such a proton transfer from the H_2O ligand to the oxygen atom of the Asp ligand. When a superoxide anion binds in the end-on form with the $Mn^{2+}(H_2O)$, the metal center will possess partial Mn^{3+} character. Further, if an electron transfers from Mn^{2+} to the $-O_2^{\bullet-}$ group to form O_2^{2-}, the metal changes to Mn^{3+}. The bound solvent then has lower energy as a hydroxyl group than as a water molecule. If one of the protons of the H_2O ligand transfers to the H-bonded oxygen of the Asp ligand (rather than to the $O_2^{\bullet-}$ group), the Asp will probably dissociate, and the O_2^{2-} group can change to the side-on form.[147a] The dead-end complex X of $Mn^{3+}-O_2^{2-}$ is thus formed. A feasible alternative mechanism is H_2O dissociation from the Mn^{2+} center.

The Trp (Trp161 in hMnSOD) indole ring which lies over the active site probably has an important, although indirect, effect on H-bonding in the active site. For both Mn- and FeSOD, the atom $O_{\delta1}$ of the Asp ligand is H-bonded with the backbone NH group of its neighboring Trp residue, as well as the water ligand. For instance, in the crystal structure of hMnSOD (PDB code: 1N0J), the distances of $O_{\delta1}$(Asp159)···O(water ligand) and $O_{\delta1}$(Asp159)···N(Trp161) are 2.901 and 3.085 Å in chain A, and 2.985 and 3.163 Å in chain B, respectively. Here, we see the importance of Trp161 in balancing the interaction between the water ligand and the Asp159 side chain. It has been found in Silverman's group that mutating the Trp161 to other residues,[147b,c] especially to Phe (W161F), will increase the product inhibition. The replacement with Phe has only a minor effect on the first half cycle (eq 16) involving reduction of the manganese. However, this mutant exhibits strong product inhibition in reaction with the reduced enzyme form.[147b] The inhibited state was very similar to that observed for the inhibited wild-type enzyme.[147b] We think one possible reason is that the H-bonding balance of Asp159 with the ligand water and residue-161 is altered in the mutants. As compared to Phe161, the Trp161 side chain will have a stronger π-cation interaction with the Mn ion and its first-shell ligands, particularly the bound H_2O. This, in turn, will shift the position of the Trp161 main-chain peptide NH. In mutants lacking a strong π-cation interaction, the strength of the interaction between the water ligand and Asp159 may increase. Therefore, once the superoxide binds with the $Mn^{2+}(H_2O)$ center, the proton transfer from the water molecule to its H-bonding partner atom $O_{\delta1}$ of Asp159 will occur more easily than the wild-type form. It was reported from the X-ray crystal structure that the H-bonds between some of the residues, including the Mn-bound water molecule, Gln143, Tyr34, a water molecule, and His30, are strengthened in W161F, and the distance between the bound water molecule and the Mn center is increased in the mutant.[147b] Cabelli et al.[147b] have proposed that the positioning of Tyr34 may be critical, because this can serve as a proton donor to the metal-bound solvent (OH^-).

To investigate the function of the residues Tyr34 and Gln143 (see Figure 15), which are in the H-bonding chain, the mutants Y34F hMnSOD (Tyr34 → Phe34)[151] and Q143N hMnSOD (Gln143 → Asn143)[152] were characterized kinetically and spectroscopically. The H-bonding chain is broken in the mutant Y34F. In the active site of Q143N hMnSOD, a new water molecule was found to fill the cavity created by the Gln143 → Asn mutation.[152] In chain A of Q143N, the side chain –OH of Tyr34 is pushed away 0.9 Å by this new water molecule and hence no longer forms a direct H-bond with the side chain of Asn143. Both Tyr34 and Asn143 are now H-bonded to the new water molecule, which also H-bonds to the original H_2O or OH^- ligand. The kinetic results suggest that the replacement of Tyr34 → Phe does not affect the diffusion-controlled steady-state constant k_{cat}/K_m, which has a value near 10^9 M^{-1} s^{-1} for both wild-type and Y34F hMnSOD.[151] However, the Tyr34 → Phe replacement does affect the rate of maximal catalysis k_{cat}, reducing by about 10-fold the steps that determine k_{cat}.[151] Comparing the kinetic rate constants in the forward direction (k_1, k_2, k_3, and k_4) for the wild-type (wt) and the mutants Y34F and Q143N hMnSODs (see Scheme 8 and Table 2), we see that $k_1(Y34F) = k_1(Q143N) = k_1(wt) = k_3(Y34F) = k_3(Q143N) = k_3(wt)$, $k_2(Y34F) < k_2(wt)$, $k_4(Y34F) < k_4(wt)$, and $k_2(Q143N) = k_4(Q143N) < k_2(wt) = k_4(wt)$. These results show that the three enzymes have the same rate for the combination of superoxide anion with the Mn^{2+} or Mn^{3+} center. The main differences of the catalysis by these enzymes are within steps 2 and 4, where the catalysis by Y34F and Q143N is much slower than that by wild-type hMnSOD, which means that the alteration of the proton-transfer pathways reduced the rates for producing the products O_2 and H_2O_2. This further supports our proposal that gated proton transfer will happen in both steps 2 and 4 and the proton transfer will occur prior to or concerted with the electron transfer from the superoxide $-O_2^{\bullet-}$ group to the M^{3+}-SOD metal center in the first half of the reaction cycle.

Edwards et al.[153] recently reported that mutation of either His30 or Tyr174B in *E. coli* MnSOD reduces the activity to 30–40% of that of the wild-type enzyme. These two residues are highly conserved and correspond to His30 and Tyr166B in hMnSOD, His32 and Tyr173B in *T. thermophilus* MnSOD, and His30 and Tyr163B in *E. coli* FeSOD. Silverman and coworkers[151,152,154,155] found that mutation of any residue in the H-bonding network of Gln143···Tyr34···H_2O···His30···Tyr166B in hMnSOD will decrease the catalytic activity. This extended H-bonding network may therefore be the complete proton-transfer pathway.

Although FeSOD and MnSOD proteins are highly homologous, they exert very different redox tuning on the active site metal ion.[156] The reduction potential, E_m, of FeSOD is higher by several hundred millivolts than that in Fe-substituted MnSOD (Fe_{sub}(Mn)SOD), and much higher than that in MnSOD.[156] Because metal ion reduction is intimately coupled to proton uptake in SOD,[42,157] the degree to which protonation of coordinated solvent is favored in each oxidation state contributes significantly to the observed E_m. Thus, stronger hydrogen bond donation to the metal-ion-bound solvent has been proposed to strongly depress the E_m value of the bound metal ion in the MnSOD protein.[156a,b,158] Very recently, Miller and co-workers examined the active site structures of FeSOD and MnSOD from *E. coli* and concluded that the E_m's can be tuned by the precise positioning of the conserved second-sphere Gln.[156c] Their DFT calculations show that, in the oxidized state, the distance between the Gln amide hydrogen and the oxygen of the Fe^{3+}-bound OH^- is decreased from 2.70 Å in FeSOD to 1.94 Å in the Fe_{sub}(Mn)SOD model, which suggests formation of a stronger hydrogen bond in Fe_{sub}(Mn)SOD. However, protonation of the solvent ligand upon Fe reduction results in considerable steric interference between the Gln and the H_2O protons in the Fe_{sub}(Mn)SOD model. This indicates that the closer active site Gln side chain in Fe_{sub}(Mn)SOD than in FeSOD destabilizes coordinated H_2O versus OH^-, thus strongly favoring the Fe^{3+} state and lowering the E_m value in Fe_{sub}(Mn)SOD.

6.2. CuZnSOD

CuZnSOD is a homodimeric protein in which the two active sites act independently.[159] Each subunit contains one Cu^{2+} and one Zn^{2+} ion in the oxidized ("resting") state. During catalysis, copper is the redox partner of the superoxide radical, whereas the oxidation state of Zn^{2+} does not change during the dismutation reaction. The interaction between the two subunits in the dimer is probably not important for the catalytic process because there is a large distance between the two remote copper sites (~34 Å).

The Cu^{2+} and Zn^{2+} in each subunit in the oxidized form of CuZnSOD are connected by a histidine imidazolate bridge (His61 in bovine erythrocyte CuZnSOD) (see Figure 16). The role of this histidine bridge and its protonation is critical for the catalytic cycle, and this will be the main focus of our analysis. The Cu^{2+} ion is coordinated by ϵ nitrogen atoms of His46, His61, and His118 and the N_δ of His44 (and more distantly by a water molecule) in a square planar geometry with tetrahedral distortion. The Zn^{2+} site has the geometry of a distorted tetrahedron created by three N_δ-coordinated histidines and an aspartate residue: His61, His69, His78, and Asp81. The bridging ligand His61 lies nearly on a straight line between Cu^{2+} and Zn^{2+}, which are separated by 6 Å.

The active site Cu^{2+} ion is at the bottom of a deep and narrow (<4 Å) channel in the protein, while the Zn^{2+} ion is completely buried. There is no evidence that the potential substrates can bind to the zinc center; rather, the Zn^{2+} ion appears to play both a structural role and a role in electronic polarization and electrostatic stabilization based on our DFT electrostatics studies.[145] While the Zn^{2+} ion is not directly involved in the catalytic process, it probably participates in the catalysis indirectly by interacting with the Cu center and the His61 bridge. The positively charged copper and zinc atoms in the active site, together with other positively charged residues, form a region of strong positive potential which attracts the superoxide to the copper. The binding of the superoxide to the Cu^{2+} center may be also assisted by a positive arginine residue (Arg141) which is located about 5 Å from the Cu^{2+} ion.[160]

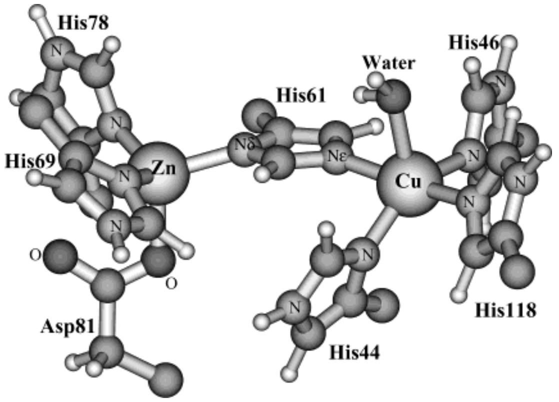

Figure 16. Representation of the active site in the oxidized CuZnSOD. Ligand numberings are from bovine erythrocyte CuZnSOD.

Mechanistic studies using pulse radiolysis established that, similar to the mechanism of Mn(Fe)SOD, the copper center is reduced and oxidized by superoxide in two steps.[161] Superoxide first reduces the Cu^{2+} ion, yielding dioxygen, and then another molecule of superoxide oxidizes the Cu^+ ion to produce hydrogen peroxide. The protons required to form the product are taken from the aqueous medium.[162] The catalytic reactions are nearly diffusion limited, occurring at a specific rate of $2 \times 10^9\ M^{-1}\ s^{-1}$ at the copper site.[162] The overall mechanism can be summarized in Scheme 9, where E symbolizes the rest of the protein.

Scheme 9

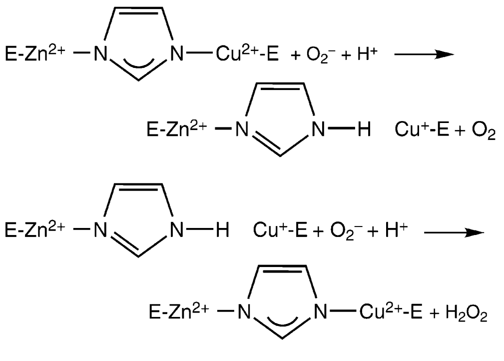

In the first step, the protonation of the imidazolate bridge upon reduction of Cu^{2+} to Cu^+ is accompanied by the dissociation of the His61−N_ϵ−Cu bond. This leads to an approximately trigonal planar Cu coordinated to three terminal histidines, with the bridging His61−N_ϵ−Cu bond being broken. In the reoxidation step, the His61 donates the proton to the substrate upon oxidation of Cu^{+} to Cu^{2+} and rebinds to Cu^{2+}.

In our DFT calculations,[145] the His61$-$N$_\epsilon$$-$Cu bond lengthens from 2.04 Å in the oxidized complex to 2.95 Å in the reduced (nonprotonated) form (see Figure 17a) and finally stretches to 3.39 Å upon protonation (see Figure 17b). At such a long distance, the His61$-$N$_\epsilon$$-$Cu bond is broken. The elongation and breaking of the His61$-$N$_\epsilon$$-$Cu bond may be partly explained by the molecular orbital analysis. Because the interaction of the oxidized CuZnSOD and superoxide is a one-electron reduction, the character of the lowest unoccupied molecular orbital (LUMO) of the oxidized CuZnSOD will represent the initial feature of this process. The major contributions to the LUMO of the oxidized structure are from d orbitals of Cu and p orbitals of N atoms bonded to the Cu ion (see Figure 4 in ref 145). Upon addition of one electron to the LUMO during the reduction, the resulting filled orbital is doubly occupied because Cu(I) retains no spin polarization, and the principal interaction becomes the antibonding interaction among the Cu d_{z^2}, $d_{(x^2-y^2)}$, and His61$-$N$_\epsilon$ p_z orbitals. This leads to the longer His61$-$N$_\epsilon$$-$Cu bond. During the elongation, the His61 ring tilts away from the copper ion and, simultaneously, the position of the Cu ion shifts relative to His61. This results in an increase in the Cu$-$His61 distance from 2.04 Å in the oxidized form to 2.95 Å in the reduced nonprotonated (Figure 17a) form and to 3.39 Å in the reduced protonated (Figure 17b) form, respectively. During the optimization of the reduced nonprotonated form, we have found a second, higher-energy local minimum which corresponds to a geometry with a His61$-$N$_\epsilon$$-$Cu bond distance of 2.64 Å. All other bond lengths and angles are similar to those in the fully optimized reduced nonprotonated form. This complex in the gas phase is 2.2 kcal/mol higher in energy than the reduced nonprotonated geometry with a His61 N$-$Cu bond length of 2.95 Å. This suggests that the potential energy surface associated with the process of the His61 N$-$Cu bond elongation upon reduction is fairly flat. The calculated energy minimum geometry for the reduced form is a structure with the His61$-$N$_\epsilon$$-$Cu bond broken. This predicted geometry is consistent with most of the X-ray experiments.[163]

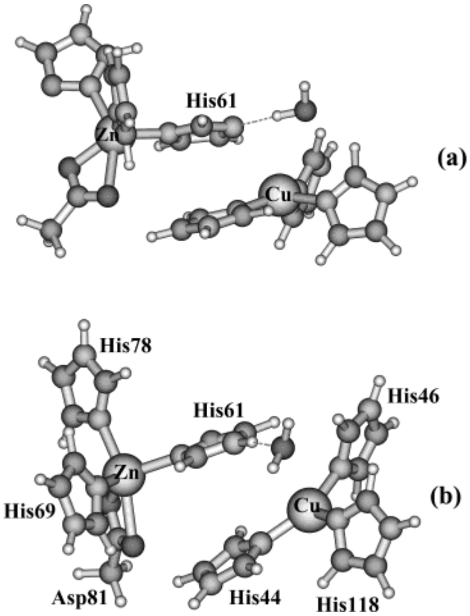

Figure 17. Optimized geometry of the reduced active site in CuZnSOD, (a) with nonprotonated His61; (b) with protonated His61.[145]

There are no significant changes in the Zn site geometry during the reduction and protonation. However, Zn ion in combination with its first- and second-shell ligands does modulate the pK_a of the histidine which switches from bridging to nonbridging (and back) during the catalytic cycle. Specifically, to study the influence of the histidine bridge and the Zn ion on the acidity of the His61 N$_\epsilon$$-$H proton, we calculated the pK_a of the Zn$-$His61 fragment, that is, the fragment which includes bridging His61, Zn^{2+}, Asp81, His69, and His78. The pK_a for the His61 H$_\epsilon$ proton of this fragment in a continuum dielectric (aqueous solution only) is 11.5, which is moderately less acidic than the full CuZnSOD complex (pK_a = 9.43 in pure solvent). This suggests that the zinc site in the CuZnSOD is responsible for most of the basicity of the CuZnSOD. The presence of the positively charged Cu^{+} ion in the full reduced CuZnSOD complex makes the His61 N$_\epsilon$$-$H proton more acidic, which increases its availability for the reaction. The effect of the Zn^{2+} and its associated terminal ligands (Asp81, His69, His78) on His61 is the result of bonding and electronic polarization. The relevant total charge of [Zn(II)AspHis$_2$] is +1, which is the same as the N$_\delta$ proton it replaces, and the calculated pK_a of bridging His61 at N$_\epsilon$ (11.5) can therefore be compared to that for methyl-imidazolium → methyl-imidazole + H^{+} (6.6 from experiment[164] and 7.5 calculated[62]). Further, the more extensive protein/solvent models yield more basic pK_a values than a simple active site model with continuum water alone. The protein residue making the largest contribution to this upward pK_a shift was found to be Asp122, which bridges His44 and His69, which are in turn coordinated to the metals. The pK_a shift due to Asp122 (a second-shell ligand to both Cu and Zn) was calculated giving $\Delta pK_a = 4.6$ units based on the protein field electrostatic energy term.

Toward the end of the catalytic cycle, when the second superoxide is bound to Cu^{+}, the electron transfer to give Cu^{2+} and peroxide strongly drives deprotonation of the linking His61 and re-formation of its bond to Cu^{2+} as expected from fundamental chemistry[12] and as supported by the DFT/PB calculations.[145]

This picture of the energetic role of the Zn^{2+} and its ligands is consistent with pulse radiolysis experiments on the pH dependence of Cu^{2+} reduction and Cu^{+} reoxidation during catalytic turnover of $O_2^{\bullet-}$.[165] The pH profile of intact CuZnSOD shows nearly pH-independent behavior of both catalytic, k_{cat}, and spectroscopic properties from pH 5 to 9.5. By contrast, removal of the Zn^{2+} ion shows pH dependence of catalytic Cu^{2+} reduction above pH = 8, and more extensive pH dependence (from pH = 6$-$10) for Cu^{+} reoxidation and peroxide product release.

The measured pK_a (assigned to bridging His) in reduced CuZnSOD is about 10.7, close to the range of the most complete DFT/PB models 10.6 to 12.5.[145,165] It might be possible for the catalytic cycle to work without protonating the bridging His (for example, by using nearby waters directly as a proton source), but this would cost at least 5 kcal/mol for the initial Cu(II) → Cu(I) reduction and would raise proton-transfer barriers throughout the catalytic cycle as well. This partly rationalizes the experimental observation that the reduced CuZn yeast enzyme X-ray structure clearly shows a broken Cu(I)−His bond, while in the reduced bovine structure, this bridging Cu(I)−His bond appears intact. There is probably also redox heterogeneity in the bovine structure based on the Cu−His bridge distance.

Some general comparisons can be drawn between the catalytic cycles of CuZnSOD versus MnSOD and FeSOD. In CuZnSOD, the breaking of the Cu(I)−bridging His61 bond (and the closely related His protonation) is controlled by changes in ligation and geometry, aided also by the Zn^{2+} and its ligands. The His61 is well positioned to protonate the peroxide and re-form the Cu−His61 bond. In MnSOD, the protonation of $(OH)^-$ on reduction of Mn(III) is also energetically favorable, but partial or complete dissociation of Asp or H_2O may then occur, leaving the Mn active site open enough to allow side-on peroxide binding. Internal proton transfer from that water or Asp to bound end-on or side-on peroxide is more circuitous in MnSOD and FeSOD than in CuZnSOD.

7. Nitrogenase

Iron−sulfur proteins play a major role in biological electron transfer and have been a critical part of all living organisms for the last two or three billion years.[13,166] Following the recognition of these proteins some 40 years ago, their physical properties have now been studied using a wide variety of spectroscopic and theoretical techniques,[167] and the biological importance of iron−sulfur (Fe−S) clusters is well-documented. Aside from their role as electron-transfer agents,[168] Fe−S clusters function as integral components of complex multielectron oxidoreductase enzymes,[169] where substrate binding and catalytic transformations are accompanied by the multiple transfer of electrons, as in the sulfite[170] and nitrite[171] reductases and several hydrogenases.[172] Fe−S clusters also play a critical functional role in the redox-active metalloenzyme, nitrogenase.

The biological conversion of dinitrogen (N_2) into ammonia (NH_3) by nitrogenase constitutes a key component of the nitrogen cycle,[173,174] in which nitrogen availability to support life on earth is maintained. Within the cycle, prokaryotic microorganisms reduce dinitrogen first to ammonia under mild physiological conditions, which subsequently is used for constructing the essential amino acid building blocks for the synthesis of proteins and nucleic acids. Nitrogen fixation is frequently the limiting factor in plant growth, and, consequently, industrial processes have been developed[175] to fix dinitrogen chemically.

Nitrogenases are known with either purely Fe or with VFe-containing proteins,[176] but the most commonly studied is a molybdenum−iron-based system, whose biochemistry has been extensively reviewed.[177] Molybdenum−iron nitrogenase consists of two separate proteins: the Fe protein and the MoFe protein, named according to their metal composition.[178] The Fe protein contains a single 4Fe4S cluster, similar to that observed for other iron−sulfur proteins. The MoFe protein contains two unique types of polynuclear metal−sulfur clusters, the P-cluster and the FeMo cofactor (alternatively M center or FeMoco) shown in Figure 18, the former containing eight iron atoms and the latter comprising one molybdenum and seven iron sites.

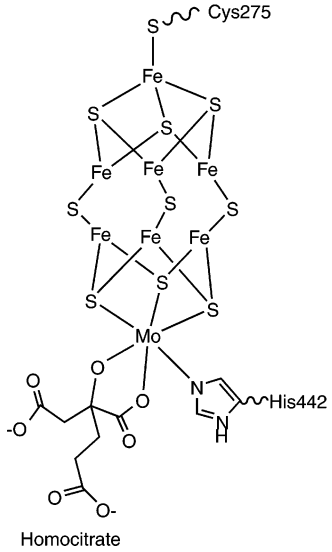

Figure 18. The original FeMoco active site of nitrogenase.

The docking of the MgATP-bound form of the Fe protein to the MoFe protein initiates enzyme turnover, during which the role of the Fe protein is to transfer electrons via the P-cluster to the active FeMo cofactor, which is the proposed site of binding and reduction of dinitrogen. The overall chemical reaction stoichiometry (assuming the reactant-to-product ratio of N_2:H_2 is 1:1) is

$$N_2 + 8H^+ + 8e^- + 16MgATP \rightarrow 2NH_3 + H_2 + 16MgADP + 16P_i \quad (18)$$

and for efficient turnover this process requires the hydrolysis of *at least* two units of MgATP for each electron that is transferred. Another determinant of product distribution is the electron flux through the MoFe protein: high flux favors reduction of N_2; at very low flux, dihydrogen (H_2) is the only product even in the presence of N_2.

The activity of nitrogenase is often described in terms of the catalytic cycle proposed by Lowe and Thorneley, in which *Klebsiella pneumoniae* nitrogenase has been analyzed in terms of a kinetic scheme describing the different protonation and oxidation states of the MoFe protein[179] (Figure 19).

In brief, successive one-electron reductions of the resting FeMoco (denoted E_0) give $1e^-$, $2e^-$, and $3e^-$ reduced states labeled as E_1, E_2, and E_3, etc., while coupled proton transfers, one for each electron transferred to the cluster, give states E_1H_1, E_2H_2, and

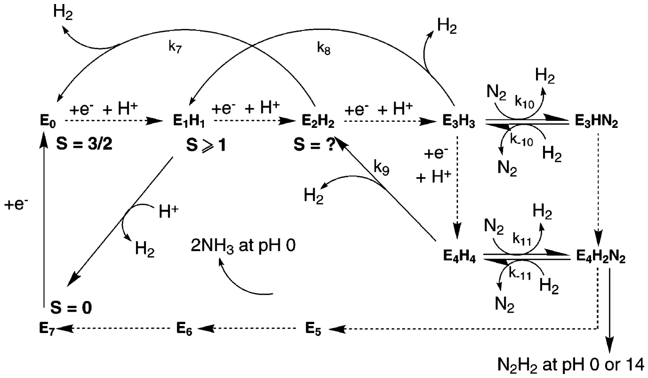

Figure 19. Modified Lowe–Thorneley scheme for dinitrogen binding and reduction.

E_3H_3, etc. Beyond state E_3H_3, an extensive accumulation of kinetic data supports N_2 entering the cycle and binding as part of the process by which N_2 and H_2 exchange. The eventual cleavage of the dinitrogen triple bond and dissociation of two molecules of NH_3 results after step $E_4H_2N_2$, and the cycle proceeds via another intermediate state, E_7, back to the resting state. State E_7 is presumed to be one electron more oxidized than the resting E_0 state and is probably similar to a diamagnetic state (named M^{OX}) characterized by spectroscopy.[180,181]

A key advance to understanding nitrogenase function in terms of the proposed kinetic scheme has been provided by the crystal structures of both the Fe protein and the MoFe protein. The first crystal structures of the MoFe protein were obtained on enzyme isolated from several independent bacteria, such as *Azotobacter vinelandii* (*Av*),[182] *Clostridium pasteurianium* (*Cp*), and *Klebsiella pneumoniae* (*Kp*). EPR studies on the *Av* crystals give rise to the spectroscopically assigned native dithionite-reduced (P^N, M^N) and oxidized (P^{OX}, M^{OX}) states. Electrochemical and spectroscopic studies[183] further reveal that each M^{OX} cluster is one-electron oxidized as compared to M^N; each P^{OX} cluster is two electrons oxidized with respect to P^N.

The original structure of the M-center, the proposed active site of nitrogenase, featured two distorted metal cubane fragments linked by three μ-2 sulfide bridges. One cubane has four iron centers (4Fe3S), and the other comprises three iron sites and one molybdenum (Mo3Fe3S), with each cuboidal component attached to the protein via only one ligand. Cys275•Sγ coordinates to the corner Fe site of the 4Fe3S cubane to complete its tetrahedral environment, while His442•Nδ provides the covalent link to the Mo site, whose octahedral coordination sphere is completed by carboxylate and hydroxyl oxygens of an organic homocitrate ligand. Contrary to initial expectations, the availability of the FeMoco structure has yielded only limited insight into cofactor function and underlying electronic structure. A complete understanding has been hindered by the limited availability of definitive experimental data, which thus far have derived from a variety of biochemical experiments, genetics techniques, kinetics measurements, and spectroscopic (EPR, Mössbauer, ENDOR, and EXAFS) studies.

Isolation of the MoFe protein in the presence of excess dithionite reveals an M-center in the resting oxidation state (M^N corresponding to E_0 of the catalytic cycle) that yields a prominent $S = {}^3/_2$ EPR signal at $g = 4.32$, 3.68, and 2.01.[184] An analysis of the oxidation states of the individual Fe sites has, however, been prevented by the difficulties associated with interpretation of the hyperfine parameters from the ENDOR[185] and Mössbauer data. Combined ^{57}Fe Q-band ENDOR and EPR data suggest metal valence assignments of $1Mo^{4+}$, $6Fe^{2+}$, and $1Fe^{3+}$ (alternatively $1Mo^{4+}$, $5Fe^{2+}$, and $2Fe^{2.5+}$). These valence assignments have recently come under scrutiny following a revision of the original Mössbauer data analysis,[186] and $1Mo^{4+}$, $4Fe^{2+}$, and $3Fe^{3+}$ have been proposed on the basis of a comparison of average isomer shift data for FeMoco with that for an Fe^{2+} model complex with trigonal sulfur coordination.[187]

Even less is known about FeMoco during enzyme turnover. States that lie either one-electron reduced or one-electron oxidized along the catalytic pathway from E_0 have been isolated and characterized. The $S = {}^3/_2$ resting state may be reduced to an EPR-silent ($S \geq 1$, most likely $S = 2$) state (M^R), which is only observed when the reduced Fe protein and MgATP are present, that is, under physiological turnover conditions. For the M^N to M^R conversion, the average isomer shift (δ_{av}) remains relatively unaffected at $\Delta\delta_{av} = 0.02$ mm s^{-1}, indicating that reduction produces only minor changes in the electron density at the Fe sites. In the absence of the reduced Fe protein and MgATP, reduction of M^N to M^R has not yet been accomplished, but an alternate one-electron reduced state (M^I) having an integer electronic spin ($S \geq 1$, most likely $S = 1$) has been identified from radiolytic reduction of freeze-quenched M^N. In contrast to the M^N-to-M^R conversion, δ_{av} for M^N to M^I changes by 0.05 mm s^{-1}, suggesting that X-ray reduction occurs in the Fe portion of the cluster. The M^N state can also be observed with the addition of redox-active dyes with midpoint potentials ranging from 0 to −100 mV, yielding a state in which the $S = {}^3/_2$ EPR signal disappears (M^{OX}). This one-electron oxidation is fully reversible, and Mössbauer and MCD have established that M^{OX} has a diamagnetic ground state, δ_{av} of which changes by −0.06 mm s^{-1} relative to M^N. The inference from the changing average isomer shift values and total spin is that the spin-coupling pattern present in M^N no longer persists on one-electron oxidation.

A recent high-resolution X-ray crystallographic analysis of the nitrogenase MoFe protein has recently revealed a previously unrecognized ligand coordinated to six iron atoms in the center of the catalytically essential FeMo-cofactor (FeMoco).[188] The new central atom completes an approximate tetrahedral coordination for each of the six iron atoms of the prismane, instead of the quite unusual trigonal coordination originally proposed on the basis of earlier, lower resolution structures.[182] The crystallographic refinement at 1.16 Å is consistent with this newly detected atomic component being a light element, most plausibly nitrogen,[189] but unambiguous identification of the atom type based on its electron density alone has proven to be difficult, even at such a high level of resolution.

Carbon, nitrogen, oxygen, and sulfur have been postulated as chemically plausible candidates for the central atom, shown in Figure 20, and each has been tested against the available diffraction data. Of these four elements, sulfur was deemed the least likely because its electron density is too high as compared to experiment. Also, the observed distances to the surrounding iron atoms were too short. Carbon, nitrogen, or oxygen could not be differentiated between, nor could they be ruled out from the X-ray analysis. On the basis of the resolution-dependent electron-density profile and the fact that nitrogenase interacts with dinitrogen to generate ammonia, this central ligand was tentatively assigned as N.

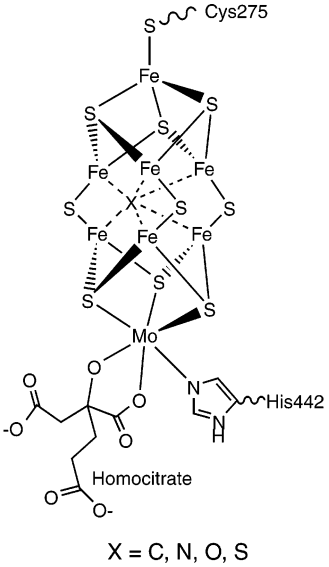

Figure 20. The FeMoco of nitrogenase with an unknown ligand (X) sitting in the center.

Prior to knowledge of the central atom, a number of workers using various theoretical approaches have examined the ultimate question for nitrogenase: where does nitrogen bind, and how is the dinitrogen triple bond reduced and cleaved? Plass[190] was among the first to apply extended Hückel molecular orbital (EHMO) calculations to the FeMoco to compare and evaluate the potential consequences of heteroatom substitution in the cofactor, by way of the differences and similarities in the MO analysis. Deng and Hoffmann[191] utilized the EHMO approach to calculate a cluster model $[HFe_4S_3(\mu\text{-}S)_3Fe_3S_3MoH_3]^-$ and concluded that metal−metal bonding in the cluster is important. They also considered nine possible N_2 binding modes. Stavrev and Zerner[192] employed the semiempirical ZINDO approach to study the whole FeMo cofactor, including side-chain ligands to Mo and four coordination to Fe, but the calculations were done by the restricted open-shell Hartree−Fock (ROHF) approximation and a configuration-averaged method. They also explored various positions for nitrogen binding and found that N_2 preferentially coordinates inside the FeMo cofactor. Reduced forms of the FeMo cofactor were also examined with the contraction of the cluster and the change in Mo site upon reduction rationalized by bond index analysis. The first density functional calculations on a large FeMo cofactor were done by Dance,[193] using a spin-restricted approach. N_2 was postulated to bind one of the Fe_4 quadrilateral faces of MoFe. Siegbahn et al.[194] published spin unrestricted hybrid density functional calculations on the mechanism of ammonia formation using a model cluster that was a more easily intelligible, using an approximate subunit of the full FeMo cofactor. Using an Fe(II)Fe(II) model as a starting point to study the N_2 binding and activation, the results were compared in a few cases with a larger Fe_8S_9 model, for which no side ligands were included. However, only ferromagnetic coupling of the spins on the Fe sites was considered. Barriere et al.[195] have investigated the possibility of activating molecular nitrogen at the molybdenum site using an EHMO description of structural and functional models of the enzyme. They also examined the possibility that the homocitrate acts as a leaving group at molybdenum, concluding that the fragmentation proposal is unlikely due to an unfavorable energy. Recently, Rod et al.[196] have studied the reactivity of FeMoco by using a plane wave basis set with a spin polarized exchange correlation functional. This study was based on a structure consisting of periodically repeating units, each with stoichiometric formula $MoFe_6S_9$. It was shown that N_2 can bind on top of FeMoco on one of the Fe sites and that a mechanism where adsorbed N_2 is hydrogenated stepwise to form two ammonia molecules is possible at low temperature, providing that the chemical potential of the reacting H-atom is higher than that of H_2. The FeMoco calculations were also compared to corresponding calculations for a Ru(0001) surface and calculations for the Haber−Bosch mechanism on Ru(0001) to illustrate why two different mechanisms are in use, and that widely different reaction conditions are required for the enzyme and the metal surface. This study was later expanded. The size of the FeMo cofactor employed has been extended to include a more correct description of the spin properties of the FeMo cofactor to rationalize a number of other experimentally observed features of the FeMoco function, including H-bonding and H_2 formation, CO adsorption, hydrogenation of adsorbed N_2, and proton transfer to adsorbed N_2 and CO. Of late, Morokuma et al.[197] have utilized hybrid (B3LYP) DF methods and examined various dinitrogen binding modes to Mo using an abbreviated model of the homocitrate end of the FeMo cofactor. In their approximate model, no Fe sites were included, and the principal conclusion was that His442 cannot be protonated at $N\epsilon$. Durrant[198] has used DFT to relate the intrinsic dinitrogen binding affinities of the Fe and Mo sites of the FeMoco to those of known N_2 complexes. The results indicate that binding to FeMoco is reversible and Mo is the preferred site. In later work, possible routes for the transfer of protons from the surface of the MoFe protein to the cofactor have been suggested, and the implications are discussed in terms of the Lowe−Thorneley scheme. By studying smaller subsections of the FeMoco using DFT-based methods for a number of models and describing the protein by molecular mechanics, the latest DFT calculations by Durrant indicate that the homocitrate ligand of the cofactor can become monodentate on reduction, allowing nitrogen to bind at Mo; Fe then plays a crucial role in stabilizing the initial reduced nitrogen species and facilitating cleavage of the N−N bond. This work was followed by reactions with diazene and isodiazene with H_2, and the results have been used to extend the model for N_2 reduction to describe the formation of HD from D_2. This latter mechanism involves a combination of two well-established chemical reactions, competitive protonation of metal N_2 species followed by scrambling of D_2 at a metal hydride.

Notwithstanding the missing central atom, the reported calculations provided considerable information but also shared one or more of a number of shortcomings, neglecting several potentially vital aspects of the electronic structure. These include the use of structural models that were greatly oversimplified, model FeMo cofactors with d electron counts that were inconsistent with the available experimental data, the use of ferromagnetic rather than antiferromagnetic coupling of electron spins, and with the exception of the recent work by Durrant, a neglect of the protein/solvent environment; the latter contributes a number of essential features to the enzymatic function. Thus, the combined effects due to the charged amino acid side chains within the second ligand shell on the active site are not considered, as well as the potentially crucial role they play in hydrogen bonding, coupled electron/proton transfer, and stabilization of small molecule binding to the FeMo cofactor.

For the resting state of the enzyme, we have also employed density functional calculations as a means of understanding several properties of the FeMoco,[63,199] including the spin-coupling mode within the seven iron sites, a detailed oxidation state description for the iron sites for the most stable spin-coupling mode for the resting cofactor, as well as a comparison of measured and calculated redox data in the protein environment for experimentally characterized states of the FeMoco.

The revelation that an atom sits in the center of the FeMoco now introduces a major new factor as compared to all of the previous theoretical assessments. Originally, we assigned the most likely oxidation states of the molybdenum and iron sites to be $Mo^{4+}6Fe^{2+}1Fe^{3+}$, consistent with ENDOR data, but this assignment needs to be reexamined, especially in light of the alternative $Mo^{4+}4Fe^{2+}3Fe^{3+}$ oxidation states also proposed on the basis of Mössbauer measurements. The presence of the newly detected central atom may also help to explain why our original redox potential calculations for the FeMoco with no central atom deviated from experiment by +0.82 V, even though for a number of iron−sulfur clusters in proteins, our calculated redox potentials are generally 0.2−0.3 eV lower than experiment.[57,200]

We have recently examined how the presence of a centrally located atom affects the cofactor geometry, the electron density at the iron sites and, hence, the average Mössbauer isomer shift value, and the redox potential between the resting cofactor and its one-electron oxidized counterpart in the protein environment. On the basis of the resolution-dependent electron-density profiles, the central atom of FeMoco has been proposed to be either C, N, or O. Calculated core structures for C^{4-}, N^{3-}, and O^{2-} anions in the center of the FeMoco are given in Table 3, along with the structural data at a resolution of 1.16 Å. A comparison of the structural data with the calculated parameters indicates that oxygen is improbable as Fe−O bond distances are calculated to be much longer than those in the X-ray structural data. The FeMoco cluster therefore expands too much when a single O^{2-} anion is present. Interestingly, we have also tried to place molecules such as OH^-, H_2O, and NH^{2-} in the center of the cluster, and the FeMoco also expands substantially. Therefore, consistent with experimental analysis, we discount diatomic or solvent molecules also. Both our best N^{3-} model shown in Figure 21 and C^{4-} produce Fe−N and Fe−C distances in reasonable accord with the X-ray data, and we cannot discriminate between them solely on the basis of the calculated structures.

Table 3. Averaged Bond Distances (Å) of the FeMocoX ($X = C^{4-}$, N^{3-}, O^{2-}) Cores[a]

bond type	$6Fe^{2+}Fe^{3+}$				$4Fe^{2+}3Fe^{3+}$				expt
	C	N	O	vacancy	C	N	O	vacancy	
Mo−Fe	2.81	2.80	2.80	2.75	2.77	2.78	2.81	2.75	2.70
Fe−Fe	2.63	2.69	2.76	2.70	2.64	2.65	2.79	2.64	2.61
Fe−X[b]	2.02	2.03	2.17		2.01	2.02	2.11		2.00
Fe−Fe′	2.63	2.67	2.82	2.75	2.61	2.63	2.74	2.66	2.59
Fe′−Fe′	2.76	2.71	2.75	2.70	2.70	2.69	2.74	2.66	2.66

[a] All calculations carried out for the spin-coupled state BS6-1 were defined previously. [b] Fe−X is the average of all six coordinated Fe−X and Fe′−X distances.

As compared to our previous calculations, where calculated Fe−Fe distances were longer than experiment when there was no central anion, the Fe−Fe distances across the central waist contract slightly when a C^{4-} or N^{3-} anion is present. The presence of the central atom would appear to play an important geometric role in constraining the 6Fe prismane core.

The X-ray data suggest that the central atom sits fairly equally displaced in the 6Fe prism. All Fe sites therefore now appear to be four coordinate and no longer display the unusual trigonal coordination, as was suggested originally. Our calculations indicate that the N^{3-} anion lies closer to sites Fe3 and Fe4, rather than being equally displaced between all six irons of the core. An asymmetrically located central atom was also observed in recent calculations of the protonated and reduced states of the FeMoco. Here, a single proton sitting in the central cavity also favored site Fe4. However, in both cases, the same spin-coupling pattern was used in the calculations. It is likely that the position of the N^{3-} anion and the resultant Fe−N bond distances arise due to the specific pattern of up and down majority site spin vectors employed and that the pattern of Fe−N bond distances will vary in accord with the spin-coupling pattern.

Calculations for the FeMoco at the two most probable resting oxidation states, $Mo^{4+}4Fe^{2+}3Fe^{3+}$ and $Mo^{4+}6Fe^{2+}1Fe^{3+}$, give similar structural trends,

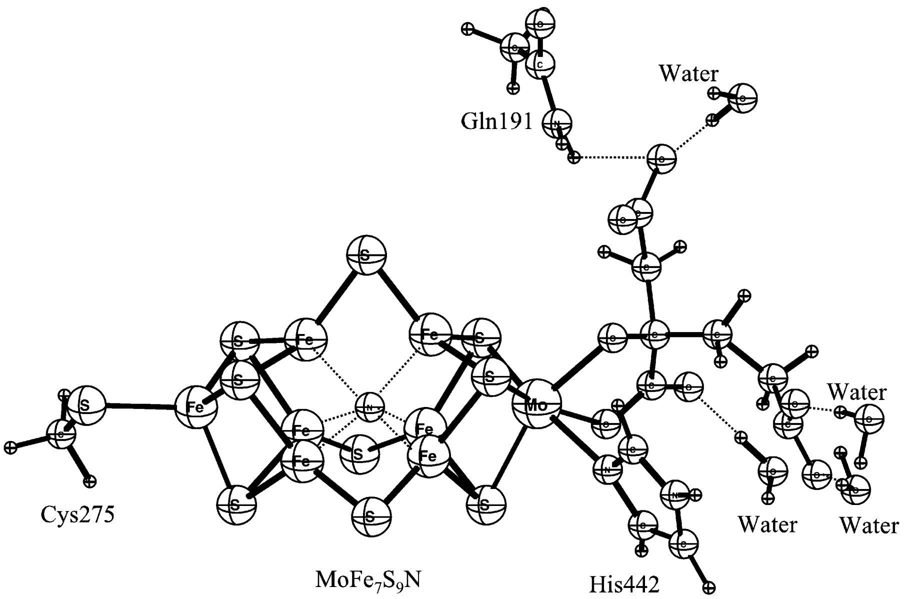

Figure 21. Optimized FeMoco structure at the $Mo^{4+}4Fe^{2+}3Fe^{3+}$ oxidation level. The N^{3-} atom is shown in the center of the cluster. Gas-phase DFT geometry optimization of the entire large cluster shown was used.

Table 4. Calculated Redox Potentials (V) for Redox Transition (Oxidized FeMoco + e$^-$ → Resting FeMoco)

redox transition[a]	charge changes on redox[b]	IP (eV)	ΔE_{pr} (eV)	redox potential (eV)
$Mo^{4+}5Fe^{2+}2Fe^{3+}N^{3-} + e^- \rightarrow Mo^{4+}6Fe^{2+}1Fe^{3+}N^{3-}$	$-6 + -1 \rightarrow -7$	−10.35	+12.56	−2.21
$Mo^{4+}3Fe^{2+}4Fe^{3+}C^{4-} + e^- \rightarrow Mo^{4+}4Fe^{2+}3Fe^{3+}C^{4-}$	$-5 + -1 \rightarrow -6$	−8.49	+11.61	−1.31
$Mo^{4+}3Fe^{2+}4Fe^{3+}N^{3-} + e^- \rightarrow Mo^{4+}4Fe^{2+}3Fe^{3+}N^{3-}$	$-4 + -1 \rightarrow -5$	−5.34	+9.96	+0.19
$Mo^{4+}5Fe^{2+}2Fe^{3+} + e^- \rightarrow Mo^{4+}6Fe^{2+}1Fe^{3+}$	$-3 + -1 \rightarrow -4$	−2.52	+7.76	+0.82
$Mo^{4+}3Fe^{2+}4Fe^{3+}O^{2-} + e^- \rightarrow Mo^{4+}4Fe^{2+}3Fe^{3+}O^{2-}$	$-3 + -1 \rightarrow -4$	−2.45	+7.85	+0.97
$Mo^{4+}3Fe^{2+}4Fe^{3+} + e^- \rightarrow Mo^{4+}4Fe^{2+}3Fe^{3+}$	$-1 + -1 \rightarrow -2$	+2.08	+3.65	+1.30
expt.				−0.042[c]

[a] All redox potentials were calculated using $\Delta E_{redox}° = IP + \Delta E_{pr} - 4.43$ V. [b] For comparison with the P cluster of the same protein, omitting or neutralizing the carboxylates of the homocitrate would change the charge on FeMoco by +2 in each case. [c] Measured for *A. vinelandii.*

in that O^{2-} seems unlikely to be the central ligand due to a larger overall geometric expansion of the cluster, while C^{4-} and N^{3-} cannot be distinguished by bond length comparisons with the X-ray data alone. The more oxidized $Mo^{4+}4Fe^{2+}3Fe^{3+}$ state shows a slight contraction both in FeMoco cluster size and in Fe−X (X = C^{4-}, N^{3-}, or O^{2-}) distances relative to the $Mo^{4+}6Fe^{2+}1Fe^{3+}$ reduced state, and, in that sense, there is a small improvement in overall geometric correlation with the 1.2 Å structure for the more oxidized assignment of metal-ion valencies.

On the basis of the resolution-dependent electron-density profile and the fact that nitrogenase interacts with dinitrogen to make ammonia, Einsle et al.[188] proposed that it was reasonable to assign the central ligand as a nitrogen atom. Recently, plane-wave DFT calculations by Hinnemann and Nørskov and DMol calculations by Dance[201] also examined the various possibilities that the light element in the center of the cofactor could be carbon, nitrogen, or oxygen. Comparing those works with our own, there are some relevant differences in approach. Hinnemann and Nørskov considered a smaller active site model in the gas phase only and compensated for the additional charge of the central X ligand (X = C^{4-}, N^{3-}, or O^{2-}) by an equal number of protons on the cluster sulfurs (and on Fe for C^{4-}). By contrast, we have performed calculations on a larger active site model for which the central anion increases the cluster's negative charge as compared to a central vacancy model, and energetics are assessed by redox potential calculations in the protein and solvent environment. After consideration of the O and N possibilities, Dance, as well as Hinnemann and Nørskov, suggested the most likely resting state for an atom-centered FeMoco was $Mo^{4+}4Fe^{2+}3Fe^{3+}(\mu_6\text{-}N^{3-})$. Nevertheless, the results of Hinnemann and Nørskov's and Dance's calculations, which were favorable for a nitride anion from both a structural and an energetic perspective, agree structurally with that presented and add support to the crystallographic assignment.

In Table 4, calculated redox potentials in the protein environment are presented for the interconversion between two states of the FeMoco, from the resting $S = {}^3/_2 = M^N$ state to a state that is one-electron oxidized $S = 1 = M^{OX}$ relative to the resting enzyme. Calculated redox data are presented for several independent processes that could represent the observed redox event, FeMoco(oxidized) + e$^-$ → FeMoco(resting), along with the measured value of −0.042 V in *Azotobacter vinelandii*.[202]

In our early work, using the metal-ion valence assignments based on the ENDOR data, we reported the calculated redox potential for the process, $Mo^{4+}5Fe^{2+}2Fe^{3+} + e^- \rightarrow Mo^{4+}6Fe^{2+}1Fe^{3+}$, to be +0.82 eV. On the basis of metal-ion valence assignments from

Mössbauer data, the more oxidized redox potential, described by $Mo^{4+}3Fe^{2+}4Fe^{3+} + e^- \rightarrow Mo^{4+}4Fe^{2+}3Fe^{3+}$, was calculated to be +1.30 eV. Since those previous efforts to calculate the redox potential, we have tried several different approaches to obtain a more accurate value. These have included calculations of FeMoco with a deprotonated imidazole ring bound to molybdenum, exploring coupled redox events involving protons on the homocitrate or the imidazole ring and electrons on the molybdenum−iron cluster, incorporating different protonation states of the surrounding protein amino acid side chains, and variations in the density functional and electrostatics methodology employed. None of these approaches reproduced the observed redox potential within an error margin of a few tenths of an electronvolt.

The incorporation of a N^{3-} anion in the center of the FeMoco now gives us a chance to evaluate this finding energetically with respect to the redox data. From Table 4, it is immediately clear that the redox process described by $Mo^{4+}3Fe^{2+}4Fe^{3+}N^{3-} + e^- \rightarrow Mo^{4+}4Fe^{2+}3Fe^{3+}N^{3-}$, calculated to be +0.19 eV, although not perfect, is in much better agreement with the experimental value. This contrasts to that for the redox process described by $Mo^{4+}5Fe^{2+}2Fe^{3+}N^{3-} + e^- \rightarrow Mo^{4+}6Fe^{2+}1Fe^{3+}N^{3-}$, where the calculated value of −2.2 V is far too negative. Our new calculated value for the FeMoco redox process, in which $Mo^{4+}4Fe^{2+}3Fe^{3+}N^{3-}$ are the favored valence assignments in the resting state, is much improved over the previous assignment of $Mo^{4+}6Fe^{2+}1Fe^{3+}$ with a central vacancy, and, as can be seen in Figure 22, this value now falls more in line with the results of redox potentials we have calculated for other iron−sulfur proteins.

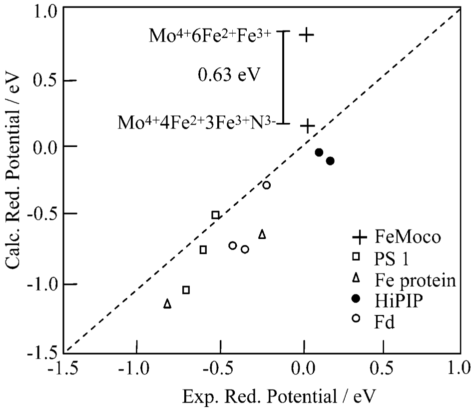

Figure 22. Plot of calculated FeMoco redox potential versus experiment. For comparison, redox potentials calculated for a range of iron−sulfur proteins are also shown.

As noted previously, although oxygen is unlikely as a central ligand, we cannot rule out a carbon anion on the basis of Fe−C distances alone, as they were effectively indistinguishable from the Fe−N distances observed both in the geometry optimizations and in the high-resolution X-ray data. In this context, we have also evaluated the redox potentials for the FeMoco clusters with O^{2-} and C^{4-} in the center at the $Mo^{4+}4Fe^{2+}3Fe^{3+}$ level. Along with the redox data for the FeMoco models with a central N^{3-} anion, these are shown in Table 4 and Figure 23. The most striking feature of Figure 23 is that the redox potential calculated for $Mo^{4+}3Fe^{2+}4Fe^{3+}C^{4-} + e^- \rightarrow Mo^{4+}4Fe^{2+}3Fe^{3+}C^{4-}$, at −1.31 eV, is far too negative; that for $Mo^{4+}3Fe^{2+}4Fe^{3+}O^{2-} + e^- \rightarrow Mo^{4+}4Fe^{2+}3Fe^{3+}O^{2-}$ is too positive.

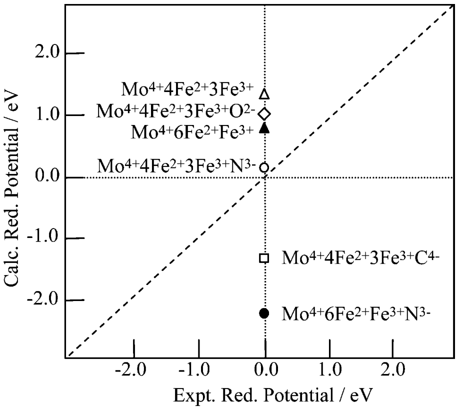

Figure 23. Correlation of calculated versus experimental redox potential for the FeMoco. Points in the upper left quadrant arise from FeMoco cluster charge changes ranging from −1 to −5; those in the lower right quadrant derive from charge changes ranging from −5 to −7.

Combined with the geometric criteria, these calculated redox values further enable us to discount both O and C as the central anion (as Einsle et al.[188] did previously on the basis of simple chemical arguments). More importantly, these incorrect redox potentials for O and C in the center of the FeMoco illustrate the usefulness of redox potential calculations in providing an energetic measure of the correctness of structure.

The calculated potentials in Table 5 are clearly dependent on the total charges associated with the two FeMoco clusters involved in the redox event. As these clusters become progressively more negatively charged, so too do the calculated redox and ionization potentials; the change in the environmental contribution (ΔE_{pr}) to the redox process also increases with increasing negative charge. Considering when only the N^{3-} anion is present in Table 5, as electrons are removed from the FeMoco, the cluster stabilizes due to a larger number of ferric−ferric pairs and the increased single-ion exchange energy associated with the ferric sites. As the resting FeMoco becomes increasingly more reduced, the total charge on the cofactor increases from −5 to a maximum of −7 and the interaction energy of the cofactor with the protein

Table 5. Gas-Phase and Protein Interaction Energies of the FeMoco Oxidation States

oxidation states	total charge[a]	gas phase (eV)	E_{pr} (eV)
$6Fe^{2+}1Fe^{3+}N^{3-}$	−7	−411.7835	−54.85
$5Fe^{2+}2Fe^{3+}N^{3-}$	−6	−422.1369	−42.29
$4Fe^{2+}3Fe^{3+}N^{3-}$	−5	−430.6144	−31.09
$3Fe^{2+}4Fe^{3+}N^{3-}$	−4	−435.9511	−21.13
$6Fe^{2+}1Fe^{3+}$	−4	−426.6996	−20.92
$5Fe^{2+}2Fe^{3+}$	−3	−429.2124	−13.10
$4Fe^{2+}3Fe^{3+}$	−2	−428.7386	−7.46
$3Fe^{2+}4Fe^{3+}$	−1	−426.6522	−3.81

[a] For comparison with the P cluster of the same protein, omitting or neutralizing the carboxylates of the homocitrate would change the charge on FeMoco by +2 in each case.

and solvent environment increases dramatically. It therefore appears that it is the interplay of these two competing terms that regulates the calculated redox potentials, and, in this respect, assigning the correct charge to the FeMoco cluster is essential to properly describe the redox energetics.

Furthermore, the trend in redox potential as a function of the cofactor charge enables us to estimate the redox potential for a variety of oxidation states and central ligands. For example, the redox process described by $Mo^{4+}5Fe^{2+}2Fe^{3+}O^{2-} + e^- \rightarrow Mo^{4+}6Fe^{2+}1Fe^{3+}O^{2-}$ involves changes in charge of $(-5) + (-1) \rightarrow (-6)$. By comparison with redox potentials of the same charges in Table 4, the calculated redox potential should therefore be around −1.3 eV. For $Mo^{4+}5Fe^{2+}2Fe^{3+}C^{4-} + e^- \rightarrow Mo^{4+}6Fe^{2+}1Fe^{3+}C^{4-}$, intrinsic cluster charges of $(-7) + (-1) \rightarrow (-8)$ must yield a redox potential that is much more negative than −2.2 eV. Both values are sufficiently far removed from the experimental value of −42 mV in *Azotobacter vinelandii* that they can be excluded.

Another potential class of models would involve a more reduced $Mo^{4+}6Fe^{2+}Fe^{3+}$core with a central atom (C, N, O), but with the extra charge compensated for by protonation, most probably at the μ^2S atoms. The two clearest examples of this would involve an O^{2-} or N^{3-} as the central anion and one or two added protons, respectively. Both models would exhibit the same overall total cluster charge of −5. As similarly charged clusters are likely to give comparable redox potentials, the predicted redox potentials should also prove to be around +0.2 eV, as was found for $Mo^{4+}4Fe^{2+}3Fe^{3+}N^{3-}$ without the protons (Table 6 and Figure 23). Such models may also be viable candidates for the resting FeMoco.

Table 6. Experimental and Calculated ^{57}Fe Isomer Shifts (mm s^{-1}) for the FeMoco Cluster

oxidation state	total charge[a]	range	average
$6Fe^{2+}1Fe^{3+}N^{3-}$	−7	0.49−0.62	0.54
$4Fe^{2+}3Fe^{3+}N^{3-}$	−5	0.41−0.60	0.48
$6Fe^{2+}1Fe^{3+}$	−4	0.21−0.40	0.30
$4Fe^{2+}3Fe^{3+}$	−2	0.10−0.35	0.24
expt.		0.33−0.50	0.40[b]

[a] All isomer shifts were derived from a linear fit (−0.51(nuclear density − 11 890.0) + 0.36) of 1Fe, 2Fe, and 4Fe S-phenyl and S_2-*o*-xylyl group model compounds to iron−sulfur protein isomer shift data. [b] Measured at 4.2 K for the resting state of the enzyme ($S = ^3/_2$).

As a further test, we have also examined the geometry of $Mo^{4+}6Fe^{2+}Fe^{3+}O^{2-}H^+$ core, shown in Figure 24, along with its unprotonated $Mo^{4+}6Fe^{2+}Fe^{3+}O^{2-}$ counterpart, the experimental structure, and our calculated structure of $Mo^{4+}4Fe^{2+}3Fe^{3+}N^{3-}$. For the $Mo^{4+}6Fe^{2+}Fe^{3+}O^{2-}$ core, although Fe−μ^2S distances of 2.26 Å on average agree reasonably well with those of the X-ray structure (2.22 Å), longer average Fe−Fe′ (2.82 Å) and Fe−O (2.17 Å) distances, along with its redox potential (estimated on the basis of charge to be about −1.3 eV), make it an unlikely option.

By protonating one of the μ^2S atoms, as noted previously, the charge on the cluster would seem to be right to give a reasonable redox potential. However, then the two Fe−μ^2S(H) bonds lengthen to 2.35 and 2.38 Å, much longer than the other four Fe−μ^2S bonds, which range from 2.23 to 2.25 Å. The equivalent bonds in the X-ray data display a range of 2.17−2.26 Å and an average of 2.22 Å, which are consistent with no protonation. Calculated Fe−O (2.11 Å) and Fe−Fe′ (2.87 Å) distances are also longer on average than the equivalent experimental distances of 2.00 and 2.59 Å. Structurally, the $Mo^{4+}6Fe^{2+}Fe^{3+}O^{2-}H^+$ core is much poorer than our best model of $Mo^{4+}4Fe^{2+}3Fe^{3+}N^{3-}$, which displays *both* geometric (Fe−μ^2S$_{av}$ = 2.23 Å, Fe−N$_{av}$ = 2.02 Å, Fe−Fe′$_{av}$ = 2.63 Å) and redox (+0.19 eV) features consistent with experiment. A doubly protonated $Mo^{4+}6Fe^{2+}Fe^{3+}N^{3-}2H^+$ model would therefore also be unlikely as it would be expected to give similar or larger Fe−Fe′ and Fe−μ^2S distances as compared to the $Mo^{4+}6Fe^{2+}Fe^{3+}O^{2-}H^+$ core.

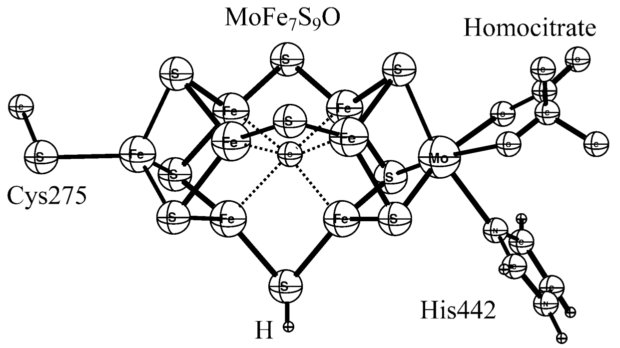

Figure 24. Optimized FeMoco structure at the $Mo^{4+}6Fe^{2+}Fe^{3+}$ oxidation level (a large part of the cluster, including the H-bonding waters and homocitrate, has been omitted for clarity). The O^{2-} is shown in the center of the cluster, and a single H^+ resides on a μ-2 sulfur.

Table 6 reports experimental isomer shift data, along with calculated isomer shift values for FeMoco for the two postulated oxidation state assignments, both in the absence and in the presence of the multiply charged N^{3-} ion in the center of the cofactor. Also reported is the total cluster charge for each set of oxidation state assignments.

Previously, for FeMoco with no central N^{3-} anion, the more reduced $Mo^{4+}6Fe^{2+}1Fe^{3+}$ oxidation state assignment was calculated to have an average isomer shift value of 0.30 mm s^{-1}; the corresponding value for the $Mo^{4+}4Fe^{2+}3Fe^{3+}$ metal-ion valence assignments was 0.24 mm s^{-1}. On the basis of the experimentally reported average of 0.40 mm s^{-1}, we concluded that the $Mo^{4+}6Fe^{2+}1Fe^{3+}$ oxidation state assignment was more likely to be correct. With the revised model that now incorporates the central N^{3-} anion, the calculated average isomer shift for $Mo^{4+}4Fe^{2+}3Fe^{3+}$ is 0.48 mm s^{-1}, closer to the average experimental value of 0.40 mm s^{-1}. By contrast, the $Mo^{4+}6Fe^{2+}1Fe^{3+}$ oxidation state assignment is now calculated to give an average isomer shift value of 0.54 mm s^{-1} and an error of 0.14 mm s^{-1}.

The trend in calculated isomer shift values is exactly what one would expect given electron counting arguments and charge transfer from nitride to iron. With no central N^{3-} anion, the ENDOR-based $Mo^{4+}6Fe^{2+}1Fe^{3+}$ valence assignments result in a cofactor with total charge of −4, and based on a comparison of calculated and observed average isomer shift values, our original conclusion was that the cofactor was electron deficient. Oxidation of two of the ferrous sites to ferric yielded the $Mo^{4+}4Fe^{2+}3Fe^{3+}$ model, which made the cofactor total charge −2 and rendered the cofactor even more electron deficient, such that the calculated average isomer shift values were further from those measured experimentally. The subsequent addition of the nitride ion, having a charge of −3, offsets the oxidation of two ferrous sites and also reduces the cofactor net charge by one extra negative unit, giving a cluster with an overall total charge of −5. The qualitative conclusion to be drawn is that, although the new $Mo^{4+}4Fe^{2+}3Fe^{3+}N^{3-}$ model is formally two electrons more oxidized than the original $Mo^{4+}6Fe^{2+}1Fe^{3+}$ model in terms of valence assignments of the iron sites, due to the addition of N^{3-}, the cofactor is, in fact, one electron more reduced overall. The seven iron sites must therefore be electron rich relative to the original ENDOR-based model, and this enables us to rationalize the trend in calculated average isomer shift in Table 6. However, it is also worth noting that, in the protein environment around FeMoco, there are several amino acid residues (Arg, Lys, His) lying close to the FeMoco that could easily accept charge donation from the cluster. These residues are not included in our quantum chemical model, but could well be the reason that our calculated average isomer shift data suggest the cluster is now somewhat too electron rich.

Overall, these new isomer shift estimates suggest that the oxidation state assignment of $Mo^{4+}4Fe^{2+}3Fe^{3+}N^{3-}$ is more compatible with experiment and a more reduced $Mo^{4+}6Fe^{2+}1Fe^{3+}N^{3-}$ cluster assignment is not required.

In Table 7, calculated Mulliken net spin densities are given for FeMoco clusters with C, N, or O in the center. The total net spin density on these central anions is very small for N^{3-} and O^{2-}, but slightly larger for C^{4-}. The calculated magnitude of the N^{3-} spin population is −0.02 of an electron, further broken down into total s (0.02) and total p (−0.04) contributions where $[p_x + p_y + p_z = 0.01 + (-0.05) + 0.00]$. This spin density distribution would give rise to a ^{14}N hyperfine signal that may be difficult to identify,[203] especially when one considers that FeMoco is hydrogen bonded to several amino acid side chains and main-chain peptides derived from arginine, glycine, and lysine, making the local protein environment relatively nitrogen rich, and all of which may mask any potential spectroscopic signal. Lee et al.[189] have recently observed no new ^{15}N signals or changes in ^{14}N hyperfine spectra during ENDOR and ESEEM experiments under catalytic turnover with $^{15}N_2$. This is consistent with a stable central ligand that is not exchangeable, which argues against the dinitrogen substrate being the source of a central N.

Table 7. Calculated Net Spin Density for the Central Anion of FeMoco

FeMoco model	net spin density
$Mo^{4+}4Fe^{2+}3Fe^{3+}C^{4-}$	−0.14
$Mo^{4+}4Fe^{2+}3Fe^{3+}N^{3-}$	−0.02
$Mo^{4+}4Fe^{2+}3Fe^{3+}O^{2-}$	−0.01

In summary, quantum chemical calculations have been used to examine which of three proposed atoms, C, N, or O, is present in the center of the active site of nitrogenase. The calculations yield structural, spectroscopic, and energetic evidence to corroborate the hypothesis that the central atom sitting in the six-iron prismane of the FeMoco is a N^{3-} anion, as was suggested recently by Rees and co-workers, and further reinforced by theoretical studies.[188,199,201] We also reach this conclusion on the basis of calculated Fe−N bond distances that are in very good agreement with the high-resolution X-ray data, a calculated redox potential of 0.19 eV that compares well with the experimental value of −0.042 V in the protein, for the process defined as $M^{OX} + e^- \rightarrow M^N$, or, in oxidation state terms, $Mo^{4+}3Fe^{2+}4Fe^{3+} + e^- \rightarrow Mo^{4+}4Fe^{2+}3Fe^{3+}$, and isomer shift calculations that suggest a metal-ion valence assignment of $Mo^{4+}4Fe^{2+}$-$3Fe^{3+}$ for the resting state. Furthermore, in the presence of the N^{3-} anion, the homocitrate anion is stable in the $Mo^{4+}4Fe^{2+}3Fe^{3+}$ state; our earlier DFT calculations[63] with a central vacancy produced spontaneous oxidation of the homocitrate to yield a terminal homocitrate radical, which is not observed experimentally. The incorporation of a central N^{3-} anion into the FeMoco raises many questions about both the cluster assembly and the catalytic reaction mechanism. Some of the most significant questions include how does the N^{3-} anion become incorporated into the center of the FeMoco, does the N^{3-} anion play any role in the catalytic cycle, perhaps in initial dinitrogen binding, or does it mainly serve a structural and electronic role in maintaining the integrity of the cluster during catalysis? A related major question is the location and nature of N_2 binding to the MoFe cluster active site. There has been significant recent progress on two fronts. Yandulov and Schrock[204] have developed a synthetic Mo molecular complex which catalytically reduces dinitrogen to ammonia at a single Mo site using chemical reducing agents and proton sources. In addition to being a major synthetic accomplishment, this achievement has been interpreted as favoring the Mo site of the MoFe nitrogenase protein as the site of N_2 binding. However, there is contrary evidence on this issue as well. Very recently, Seefeldt and co-workers[205] have found that the binding site of propargyl alcohol ($HCCCH_2OH$, having a C−C triple bond) in the α70Val → Ala mutant of the MoFe protein is localized to one 4Fe4S face of the FeMo cofactor cluster as shown by ^{13}C ENDOR spectroscopy. Because propargyl alcohol can be reduced by nitrogenase, and competes for electrons when N_2 or protons are present, and because the electronically related substrate acetylene is competitive for N_2 binding and reduction in the related α69Gly → Ser mutant, there are strong indications that all of these have the same binding site. In view of both of these developments, the site of N_2 binding is still an open question. Molecular modeling is well suited to be able to tackle such questions, and such issues will be the focus of future studies in several laboratories.

8. Iron–Oxo Mössbauer Parameters

Iron, with its large bioavailability and redox activity in the Fe^{2+} form, is an essential element for life on planet Earth.[206] As a consequence, iron is incorporated into many proteins and enzymes that perform critical biochemical functions.[173c] Among the binuclear non-heme iron proteins,[48] methane monooxygenase (MMO) and ribonucleotide reductase (RNR) are well-known, with the hydroxylase component of MMO (MMOH) catalyzing methane oxidation,[45,46,207] while RNR plays a key role in the synthesis of deoxyribonucleotides required by all living organisms.[208,209]

On the atomic level, MMO and RNR have strikingly similar active sites, and during the course of their distinct chemistries, it is clear that there are significant mechanistic elements in common over their reaction paths. Differences arise particularly in the active site reactivity with molecular oxygen, which constitutes a first branch point in the subsequent chemical reactions, discussed for the individual enzymes below. After this reaction branching, the catalytic mechanisms by which these two proteins perform their unique functions remain only partially understood at present, mostly because the highly prized structures of the key catalytic intermediates, which enable these two proteins to bring about different chemical reactions, are not yet known. A direct measure of the important structural elements of these key intermediates can be obtained in principle by protein X-ray crystallography, but a major obstacle is that the key intermediates are very short-lived, and it is difficult to stabilize the protein on a sufficiently long time scale to obtain crystals for diffraction studies. The catalytic mechanisms of MMO and RNR are therefore not easy to follow with a direct structural probe.

Spectroscopy generally provides a means of following catalytic reactions for which the structures of short-lived intermediates are not available. Mössbauer spectroscopy[210,211] typically takes hours or days for an accurate measurement of a biological sample, but the situation can be remedied somewhat by using the freeze-quench approach, which allows trapping of unstable and otherwise short-lived species.[212] Measured parameters such as isomer shift, quadrupole splitting, and metal and ligand hyperfine for ^{57}Fe sites then enable an indirect measure of many factors such as metal oxidation and spin state, the local chemical environment at the iron site, the electric field gradient, the occupation of iron d levels, and the degree of valence delocalization in mixed-valence systems. In combination with other spectroscopic techniques, these parameters allow models for the key intermediates to be proposed, and they also represent a yardstick by which postulated models and existing protein data can be examined and compared to known synthetic analogues.[47,213]

Prior to calculating isomer shifts and quadrupole splitting parameters of Fe atoms in protein active sites, a correlation between experimental isomer shifts ranging from 0.1 to 1.5 mm s^{-1} for Fe atoms in a known training set of complexes with the corresponding electron densities at the Fe nuclei in those complexes must first be established and validated. As μ-oxo diiron (Fe–O–Fe) and μ-hydroxo diiron (Fe–OH–Fe) units appear consistently in a number of dinuclear non-heme iron proteins, it is relatively easy to select a training set of molecules to establish a correlation that incorporates a range of synthetic dimeric iron complexes that display these structural features, as well as polar monomeric iron species. For all of the structures in the training set, measured isomer shift and quadrupole splitting data are available and allow the building of a linear relationship between the isomer shifts of Fe atoms for the synthetic complexes and their corresponding calculated nuclear densities (and for calculated and observed quadrupole splittings).

For isomer shifts, all electron calculations were used to calculate the electron density at the Fe nuclei, and then a linear correlation is constructed between measured isomer shifts and calculated electron densities for a series of synthetic high-resolution Fe complexes, whose coordinates were extracted from the Cambridge structural database.[213n] An isomer shift correlation for these 15 dinuclear iron–oxo, iron–hydroxyl, and iron–phenoxo type compounds plus 6 polar mononuclear Fe complexes (Figure 25) was constructed using the experimental geometries, and we have also calculated Mössbauer quadrupole splittings (QS) for the synthetic complexes cited above (Figure 26).[213n] The correlation equation between

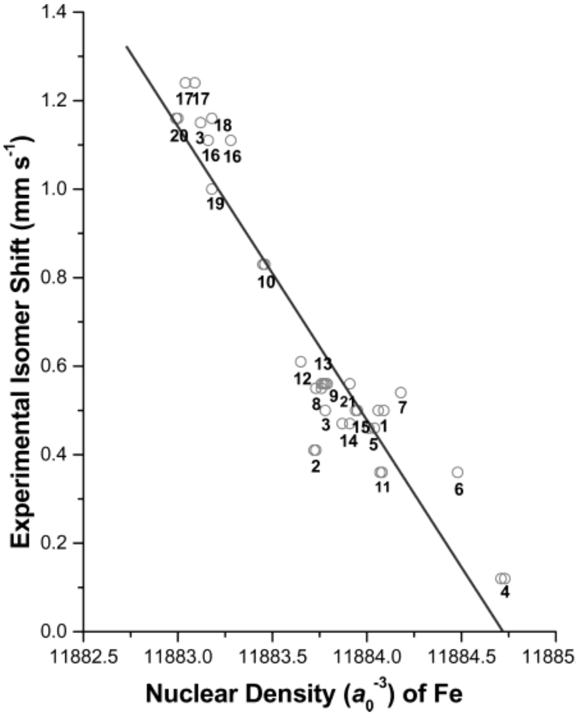

Figure 25. Plot of measured isomer shift versus calculated nuclear density for a range of synthetic iron–oxo complexes:[213n] (1) $Fe_2(OH)(OAc)_2(HBpz3)_2^{1+}$, (2) $Fe_2O(OAc)_2(bipy)_2Cl_2$, (3) $Fe_2BPMP)(OPr)_2^{2+}$, (4) $Fe_2O_2(5\text{-}Et_3\text{-}TPA)_2^{3+}$, (5) $Fe_2O(Me_3TACN)_2(Cl_4cat)_2$, (6) $FeCl_4^{1-}$, (7) $Fe(bipy)_2Cl_2^{1+}$, (8) $Fe_2(salmp)_2$, (9) $Fe_2(cat)_4(H_2O)_2^{2-}$, (10) $Fe_2(salmp)_2^{1-}$, (11) $Cl_3FeOFeCl_3^{2-}$, (12) FeF_6^{3-}, (13) $Fe_2O(OAc)_2(HBpz_3)_2$, (14) $Fe_3O(OAc)_2(Me_3TACN)_2^{2+}$, (15) $Fe_2O_2(6TLA)_2^{2+}$, (16) $Fe_2(salmp)_2^{2-}$, (17) $Fe_2(BPMP)(OPr)_2^{1+}$, (18) $Fe(Py)_4Cl_2$, (19) $FeCl_4^{2-}$, (20) $Fe_2(OH)(OAc)_2(Me_3TACN)_2^{1+}$, (21) $FeCl_6^{3-}$.

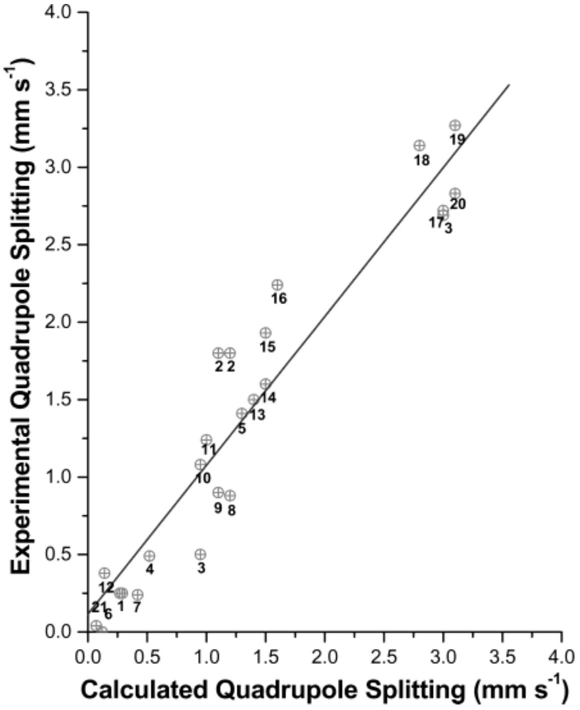

Figure 26. Plot of measured quadrupole splitting versus calculated quadrupole splitting for a range of synthetic iron−oxo complexes (see Figure 25).[213n]

isomer shifts δ and Fe nuclear densities $\rho(0)$ is

$$\delta = \alpha(\rho(0) - 11884.0) + C \tag{19}$$

where $\alpha = -0.664$ and $C = 0.478$.

The best fit equation gives a correlation coefficient $r = -0.94$ with a standard deviation (SD = 0.11 mm/s) with isomer shifts ranging from 1.2 to 0.14 mm/s, including Fe(II), Fe(III), and Fe(IV) (mainly high-spin metal sites, but including also the intermediate-spin ferromagnetically coupled $Fe_2O_2(5\text{-}Et_3\text{-}TPA)_2^{3+}$).[213n]

Calculated QS values are in very good agreement with experiment, with typical deviations in QS of rms of 0.3 mm s^{-1} (10−20%). With a linear fit, the standard deviation is 0.1 mm s^{-1} in QS.[213n] This level of accuracy will be quite valuable for distinguishing between DFT calculated structural and electronic models for intermediates including Q in MMOH and X in RNR, discussed in the following sections.

9. Methane Monooxygenase

Proteins that contain one or more transition metals as an important constituent of their active site (metalloproteins) play a crucial role in biology, particularly in processes involving coupled electron and proton transfer and where small molecules are chemically transformed.[173c] The family of binuclear non-heme iron proteins have attracted considerable interest during recent years due to the potential environmental, medical, and agricultural benefits that stand to be gained from a better understanding of the general principles governing their function and reactivity on the microscopic level. Several reviews[214] have thus appeared concerning different aspects of their molecular and electronic structures and biochemical functions.

Soluble methane monooxygenase (MMO) is a protein that belongs to a class of binuclear non-heme iron enzymes capable of activating dioxygen for further oxidation chemistry. The hydroxylase component (MMOH) of the MMO protein[215] found in methanotrophic bacteria[216] effectively catalyzes the reaction in which methane is converted to methanol and water in accord with the following set of reactions:

$$\mathrm{Fe(III)-(OH^-)_2-Fe(III) + 2e^- + 2H^+ \rightarrow 2Fe(II) + 2H_2O} \tag{20}$$

$$\mathrm{2Fe(II) + O_2 \rightarrow Fe(IV)-(\mu O)_2-Fe(IV)} \tag{21}$$

$$\mathrm{Fe(IV)-(\mu O)_2-Fe(IV) + R-H + H_2O \rightarrow Fe(III)-(OH^-)_2-Fe(III) + R-OH} \tag{22}$$

Methanotrophic bacteria are capable of metabolizing one of the most inert hydrocarbons, CH_4, as their sole source of carbon and energy, allowing for rapid growth in vivo. Thus, methanotrophic bacteria play an important environmental role in CH_4 consumption, by limiting its flow to the atmosphere via the conversion of methane into a more utilizable form. MMO participates in the global regulation of concentrations of this greenhouse gas. Apart from this obvious biological and ecological importance, MMO is also known to oxidize a broad range of hydrocarbons, leading to several other potential applications of the bacteria, but presently the mechanism by which MMO performs this unique conversion is only partly understood.

The overall catalytic cycle of MMOH is well-established. Coupled electron and proton addition to the Fe(III)Fe(III) resting enzyme generates the reduced Fe(II)Fe(II) state and crystal structures (active sites are shown in Figures 27 and 28) are available for both of these states of the cycle, shown in Figure 29.

Two spectroscopically observable intermediates, P and Q, are then formed upon reaction with dioxygen. P is a peroxo-Fe(III)Fe(III) intermediate. Q is the proposed high-valent Fe(IV)Fe(IV) species capable of oxidizing methane. Presently, no X-ray structure of the protein exists that contains inter-

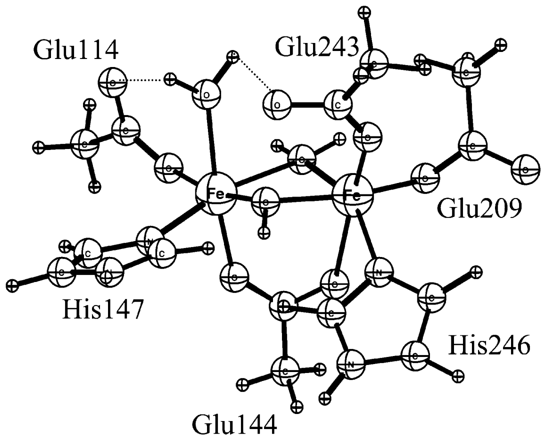

Figure 27. Structure of oxidized MMOH from *M. capsulatus*.

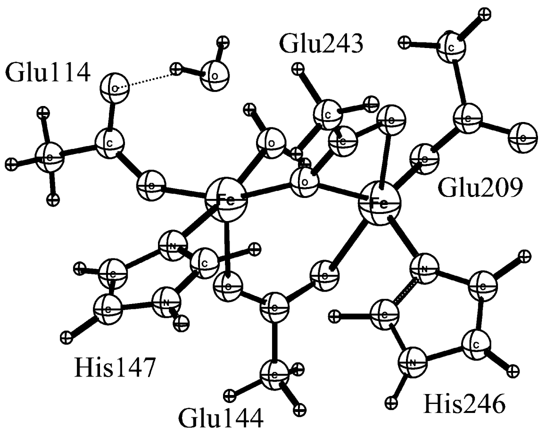

Figure 28. Structure of reduced MMOH from *M. capsulatus*.

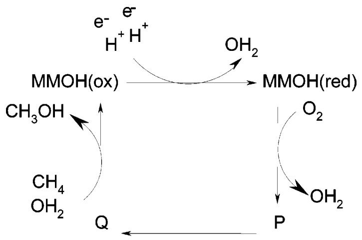

Figure 29. Simple catalytic cycle for methane monooxygenase. Reprinted with permission from ref 18. Copyright 2003 Elsevier.

mediate Q, and no Fe(IV)Fe(IV) model complexes with biologically relevant ligands have been stabilized in aqueous solution. The identity of intermediate Q is thus an unknown quantity but a topic of substantial interest.

Despite the collective experimental effort, structures of these intermediate species, P and Q, are not yet available, and, as a result, many questions regarding the possible mechanism(s) of catalysis still remain unanswered. As more experimental data become available concerning the structures of the intermediates, attention naturally turns toward understanding not only the operation of the catalytically active species in isolation, but also in the presence of the full protein and solvent environment, and how the combined features affect the interconversion of one intermediate into another during enzyme turnover.

Modern quantum chemical methods have been employed to model aspects of the MMO catalytic pathway.[217] Each successive study by authors such as Yoshizawa,[218] Morokuma−Basch,[219] Siegbahn,[217,220] and Friesner−Lippard[221] has provided significant insight into this complex system. Most of these studies have been focused toward identifying the structures and the related energetics associated with the formation and subsequent reactions of the presently unknown key intermediates, P and Q. The differences in the various approaches along with the latest findings from quantum chemical studies for MMO are reviewed in the excellent recent work by Baik et al.[215]. Rather than repeat these topics, as part of this review, we will briefly mention some of our efforts in the intermediate Q area where the focus is on the electronic structure and spectroscopic properties of potential Q structures.

Our initial calculations for intermediate Q of MMOH,[222] the proposed high-valent Fe(IV)Fe(IV) species capable of oxidizing methane in the catalytic cycle of MMO, have been largely guided by the spectroscopic data.

Freeze-quench trapping techniques coupled with Mössbauer and EXAFS spectroscopies have provided the most insight into possible structures for Q.[223] Mössbauer data indicate that Q exhibits diamagnetism at high magnetic field strength[223a] and comprises two near-equivalent Fe(IV) sites that are antiferromagnetically coupled ($J < -30$ cm^{-1}).[223b,c] XAS experiments on *M. trichosporium* indicate preedge areas consistent with Fe coordination numbers of five or lower.[223d] EXAFS spectra from *M. trichosporium* upon analysis indicate a diamond core (Fe_2O_2) exists comprising one short (1.77 Å) and one long (2.06 Å) μO bond to each Fe and an Fe−Fe distance ranging from 2.46 to 2.52 Å.[223d,e]

In attempting to construct a quantum chemical model that accurately represents intermediate Q, our working hypothesis was that the active site cluster be consistent with most of the experimental observations noted above. We evaluated previously suggested structural models by Gherman[221e] (Figure 30a) and Siegbahn (Figure 30b),[220b,g] and the two bidentate bridging carboxylate model produced the shorter iron−iron distance and was more consistent with the EXAFS metric.

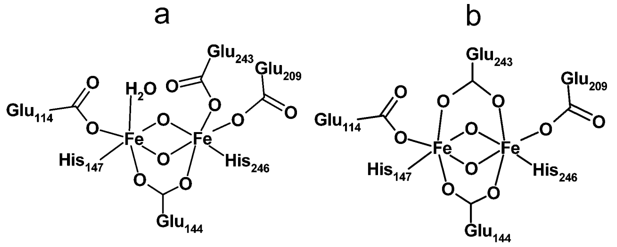

Figure 30. MMOH-Q models suggested by (a) Gherman et al.[221e] and (b) Siegbahn.[220b,g]

On the basis of our calculations, an intermediate-spin ferromagnetically coupled state was found to be the ground state for the Gherman model,[221e] as compared to the high-spin antiferromagnetically coupled state for Siegbahn's model.[220b,g] Both models have iron coordination numbers of six, in contrast to the X-ray absorption spectral analysis, which indicates both irons are five coordinate. Even though in these small structural models the Gherman model was apparently lower in energy than the Siegbahn model, the catalytic reaction need not necessarily proceed through the lowest energy pathway, either because of second- and third-shell ligand interactions or because of other protein and solvent effects. On the basis of agreement with measured spectroscopic parameters such as structural information and spin state, we chose Siegbahn's model as our starting basis to build a large quantum model of Q containing 102 atoms (Figure 31) that incorporates a number of

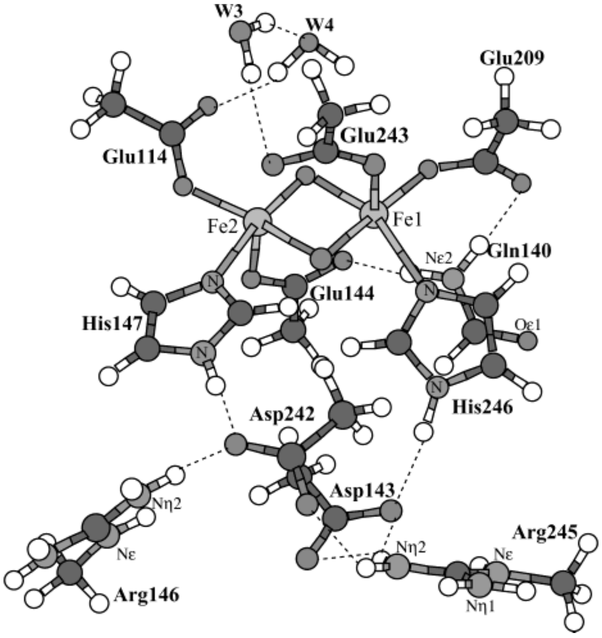

Figure 31. Our large more open (LHLN) model[222] for intermediate Q related to that of Siegbahn.[220b,g]

second- and third-shell amino acid residues (Asp143, Asp242, Gln140, Arg245, and Arg146). These residues were incorporated on the basis of a breakdown of the protein field electrostatics for the oxidized and reduced MMOH clusters,[213i] as they appeared to be structurally, electrostatically, and, therefore, energetically significant.

This large more open model resembles Siegbahn's,[220b,g] but with $2H_2O$ and Gln amide H bonds to Glu.[222] We will refer to this as the Lovell−Han−Liu−Noodleman (LHLN) model below. The primary goal of developing this model that complements the work of Siegbahn[220b,g] and Gherman et al.[221e] was to evaluate how the properties of the active site were governed by the spin state ($S = 2$, high-spin (HS), or $S = 1$, intermediate-spin (IS)) of the individual Fe sites when second- and third-shell amino acid ligands were present. In this way, the main long-range protein and solvent environment effects are kept within the quantum mechanics. The characteristic features of Q guiding evaluation of the calculations are the geometry (Fe−Fe distance) and Fe coordination number, Fe net spin populations, relative energies between spin states (but not between models as other workers have), the exchange coupling between the two Fe sites, and Mössbauer parameters.

Our LHLN model displays two strongly AF-coupled ($J_{\mathrm{calc}} = -376$ cm^{-1}) five-coordinate HS Fe sites separated by 2.63 Å with a small asymmetry in the Fe−O distances.[222] While the properties of this cluster are consistent with Mössbauer and XAS spectroscopy,[223e] the calculated Fe−Fe distance is longer than the EXAFS-derived range (2.46−2.52 Å).[223d,e] EXAFS is often quite accurate for Fe−ligand and Fe−Fe distances; however, errors of up to 0.2 Å as compared to subsequent X-ray structures have been found for Fe−Fe distances in some cases. We also obtained a state in which two intermediate-spin, six-coordinate, AF-coupled ($J = -118$ cm^{-1}), asymmetrically bridged Fe sites are separated by 2.42 Å, and this lies +7.5 kcal/mol higher in energy and +11 kcal/mol higher after spin-projection corrections to the energies.[224]

Although it has been established[223b,c] that both iron atoms in the reactive intermediate **Q** are in an oxidation state of IV, neither the structural arrangement of the first-shell ligands around the Fe_2O_2 core nor the electronic configuration is known exactly. In principle, the four metal-based electrons of the d^4-Fe(IV) configuration at each metal center can adopt three different spin states, "low-spin" (LS), "intermediate-spin" (IS), and "high-spin" (HS). In addition, the orientation of the unpaired electrons at the iron centers to each other gives rise to a second degree of freedom resulting in either a ferromagnetic (F) or antiferromagnetic (AF) spin-coupling of the diiron centers for the IS and HS cases. Experimentally, antiferromagnetic behavior is observed in Mössbauer studies of the intermediate **Q** with a coupling constant of $J < -30$ cm^{-1}. These measurements strongly suggest high-valent iron centers with unpaired electrons that couple with one another, ruling out the LS case. The LS state for Fe(IV) is also intuitively unlikely given that, to date, not one example of a complex displaying a low-spin d^4-Fe(IV) configuration is known. Further, both the average Fe site isomer shift and quadrupole splitting are calculated to be in better agreement with experiment for AF coupling of HS than IS Fe sites.

The most significant point to emerge from our calculations is that the presence of HS metal ions and a very short Fe−Fe separation as well as substantial asymmetry in the Fe−O bond lengths (from EXAFS) are very clearly mutually incompatible. The values of J calculated are, however, in reasonable accord, both in sign and in magnitude, with the estimation from Mössbauer spectroscopy ($J < -30$ cm^{-1}) and that calculated by Gherman et al. ($J = -143$ cm^{-1}).[221e] More extensive studies in the protein on the properties of alternative electronic states will prove extremely useful.

To not bias our results in favor of one model over another, we also examined a larger cluster (Figure 32) similar to that proposed by Friesner and Lippard (Gherman et al.),[221e] incorporating the same second-shell ligands as in the larger LHLN model.[225]

In the larger Friesner−Lippard model, high-spin antiferromagnetically coupled iron sites are preferred in the ground state in contrast to intermediate-spin ferromagnetically coupled sites in the smaller model (Figure 30a). Clearly, the environment affects the stabilization of one spin state over another in these binuclear systems. The calculated iron−iron distance is larger in the larger Friesner−Lippard model than in the large LHLN model by 0.06 Å (2.69 Å), and a much larger difference between the isomer shifts calculated for the iron sites in the larger Friesner−Lippard model ($\Delta\delta = 0.46$ mm/s) is present as compared to LHLN model ($\Delta\delta = 0.28$ mm/s) and that measured experimentally ($\Delta\delta = 0.04$ mm/s). This is consistent with the greater difference in Fe coordination geometry for the two sites in the Friesner−

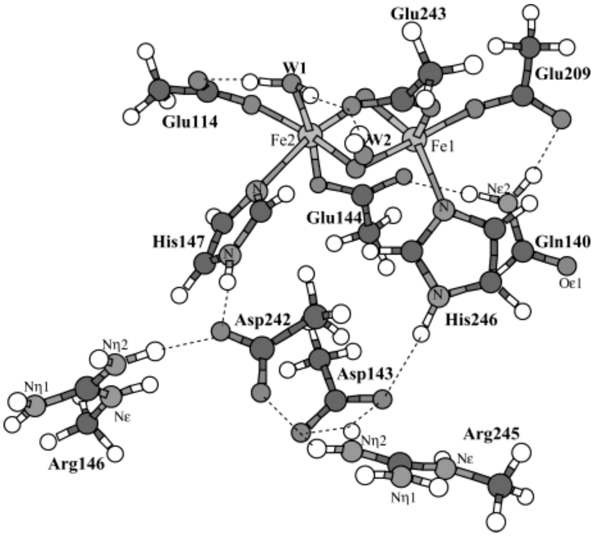

Figure 32. Our large model for intermediate Q related to that of Friesner and Lippard.[221e]

Lippard model as compared to the LHLN model. From these spectroscopic calculations, the LHLN model matches better than the Friesner and Lippard model. However, in both models, the presence of HS metal ions and a very short Fe−Fe separation as well as substantial asymmetry in the Fe−O bond lengths (from EXAFS) are very clearly mutually incompatible. Given the ability of DFT-based methods to predict relatively accurate bond lengths, if the Fe sites in intermediate Q are really of high-spin configuration, it is surprising that the calculated Fe−Fe separation is so inaccurate. Further tests of alternative large quantum cluster Q models with treatment of the extended protein/solvent environment by SCRF-based and related methods are planned.

10. Ribonucleotide Reductase

Ribonucleotide reductase (RNR) catalyzes the reduction of ribonucleotides to deoxyribonucleotides.[214b,226] This is the first step in the required biosynthesis of DNA. Although different classes of this enzyme differ in composition and cofactor requirements, they display a reaction mechanism with a common theme using metals and free radical chemistry. For a review on metal-containing radical enzymes, the reader is referred to the work of Himo and Siegbahn.[15d]

The class I RNRs consist of a homodimer of two dissimilar protein subunits, R1 and R2, in an overall $\alpha_2\beta_2$ tetramer. Subunit R1 contains the substrate binding site, and R2 contains one binuclear iron cluster which generates and stabilizes a radical at tyrosine 122 (Tyr122). This radical functions as a “pilot light” which begins the catalytic reaction via long-range proton-coupled electron transfer to generate a thiyl radical on cysteine 439 (Cys439) of the R1 subunit, which then performs the ribonucleotide reduction.[214c,227] The Tyr122 radical has been identified in the oxidized deprotonated form and is stable for days at room temperature.[1] Once the Tyr122 radical is lost, the enzyme becomes inactive, but the active form can be regenerated by two-electron reduction from a reductase protein followed by O_2 binding. During the formation of active R2, a transient species (intermediate X) is formed that oxidizes tyrosine to the stable radical form.[228] The overall net reaction cycle is given by

$$\mathrm{Fe(III)}(\mu\mathrm{O})(\mathrm{OH}_n)\mathrm{Fe(III)-Tyr122-OH} + 2\mathrm{e}^- + (4-n)\mathrm{H}^+ \rightarrow \mathrm{Fe(II)Fe(II)-Tyr122-OH} + 2\mathrm{H_2O} \quad (23)$$

$$\mathrm{Fe(II)Fe(II)-Tyr122-OH} + \mathrm{O_2} + \mathrm{e}^- + n\mathrm{H}^+ \rightarrow \mathrm{Fe(III)}(\mu\mathrm{O})(\mathrm{OH}_n)\mathrm{Fe(IV)-Tyr122-OH} \quad (24)$$

$$\mathrm{Fe(III)}(\mu\mathrm{O})(\mathrm{OH}_n)\mathrm{Fe(IV)-Tyr122-OH} \rightarrow \mathrm{Fe(III)}(\mu\mathrm{O})(\mathrm{OH}_n)\mathrm{Fe(III)-Tyr122-O}^{\bullet} + \mathrm{H}^+ \quad (25)$$

where $n = 1$ or 2 in eqs 23−25. Presently, the structure for the active form of the protein that contains the Tyr122 radical is unknown, but X-ray structures of RNR from *E. coli* are available for both the reduced (Figure 33) and the oxidized (met) (Figure 34) forms.[229]

In the diferrous cluster, both carboxylate groups from Glu238 and Glu115 exist in a bridging position between the two irons. Upon interaction with an O_2 molecule and the subsequent oxidation reaction, the carboxylate of Glu238 changes from the bidentate position to monodentate binding with Fe2. Meanwhile, a water molecule binds to Fe1 which H-bonds with Glu238. One oxygen atom from O_2 is reduced

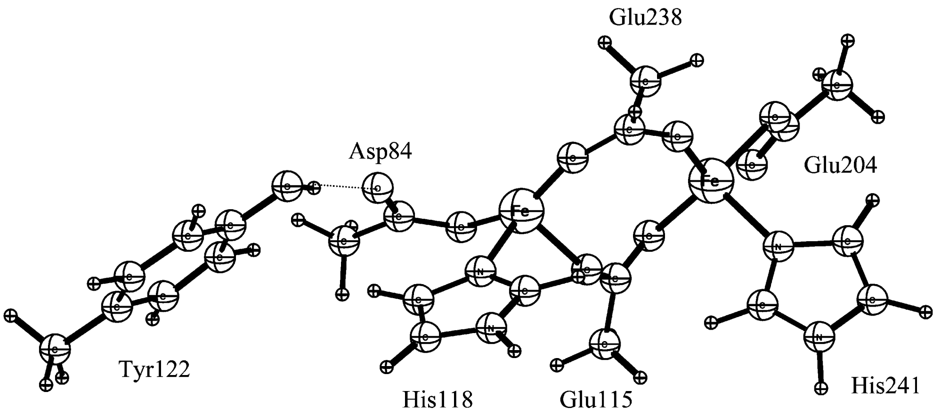

Figure 33. Core structure of reduced RNR from *E. coli*.

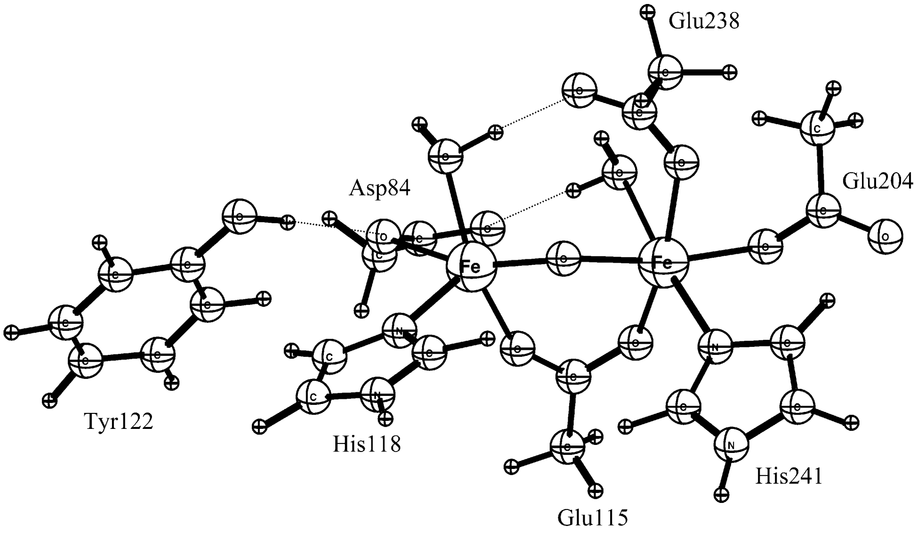

Figure 34. Core structure of oxidized RNR from *E. coli*.

to H_2O, and the other is incorporated as a bridging oxo in the diferric form. In addition, the carboxylate of Glu204 undergoes a shift from a bidentate to monodentate ligation of Fe2. The carboxylate of Asp84 shifts from a monodentate to approximate bidentate ligation of Fe1 with the production of Tyr122 radical, and Asp84 also H-bonds with a water molecule coordinated to Fe2.

Theoretical DFT geometric and energetic studies on the oxidized and reduced RNR R2 active site, and the interactions between the active site and the protein environment, have been reported in refs 18 and 213i. Here, we will focus on the studies of the RNR intermediate state X. Although there has been a significant experimental attempt to elucidate the structure of this short-lived catalytic species, the detailed structure of intermediate X is still not clear.[230] The accumulated experimental evidence now enables a reasonable picture of X to be established. Mössbauer data indicate the iron centers of X are high-spin Fe(III) ($S = {}^{5}/_{2}$) and high-spin Fe(IV) ($S = 2$) sites that antiferromagnetically couple to give an $S_{\text{total}} = {}^{1}/_{2}$ ground state.[227] X is therefore best described as a spin-coupled Fe(III)−O−Fe(IV) system that displays no Tyr122 radical. A short Fe−Fe distance of 2.5 Å has been identified by EXAFS for X in both wild-type and mutant Y122F proteins.[230c] On the basis of this metric, possible core structures for X have been proposed, and these are shown in Figure 35.[223e]

Experimental data support the existence of at least one μ-oxo bridge in the core structure of X, but, beyond this, other elements that may be present include terminal or bridging solvent-based ligands and monodentate and/or bidentate bridging carboxylate groups from glutamate (Glu) protein residues. Recently, on the basis of CW and pulsed Q-band ^{17}O-ENDOR experiments, as well as other ENDOR and EXAFS observations, Burdi et al. proposed a structure for X, containing two oxygen atoms, both initially derived from O_2, with one present as a μ-oxo bridge and one as a terminal aqua ligand.[230e]

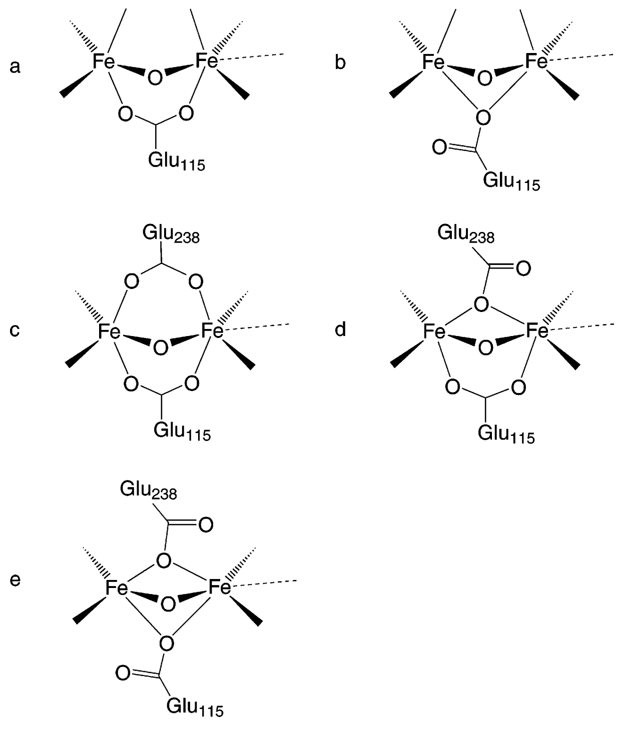

Figure 35. Possible core structures for RNR intermediate X.

In contrast to the wealth of experimental studies, few theoretical studies have focused on the structure and spin states of the RNR active site.[213i,220b,231] One model of intermediate X has been examined in detail by Siegbahn, which contains (Figure 36, also see Figure 6 in ref 220b) one μ-oxo bridge, one hydroxo bridge, and two bidentate carboxylates from Glu115

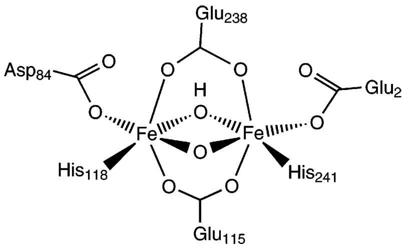

Figure 36. Active site model for RNR intermediate X proposed by Siegbahn.[220b]

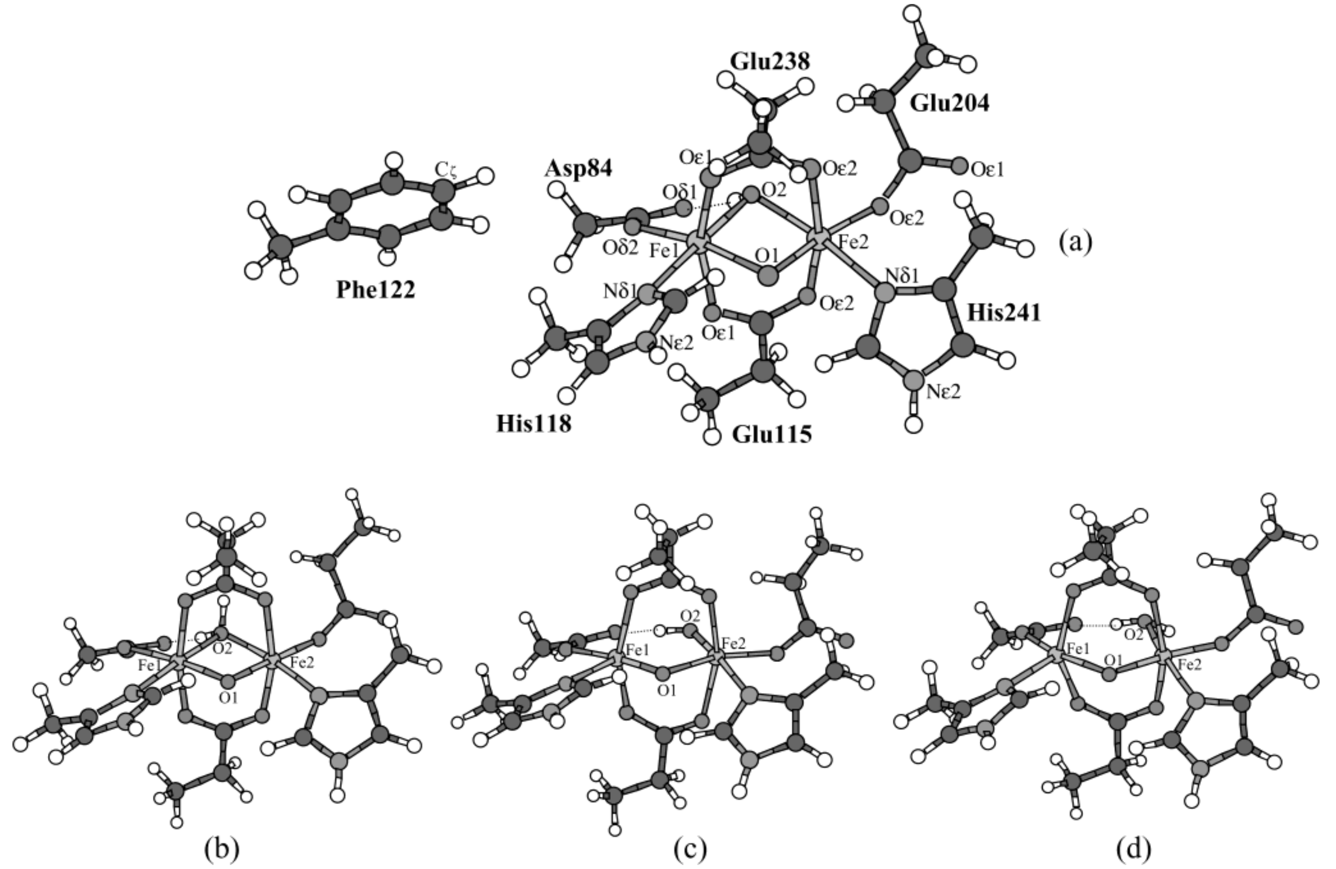

Figure 37. Our small quantum cluster models for RNR−X adapted from Siegbahn's model (Figure 36), (a) with a bridging hydroxide; (b) with a bridging H_2O; (c) with a terminal hydroxide; and (d) with a terminal H_2O. Because the majority of the experiments have been performed on a R2 mutant Y122F (Tyr122 → Phe122), we also included the Phe122 side chain into the model clusters (not shown in b−d).[232]

and Glu238. Following geometry optimization of this $S_{\text{total}} = {}^1/_2$ model using the B3LYP density functional theory (DFT) approach, an Fe−Fe distance of 2.61 Å was obtained. Furthermore, spin populations of 0.99 and −1.71 were noted for the two iron sites. Such small spin populations are more characteristic of low-spin and intermediate-spin Fe centers, rather than high-spin Fe sites, and appear inconsistent with the Mössbauer data for X.

Very recently, we have reexamined Siegbahn's model in an attempt to find out whether the protonated oxygen is present as a bridging hydroxide (Figure 37a), a bridging water (Figure 37b), a terminal hydroxide (Figure 37c), or a terminal water (Figure 37d); which Fe site is Fe(III) or Fe(IV) in such a model; if the active site adopts a high-spin AF-coupled $S_{\text{tot}} = {}^1/_2$ ground state; if we can reproduce the very short Fe−Fe distance of 2.5 Å found by EXAFS; and if the calculated Mössbauer parameters are consistent with experiment.[232]

We first worked on the small models (Figure 37a−d). For the high-spin AF-coupled $S = {}^1/_2$ state, the energetic and pK_a analysis showed that the model with a bridging hydroxide was the most favorable one. Additional calculations on the smaller model with a bridging hydroxide in different spin-coupled states showed that the F-coupled $S = {}^3/_2$ state has the lowest energy. Although the Fe−Fe distance (2.559 Å) of this state is very close to the 2.5 Å suggested by EXAFS,[230c] the $S = {}^3/_2$ spin state does not agree with the known $S = {}^1/_2$ ground state for X. We then enlarged the model for X by including the important second-shell and outer-shell H-bonding partners (see Figure 38). This allows us to examine whether the irons are present as high-spin or intermediate-spin states in a much larger quantum mechanical description of the protein environment, and whether the ground state of the cluster has total spin $S = {}^1/_2$.

Our results show that the AF-coupled $S = {}^1/_2$ intermediate state ($S_1 = {}^3/_2$, $S_2 = 1$, r(Fe−Fe) = 2.708 Å) is now the lowest in energy (S_1 is the Fe site closer to Phe or Tyr, S_2 is the farther Fe site). Next is the high-spin AF-coupled $S = {}^1/_2$ ($S_1 = 2$, $S_2 = {}^5/_2$, r(Fe−Fe) = 2.762 Å) state, which is by 1.51 kcal/mol higher in energy. The third one is a F-coupled $S = {}^3/_2$ (r(Fe−Fe) = 2.561 Å) state, which is higher than the lowest-energy state by 1.97 kcal/mol.[232]

Mössbauer property calculations were then performed on the three lowest energy states. It turned out that the calculated isomer shifts for Fe(IV) and Fe(III) sites in these three clusters are quite similar and the calculated quadrupole splitting values for Fe(III) site are smaller than those for the Fe(IV) site, which are inconsistent with the experimental data. On the basis of these calculations, we conclude that this model with one μ-oxo bridge, one hydroxo bridge, and two bidentate carboxylates from Glu115 and Glu238 is unlikely to be representative of the core structure of X.[232]

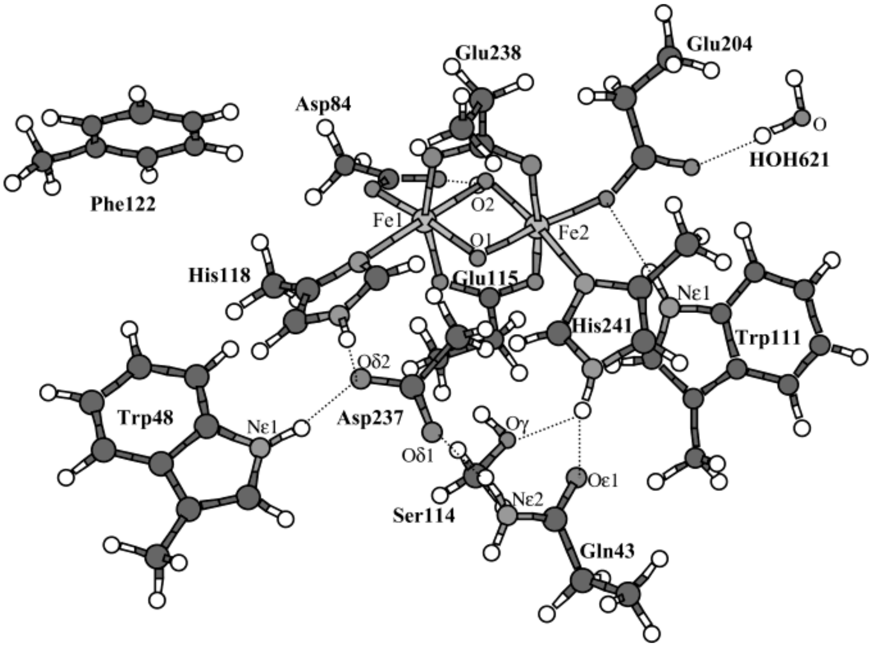

Figure 38. Our large RNR-X model (relative to the small one in Figure 37a) with a bridging hydroxide.[232]

More recently, Siegbahn has also examined the mechanism of formation of intermediate X via O−O bond cleavage leading to subsequent formation of the tyrosyl radical.[233] The new suggested structure for intermediate X (see Figure 39) was very similar to that proposed for intermediate Q of MMOH by Friesner and Lippard, the only difference being the addition of an extra electron and a proton to a bridging oxo group, as well as substitution of a glutamate with an aspartate ligand. The suggested mechanism involves an extra water molecule that enters the cycle between Tyr122 and the iron-bound water ligand, which helps considerably in the energetics of the transfer of a proton to the correct side of the diiron cluster.

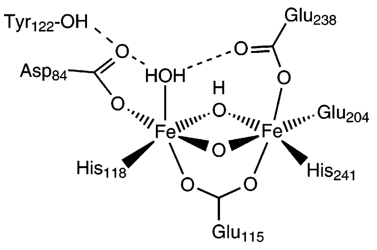

Figure 39. Siegbahn's second RNR-X model.[233]

We have currently examined a model[234] (see Figure 40) containing the core structural features proposed by Burdi et al.[230e] consisting of a μ-oxo bridge, a terminal protonated oxygen ligand bound to the iron nearest Tyr122, and a mono-oxygen bridge from Glu238 (not Glu115 as the position of this carboxylate remains bidentate in both the oxidized and the reduced forms) in the core structure of X. In accord with Mössbauer and Q-band ENDOR spectroscopy, we have geometry optimized the $S_{\mathrm{tot}} = {}^{1}/_{2}$ model containing AF-coupled high-spin iron(III) and iron(IV) sites. For both cases of water and hydroxide bound terminally to iron, the $S_{\mathrm{Fe1}} = 2$, $S_{\mathrm{Fe2}} = {}^{5}/_{2}$ state is lower in energy than the valence interchanged alternative with site Fe1 predicted to be the ferryl center.

The oxygen O of the carboxylate of Glu238 coordinates to Fe2(ferric) in the lower-energy terminal hydroxide model, and to Fe2(ferryl) in the higher-energy hydroxide model. For the water-bound form, O(Glu238) binds to the ferryl site in both cases, that is, Fe1 in the $S(\mathrm{Fe1}) = 2$, $S(\mathrm{Fe2}) = {}^{5}/_{2}$ state and Fe2 in the $S(\mathrm{Fe1}) = {}^{5}/_{2}$, $S(\mathrm{Fe2}) = 2$ state. Relative energy and pK_a analyses indicate the $S(\mathrm{Fe1}) = 2$, $S(\mathrm{Fe2}) = {}^{5}/_{2}$ state of the terminal hydroxide model cluster is the most stable one among the four clusters studied for this second larger model, and its calculated isomer shift and quadrupole splitting parameters also agree best with the experimental values. However, the DFT-calculated ^{1}H proton and ^{17}O hyperfine tensors for this state do not show good agreement with the experiments. The iron−iron separation for this and the other three clusters are all larger than 2.9 Å, a feature inconsistent with the EXAFS distance of 2.5 Å.[234]

Additional experimental and theoretical studies are still needed to clarify if the iron−iron separation in intermediate X is really near 2.5 Å, and whether a second bridging oxo or OH^- (in Siegbahn's second model)[233] should appear. The experimental interpretation of the experiments is that the high-spin AF-coupled state must dominate and it is clear that the core structure for X is influenced by the individual spin states of the Fe sites. The relative energies of the different spin states for the models discussed above are modulated by the environment (e.g., the H-bonding interactions and steric effects[235,236]). It seems that, wherever possible, the inclusion of second- and outer-shell residues into the quantum cluster model is a prerequisite to describe the spin state of the cluster correctly. Our current calculations *do not* predict both the observed short Fe−Fe distance (2.5 Å) *and* the AF-coupled $S = {}^{1}/_{2}$ ground state

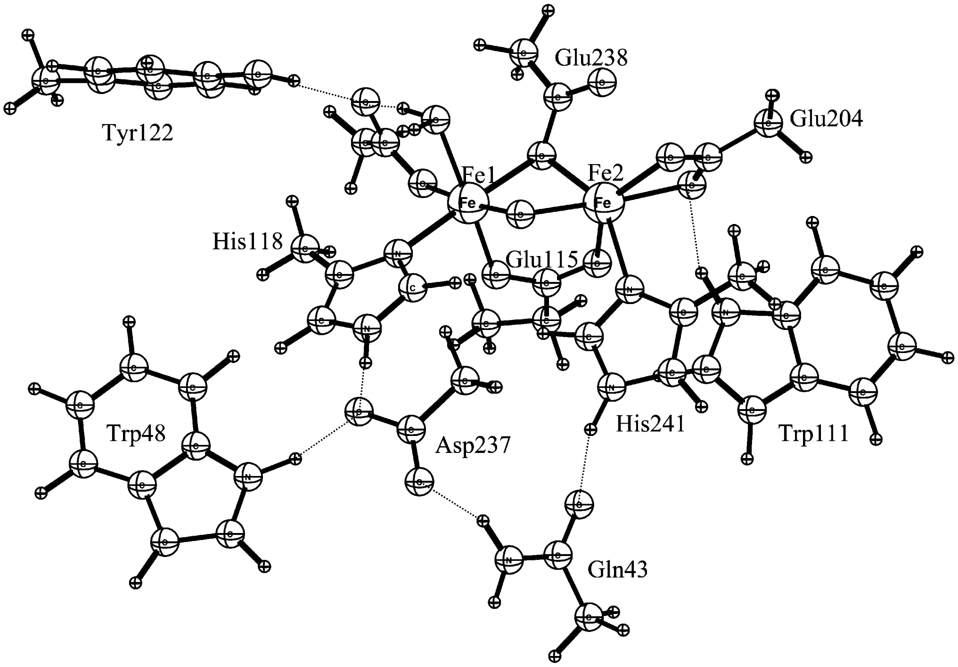

Figure 40. Our second large RNR-X model[234] based on the observations of Burdi et al.[230e]

from high-spin Fe sites in the lowest energy structure(s).

On the basis of Mössbauer and Q-band ENDOR spectroscopy combined with theoretical calculations of the geometries, energies, pK_as, and spectroscopic properties for the proposed cluster models and by considering all of these factors, the models studied here are still unlikely to be representative of the core structures of RNR intermediate X.[232,234] Of particular concern is the short Fe–Fe distance reported in the EXAFS experiments which is not reflected in the calculations where the Fe sites are high-spin. It is well-known that there are two crystallized synthetic diiron systems which produce short Fe–Fe distances. One is the $[Fe(III)Fe(IV)(\mu\text{-}O)_2(5\text{-}Et_3\text{-}TPA)_2](ClO_4)_3$ cluster (with $S_1 = {}^1/_2$, $S_2 = 1$, and $S_{total} = {}^3/_2$), which contains an $Fe_2(\mu\text{-}O)_2$ core, that results in an Fe–Fe distance of 2.683 Å.[237,238] Our first Fe(III)–O–Fe(IV) model, which contains two bidentate bridging carboxylates from Glu115 and Glu238, and a bridging hydroxide, also yields a short Fe1–Fe2 distance of 2.561 Å for the mixed-valent $S_{total} = {}^3/_2$ state. The corresponding high-spin AF-coupled $\{S_1 = {}^5/_2, S_2 = -2\}$ and $\{S_1 = -2, S_2 = {}^5/_2\}$ states, however, yield longer Fe–Fe distances of 2.804 and 2.762 Å, respectively. These are shorter than the Fe1–Fe2 distances for the current model, but still much longer than the 2.5 Å predicted by the EXAFS measurements. Another crystallized synthetic system is the $[Fe(II)Fe(III)(OH)_3(tmtacn)_2]^{2+}$ cluster, which contains three (OH^-) bridges with the ($S_1 = 2$, $S_2 = {}^5/_2$, and $S_{total} = {}^9/_2$) state, and produces a short Fe–Fe distance of 2.51 Å.[237,238] Comparing these two synthetic systems, it is difficult to see how current models with an Fe(III)–O–Fe(IV) core and one bidentate carboxylate bridge will produce the 2.5 Å Fe–Fe distance in the ($S_a = 2$, $S_b = {}^5/_2$, and $S_{total} = {}^1/_2$) state. Also, additional bridging H_2O, OH, or oxo ligands appear to give calculated ENDOR and/or Mössbauer parameters incompatible with experiment. Further experimental and theoretical studies, therefore, are still needed to provide more structural information about X.

11. Lipoxygenase

Lipoxygenases (LOs) are a class of non-heme iron enzymes that catalyze the stereo- and regioselective oxygenation of polyunsaturated fatty acids with a *cis*,*cis*-1,4-pentadiene substructure such as linoleic and arachidonic acids.[239] LOs are widely distributed in plants and animals, involved in the biosynthesis of growth-regulation and wound-healing substances for plants and leukotrienes and lipoxins, which are cell effector molecules of mammalian organisms.[240] In plants, soybeans have three LO isoforms, sLO-1, sLO-2, and sLO-3, while in mammals, LOs are classified into 5-, 8-, 12-, and 15-LO's according to their positional specificity of substrate oxygenation. X-ray structures for sLO-1,[241] sLO-3,[242] and rabbit 15-LO (15-rLO)[243] have been reported. The active site for the resting form of sLO-1 consists of a ferrous ion coordinated by three imidazole rings of histidine residues (His499, His504, His 690, based on 1YGE), a carboxylate oxygen of C-terminal isoleucine (Ile839), and a water molecule. An asparagine (Asn694) is loosely bound to the Fe(II) center with an Fe–O distance of about 3 Å. Therefore, the Fe(II) center may be considered as five coordinate. This ligand is flexible. Magnetic circular dichroism (MCD) studies in the solution phase further revealed that a significant portion of the six-coordinate Fe(II) center, in which Asn694 fully binds to iron ion, is mixed with the five-coordinate form.[244] Addition of substrate results in a full six-coordinate active site. In contrast, EPR and EXAFS data show that ferric sLO-1 remains a five-coordinate Fe(III) center, even in the presence of a substrate.[245] This fluctuation of coordination number around the iron center in sLO-1 is referred to as “coordination flexibility” and has a vital

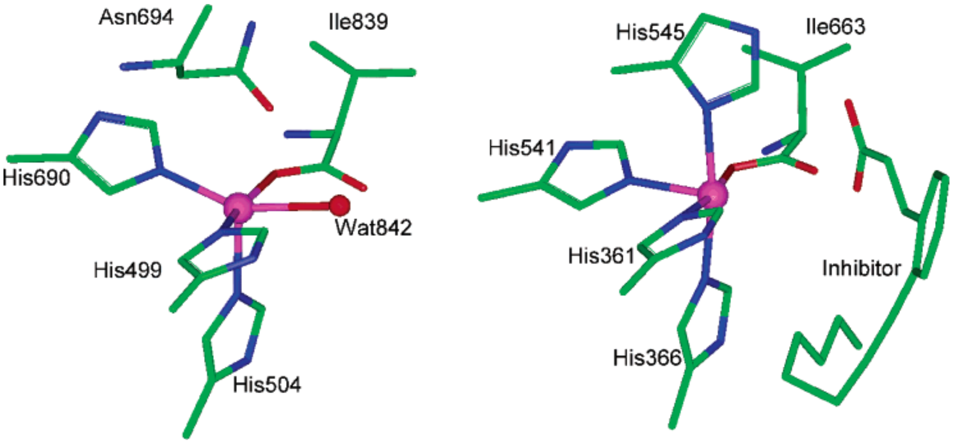

Figure 41. Active site models of sLO-1 (left) and 15-rLO (right) based on X-ray crystal structures. PDB codes: 1YGE for sLO-1 and 1LOX for 15-rLO.

importance in the regulation of enzyme activity.[48] For mammalian 15-LO, a histidine ligand replaces the asparagine to complete the six-coordinate environment.

Coordination flexibility in ferrous sLO-1 is the focus of two recent density functional calculations.[246,247] In one study, B3LYP calculations were undertaken for active site models of ferrous and ferric forms in sLO-1 and 15-rLO protein structures. Figure 41 depicts the active site models of these two proteins used in the calculations, in which the first coordination shells were represented by the reasonably simplified parts. Starting from the crystal structure geometries, the models were fully optimized. The calculated Fe−ligand bond lengths agree fairly well with experimental data obtained from the X-ray structure and EXAFS, except for ferrous forms of sLO-1. Without any constraint, the Asn694 ligand in the ferrous sLO-1 model moved toward to the iron center during the geometry optimization and ended up a typical six-coordinate complex. A constrained geometry optimization was done with the Fe−O-(Asn694) distance fixed at 3.05 Å. This optimization led to an effective five-coordinate structure. A series of potential energy scans for selected Fe−ligand bonds indicated that asparagine and water tend to make relatively weak bonds in the ferrous form of sLO-1. The calculated energy costs for stretching a ligand from its equilibrium distance to 3.05 Å are only 4.02 kcal/mol for Asn in the ferrous form and 7.40 kcal/mol for His. This energy penalty can be compensated by forming a typical hydrogen bond (3−5 kcal/mol) for Asn694 in the extended hydrogen-bonding network of the protein, but the penalty is higher for the His ligand.[246] A recent study on the sLO-1 mutants demonstrated that the hydrogen bond between Asn694 and the second coordination sphere residue Gln697 plays a key role in regulation of the enzyme activity by modulating the coordination flexibility of Asn694.[248]

The reason for the weak interaction between the Fe(II) center and Asn694 was further revealed by another B3LYP study, that used a simplified active site model in which all histidines were represented by ammonia groups.[247] This calculation demonstrated that the sideway rotated orientation of the Asn694 O−C−N plane plays a key role in controlling the Fe(II)−O(Asn694) length. Optimization of all Fe−ligand distances with the Fe−O−C−N dihedral angle fixed at −112° gave an Fe(II)−O(Asn694) distance of 2.91 Å, comparable to the 3.04 Å distance found in the crystal structure. Release of this dihedral angle constraint contracted the bond length to 2.43 Å. A further shortening to 2.34 Å was achieved after optimization of the (Asn694)O−Fe(II)−N(His690) angle. It was concluded that the protein controls the Fe(II)−O(Asn694) bond length by adjusting the spatial orientation of the Asn694 side chain and results in a weak coordination bond. A similar geometry optimization for the ferric form with an Fe(III)−O−C−N (Asn694) dihedral angle constraint led to a five-coordinate site, in which the Fe(III)−O(Asn694) bond was even weaker than the Fe(II)−O(Asn694) bond based on the calculated bond lengths and bond energies. This is an unusual example in which a ligand binds more weakly to the Fe(III) center than to Fe(II) in a protein environment. The cause can be attributed to the existence of a strong hydroxide donor in the position cis to Asn694 that weakens the Fe(III)−O(Asn694) bond by strongly interacting with the same Fe d-orbitals involved in overlap with the donor function of Asn694.

Time-dependent density functional theory (TDDFT) was used to calculate spectral properties of ferrous and ferric sLO-1 and 15-rLO active site models.[246] The calculation confirmed that the splitting between two observed MCD bands (Δ^5E_g) in the ferrous form originated from axial ligand bonding. Δ^5E_g is large for the five-coordinate ferrous sLO-1 form due to the large axial distortion and is small for six-coordinate sLO-1 and 15-rLO forms. The experimental splitting Δ^5E_g values can be reproduced very well by the TDDFT calculations when the vacuum optimized geometries were used, while the calculated two absolute vertical d−d excitation energies were close to experimental values only when experimental geometry parameters were adopted. The UV−vis CD observed relative shift of the band positions between sLO-1 and the mutant was satisfactorily reproduced. Spin density analysis and the orbital character of the first transition in the ferric sLO-1 form showed much more covalent character for the Fe(III)−OH bond than for other Fe−ligand bonds.

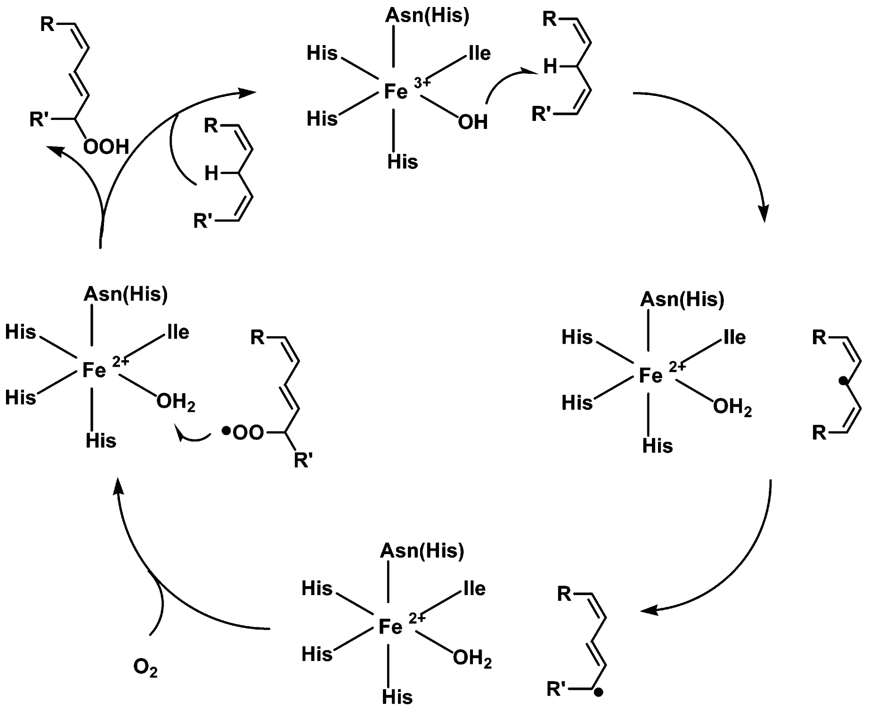

Figure 42. Reaction mechanism for lipoxygenase.

Three possible catalytic mechanisms have been proposed for the hydroperoxidation reaction, among which the radical mechanism is the most widely accepted.[249] In this mechanism, the first step is the abstraction of a H-atom from the substrate by Fe(III)–OH, resulting in a substrate radical and Fe(II)–OH_2. The second step involves a reaction of the substrate radical with O_2 to produce a peroxyl radical. In the last step, the substrate peroxyl radical captures a proton from Fe(II)–OH_2 and meanwhile is reduced to hydroperoxide product, accompanying the regeneration of the active ferric form of Fe(III)–OH. This catalytic cycle is shown in Figure 42. Alternatively, organo-iron and ene-radical mechanisms have been proposed. The distinct feature of the organo-iron mechanism is the formation of an organo-iron intermediate through the attack of the substrate carbanion by the ferric center after the proton transfers from the substrate to a basic group close to the iron center as proton acceptor.[250] The ene-radical is a variant of the radical mechanism in which the hydrogen abstraction results in a vinyl-allyl radical. An epoxy-like complex is formed through an attack on the vinyl portion of this substrate radical by the ferrous activated O_2.[251]

The thermodynamics and kinetics of H-atom abstraction, which is the first step in the radical mechanism of the catalytic reaction, were carefully investigated by density functional calculations.[247,252] The coordination flexibility mediated by Asn694 in the sLO-1 protein has a profound effect on the reaction energetics of the substrate oxidation. The substrate-bound ferrous form of sLO-1 is six-coordinate and stabilized, while the corresponding ferric form is only five-coordinate and destabilized, which results in an increase in the redox potential of the Fe(III) center. Using (*Z*,*Z*)-2,5-heptadiene as a model substrate for sLO-1, the B3LYP calculation with LANL2DZ and D95 double-ζ basis sets gave a total reaction energy for H-atom abstraction of −18 kcal/mol, and an energy barrier of +30 kcal/mol along the H-atom transfer reaction coordinate when the experimental substrate–iron center distance was used. The barrier height can be lowered to about +15 kcal/mol if substrate is moved closer to the Fe center and the zero-point energy correction is included in the calculation. This energy barrier can be overcome by proton tunneling. During the H-atom abstraction process, the proton tunneling is accompanied by the reduction of Fe(III) to Fe(II) with an electron transferred from substrate to protein, a typical proton-coupled electron transfer (PCET) mechanism. Electronic structure analysis along the H-atom transfer reaction coordinate showed that the electron is transferred directly to the Fe(III) center from substrate, rather than localizing on the proton; therefore, the reaction is a concerted proton tunneling–electron tunneling (PTET) process through the covalently linked Fe–O–H–C bridge superexchange pathway in the transition state. The +15 kcal/mol barrier height corresponds to a thermal reaction rate k_{therm} of about 1 s^{-1}. The upper limit for the tunneling rate in lipoxygenase can be as high as 2×10^9 s^{-1}.[247]

In a recent density functional study, the full catalytic cycle for peroxidation of polyunsaturated fatty acids by sLO-1 was investigated using the B3LYP method.[252] A simplified active site model was adopted in which the histidine side-chain ligands were replaced by ammonia molecules and a 2,5-heptadiene was used as substrate. The geometries of reaction intermediates and transition states of all steps were optimized, and all transition states were confirmed by frequency calculations. The first catalytic step, the H-atom abstraction from heptadiene to the Fe(III)–OH site, was calculated to be exoergic by 12.6 kcal/mol. An early, non-“tight” transition state was found with an activation energy of 12.1

kcal/mol. Spin density analysis along the reaction coordinate demonstrated that the H-atom transfer process can be seen as an electron transfer from the substrate to the ferric center accompanied by the proton shift between C in the substrate to O in the Fe(III)−OH moiety over a relatively short distance. This conclusion is corroborated with another DFT study and is in accord with the nonadiabatic model for proton tunneling based on the Marcus electron-transfer theory combined with Franck−Condon factors for H-atom tunneling. For the second step, the DFT calculation obtained a reaction energy of −7.8 kcal/mol for the reaction between the diene radical and the triplet molecular oxygen through a low-lying transition state with an activation energy of 2.0 kcal/mol. The calculation also examined the possibilities of forming an organo-iron intermediate and for oxygen to bind to ferrous site directly, and it was found that such intermediate complexes are energetically unfavorable. Accordingly, the organo-iron mechanism and ene-radical mechanism can be ruled out on the basis of the calculated energetics. The reduction of peroxy radical by the ferrous active site in the last step can proceed through two possible pathways. The calculation showed that the direct H-atom transfer from the Fe(II)−OH_2 site to the peroxy radical is almost isoenergetic (0.3 kcal/mol) with no barrier for the reaction. Alternatively, the peroxy radical may bind to the ferrous active site and form a seven-coordinate purple form of sLO-1. The calculated formation energy of the seven coordinate purple form is −6.0 kcal/mol. The decomposition of the purple form to the hydroperoxy product and a ferric site closes the catalytic reaction, and the reaction was calculated to be endoergic (6.2 kcal/mol) with an activation energy of 10.1 kcal/mol. These results suggested that the direct reduction of peroxy radical is kinetically favorable and the formation of the purple form is thermodynamically advantageous. The whole peroxidation process is exoergic with a calculated total reaction energy of −20.1 kcal/mol.[252]

12. Summary and Outlook

In this work, we have provided a guided tour of high level quantum chemical studies of reaction mechanisms, and an assessment of related problems of intermediates and transition states for a wide variety of metalloenzymes.

Some valuable parallels can be drawn between the mechanisms of protein tyrosine phosphatases (PTPases) (a nonmetal enzyme) and ribozyme chemistry. For example, PTPases exhibit a phosphate-transfer reaction characterized by a dissociative transition state (metaphosphate, PO_3^-) (Mechanism A) with a single early proton transfer and a low barrier. PTPases are extremely efficient enzymes, but this requires first of all that the protein structure stabilize unusual protonation states for Asp (protonated, neutral) and Cys (anion). The active site is highly charged and polar, and with charged and dipolar groups surrounding the main active site residues and substrate. In the Mg^{2+} aquo-catalyzed hammerhead ribozyme phosphate hydrolysis reaction, there is an associative transition state to a pentacoordinate (PO_5) intermediate, also with an early proton transfer, the first of two proton transfers overall. These mechanisms look quite different, and yet there are some common themes. The Mg^{2+} coordinates to the *pro-R* oxygen of phosphate, which reduces its charge. Further, this *pro-R* oxygen is cis to the P−O bond being broken. This is rather similar to the higher-energy Mechanism B in the PTPase calculations, where a proton residing on the non-bridging O (reducing the charge on the phosphate) converts a dissociative transition state (Mechanism A) into an associative one. Meanwhile, the ability of charged Mg^{2+} to acidify H_2O to form OH^- proves critical for both proton transfers, where only the second occurs to the leaving group.

In “click” chemistry, the catalysts for the reaction of triply bonded reactants (here, azides and nitriles) are fairly simple, Zn^{2+} or other Lewis acids or Bronsted acids in solution. The function of the catalyst is to increase the polarity of one of the reactants (the nitrile in this case), and to coordinate it, which then allows the bonding and ring formation between the reactants to occur. This same theme applies to other “click” chemistry reactions. Click chemistry has been seen for other transition metals. In particular, Cu(I) shows great versatility in ligating organic azides and alkynes to form five-membered heterocycles (triazoles) with a very wide variety of organic substituents.[253] A novel mechanism has been proposed on the basis of the initial DFT calculations involving an unusual six-membered Cu-containing ring as an intermediate. Click reactions have also been generated within an intact enzyme active site cavity,[254] evidently catalyzed by the specific cavity shape, and perhaps by electrostatic interactions. So far, these intact enzyme reactions are not metal catalyzed, but this field is promising both for general synthesis and for modifying enzymatic reactions.

There are two connections with bioinorganic systems. First, breaking multiple bonds is outside the realm of all but a few specialized enzymes, such as nitrogenase and nitrile hydratase. Second, those enzymes that do break multiple bonds, such as nitrogenase, have the same problem to solve: how to coordinate and polarize a strongly bonded and rather unreactive molecule, like N_2. For nitrogenase, we have seen that the site for N_2 binding is still not resolved; synthetic catalytic chemistry suggests that a single Mo catalytic site may be sufficient, while the use of alternative substrates and mutagenesis favors a 4Fe4S face of the $MoFe_7S_9X$ prismane cluster as the likely binding site.

For the resting state of nitrogenase, which is the starting point for analyzing reduction, protonation, and N_2 binding, and reduction to NH_3 at the active site, an “impasse” has been broken by very-high-resolution X-ray crystallography and comparison of experimental redox potentials and Mössbauer properties with DFT/electrostatics calculations. The newly identified central ligand of the $MoFe_7S_9X$ prismane cluster is very probably nitrogen (N^{3-}), and consistently the resting cluster oxidation state is $Mo^{4+}Fe_4^{2+}$-$Fe_3^{3+}S_9X$. Further, considerable experience has been obtained in treating coupled electron and proton transfers in the Rieske iron−sulfur protein, and in other metalloenzymes as well by a combination of DFT and electrostatics-based methods.

For Mn and FeSOD, the coupling between electron transfer and proton transfer is seen both kinetically and through DFT/electrostatics calculations of active site intermediates. The appearance of an inactive form of MnSOD at high $O_2^{\bullet-}$ concentrations, probably having a side-on-bound peroxo, is likely due to protonation and loss of either a water or an aspartate ligand. Excessive mobility at the active site is counterproductive in this case. Bonding and electrostatic analysis further show which first, second, and even third-shell ligands are most important. These calculations can be productively compared to the analysis of mutant (and metal substituted) enzyme structures and to synthetic analogues. Related calculations and analysis have been conducted for CuZnSOD. The bridged Cu−His−Zn site exhibits better control of superoxide catalysis and of active site conformation via Cu−His bond breaking and protonation as compared to MnSOD where the active site has no such linkage. MnSOD and FeSOD clearly show “proton gated electron transfer”. Related mechanisms are widespread in metalloenzymes. There is considerable room for further work on reaction pathways (particularly on transition states) and mutagenesis using larger and more accurate active site models and a better representation of the extended environment.

On methane monooxygenase (MMOH) and ribonucleotide reductase (RNR), the reaction mechanisms and intermediate states are partly understood. For MMOH, there have been a number of DFT studies of the reaction pathways leading to and from the important intermediate Q (the intermediate that oxidizes methane to methanol), and the predicted energy barriers look feasible, but there are still unresolved structural features for this intermediate, as well as for the earlier peroxo intermediate. Similarly, for RNR, DFT studies of reaction pathways to and from intermediate X (which oxidizes tyrosine to a neutral tyrosine radical) give reasonable reaction barriers, but again there are considerable structural and therefore also energetic uncertainties about X, as indicated by DFT structural and properties calculations as compared to available spectroscopic data.

For lipoxygenase, a reaction mechanism involving H-abstraction points to the importance of proton tunneling connected to electron transfer, and of metal−ligand covalency involving Fe^{3+}.

Two common themes for many of these enzymes are the importance of flexible and often charged amino acid side chains, and of extended charged H-bond networks from the active site to the protein surroundings. Water is often converted to hydroxyl or oxo (or conversely) and can enter or leave the active site. Amino acid side chains can readily change protonation states or become radicals in some cases.

What is mainly needed is a better integrated quantum plus classical methodology for treating large and complex transition metal active sites in an extended protein environment. The related methodology needs to be developed in several directions. There is an ongoing effort to improve DFT methods from a careful analysis of exchange, correlation, and electronic kinetic energy terms, using a selection of molecular families as test cases. This same strategy needs to be applied more extensively to spin-coupled transition metal complexes and adapted for compatibility with broken symmetry and spin projection methods. Close-lying electronic states and “state crossings” (or near crossings) require related improvements in methods. For very large systems, the interface between the quantum and classical subsystems has to be reliably modeled. Active site flexibility requires that the conformations of both quantum and classical subsystems can change in a coordinated way. The outline, at least, for these methods is now beginning to appear in the recent literature.

13. Acknowledgments

We thank our longtime collaborators Dr. David A. Case and Dr. Donald Bashford for their contributions to work discussed here. We also thank Drs. Valerie Dillet, Dilipkumar Asthagiri, Matthias Ullmann, Tiqing Liu, Cindy L. Fisher, Rhonda Torres, Jean-Marie Mouesca, Juan-Liang Chen, Chun-Yang Peng, William H. Richardson, Melanie Nelson, Xin-Gui Zhao, Hiroshi Kuramochi, David Adams, David Hendrickson, Edward Schmitt, Hui-Lien Tsai, Michael Thompson, Fred Salsbury, Charles Brooks III, James Fee, David Stout, Elizabeth Getzoff, K. Barry Sharpless, Zach Demko, and Robert Konecny for their contributions to our research. We have had valuable discussions with Drs. Lance Seefeldt, Brian Hoffmann, Eckard Munck, Edward Solomon, Martha Ludwig, Martin Bollinger, Anne-Frances Miller, David Silverman, John Tainer, and Elizabeth Stroupe. We thank Dr. Victoria Roberts for her critical reading of the manuscript and comments. We thank the NIH for financial support (grants GM43278 and GM39914, and for earlier support GM50154). F.H. thanks the Wenner-Gren Foundations for financial support.

14. References

(1) Fraústo da Silva, J. J. R.; Williams, R. J. P. *The Biological Chemistry of the Elements*; Clarendon Press: Oxford, 1991.
(2) Castagnetto, J. M.; Hennessy, S. W.; Roberts, V. A.; Getzoff, E. D.; Tainer, J. A.; Pique, M. E. *Nucleic Acids Res.* **2002**, *30*, 379.
(3) de Duve, C. *Blueprint for a Cell: The Nature and Origin of Life*; Neil Patterson: Burlington, NC, 1991.
(4) Chen, Q. W.; Bahnemann, D. W. *J. Am. Chem. Soc.* **2000**, *122*, 970.
(5) Maden, B. E. H. *Trends Biochem. Sci.* **1995**, *20*, 337.
(6) Blochl, E.; Keller, M.; Wachtershauser, G.; Stetter, K. O. *Proc. Natl. Acad. Sci. U.S.A.* **1992**, *89*, 8117.
(7) Beinert, H.; Holm, R. H.; Munck, E. *Science* **1997**, *277*, 653.
(8) Luchinat, C.; Sola, M. In *Encyclopedia of Inorganic Chemistry*; King, R. B., Ed.; Wiley: New York, 1994; pp 4406−4434.
(9) Mondragon, A.; Griffith, E. C.; Sun, L.; Xiong, F.; Armstrong, C.; Liu, J. O. *Biochemistry* **1997**, *36*, 4934.
(10) Miller, A. F.; Sorkin, D. L. *Comments Mol. Cell. Biophys.* **1997**, *9*, 1.
(11) Glusker, J. P. In *Encyclopedia of Inorganic Chemistry*; King, R. B., Ed.; John Wiley and Sons: New York, 1994; pp 598−609.
(12) Lippard, S. J.; Berg, J. M. *Principles of Bioinorganic Chemistry*; University Science Books: Mill Valley, CA. 1994.
(13) Beinert, H. *J. Biol. Inorg. Chem.* **2000**, *5*, 2.
(14) (a) Green, M. T. *J. Am. Chem. Soc.* **1999**, *121*, 7939. (b) Green, M. T. *J. Am. Chem. Soc.* **2001**, *123*, 9218.
(15) (a) Himo, F.; Noodleman, L.; Blomberg, M. R. A.; Siegbahn, P. E. M. *J. Phys. Chem. A* **2002**, *106*, 8757. (b) Himo, F.; Eriksson, L. A.; Blomberg, M. R. A.; Siegbahn, P. E. M. *Int. J. Quantum Chem.* **2000**, *76*, 714. (c) Ito, N.; Phillips, S. E. V.; Stevens, C.;

Ogel, Z. B.; McPherson, M. J.; Keen, J. N.; Yadav, K. D. S.; Knowles, P. F. *Nature* **1991**, *350*, 87. (d) Himo, F.; Siegbahn, P. E. M. *Chem. Rev.* **2003**, *103*, 2421. (e) Harris, D. L. *Curr. Opin. Chem. Biol.* **2001**, *5*, 724. (f) Ogliaro, F.; Cohen, S.; Filatov, M.; Harris, N.; Shaik, S. *Angew. Chem., Int. Ed.* **2000**, *39*, 3851.

(16) Noodleman, L.; Lovell, T.; Liu, T.; Himo, F.; Torres, R. A. *Curr. Opin. Chem. Biol.* **2002**, *6*, 259.

(17) Ludwig, M. L.; Ballou, D. P.; Noodleman, L. In *Handbook of Metalloproteins*; Wieghardt, K., Huber, R., Poulos, T., Messerschmidt, A., Eds.; John Wiley and Sons: Chichester, U.K., 2001; pp 652−667.

(18) Lovell, T.; Himo, F.; Han, W.-G.; Noodleman, L. *Coord. Chem. Rev.* **2003**, *238*−*239*, 211.

(19) Noodleman, L.; Lovell, T.; Han, W.-G.; Liu, T.; Torres, R. A.; Himo, F. In *Comprehensive Coordination Chemistry II, From Biology to Nanotechnology, Vol.2, Fundamentals*; Lever, A. B., Ed.; Elsevier: New York, 2003, pp 491−510.

(20) Becke, A. D. *J. Chem. Phys.* **1993**, *98*, 5648.

(21) Becke, A. D. In *The Challenge of d and f Electrons*, Salahub, D. R., Zerner, M. C., Eds.; American Chemical Society: Washington, DC, 1989; pp 165−179.

(22) Perdew, J. P. *Phys. Rev. B* **1986**, *33*, 8822.

(23) Becke, A. *J. Chem. Phys.* **1992**, *97*, 9173.

(24) Stoll, H.; Pavlidou, C. M. E.; Preuss, H. *Theor. Chim. Acta* **1978**, *149*, 143.

(25) Asthagiri, D.; Dillet, V.; Liu, T.; Noodleman, L.; Van Etten, R. L; Bashford, D. *J. Am. Chem. Soc.* **2002**, *124*, 10225.

(26) (a) Kohn, W.; Becke, A. D.; Parr, R. G. *J. Phys. Chem.* **1996**, *100*, 12974. (b) Koch, W.; Holthausen, M. C. *A Chemist's Guide to Density Functional Theory*; Wiley-VCH: Weinheim, Germany, 2001. (c) Springborg, M., Ed. *Density Functional Methods in Chemistry and Materials Science*; John Wiley and Sons: New York, 1997. (d) Baerends, E. J.; Gritsenko, O. V. *J. Phys. Chem. A* **1997**, *101*, 5383.

(27) (a) Li, J.; Noodleman, L.; Case, D. A. In *Inorganic Electronic Structure and Spectroscopy, Vol. 1, Methods*; Solomon, E. I., Lever, A. B. P., Eds.; John Wiley and Sons: New York, 1999; pp 661−724. (b) Li, J.; Noodleman, L. In *Spectroscopic Methods in Bioinorganic Chemistry*; Solomon, E. I., Hodgson, K. O., Eds.; ACS Symposium Series 692; American Chemical Society: Washington, DC, 1998; pp 179−195.

(28) (a) Siegbahn, P. E. M.; Blomberg, M. R. A. *Annu. Rev. Phys. Chem.* **1999**, *50*, 221.

(29) (a) Ghosh, P.; Bill, E.; Weyhermuller, T.; Neese, F. *J. Am. Chem. Soc.* **2003**, *125*, 1293. (b) Neese, F. *Curr. Opin. Chem. Biol.* **2003**, *7*, 125.

(30) Rosa, A.; Ehlers, A. W.; Baerends, E. J.; Snijders, J. G.; te Velde, G. *J. Phys. Chem.* **1996**, *100*, 5690.

(31) (a) Yang, X.; Wang, X.-B.; Fu, Y.-J.; Wang, L.-S. *J. Phys. Chem. A* **2003**, *107*, 1703. (b) Butcher, K. D.; Didziulis, S. V.; Briat, B.; Solomon, E. I. *J. Am. Chem. Soc.* **1990**, *112*, 2231.

(32) Pulay, P.; Fogarasi, G. *J. Chem. Phys.* **1992**, *96*, 2856.

(33) Jensen, F. In *Encyclopedia of Computational Chemistry*; Schleyer, P. v. R., Ed.; J. Wiley and Sons: Chichester, England, 1998; pp 3114−3123.

(34) Connors, K. A. *Chemical Kinetics: The Study of Reaction Rates in Solution*; VCH: New York, 1990.

(35) Wilmot, C. M.; Pearson, A. R. *Curr. Opin. Chem. Biol.* **2002**, *6*, 202.

(36) Crane, B. R.; Siegel, L. M.; Getzoff, E. D. *Biochemistry* **1997**, *36*, 6, 12120.

(37) Whittaker, J. W.; Whittaker, M. M. *J. Am. Chem. Soc.* **1991**, *113*, 5528.

(38) Dian, B. C.; Longarte, A.; Zwier, T. S. *Science* **2002**, *296*, 2369.

(39) (a) Garman, E. *Curr. Opin. Struct. Biol.* **2003**, *13*, 545. (b) Berglund, G. I.; Carlsson, G. H.; Smith, A. T.; Szoke, H.; Henriksen, A.; Hadju, J. *Nature* **2002**, *417*, 463.

(40) Lah, M. S.; Dixon, M. M.; Pattridge, K. A.; Stallings, W. C.; Fee, J. A.; Ludwig, M. L. *Biochemistry* **1995**, *34*, 1646.

(41) Li, J.; Fisher, C. L.; Konecny, R.; Bashford, D.; Noodleman, L. *Inorg. Chem.* **1999**, *38*, 929.

(42) Han, W.-G.; Lovell, T.; Noodleman, L. *Inorg. Chem.* **2002**, *41*, 205.

(43) Hunsicker-Wang, L. M.; Heine, A.; Chen, Y.; Luna, E. P.; Todaro, T.; Zhang, Y. M.; Williams, P. A.; McRee, D. E.; Hirst, J.; Stout, C. D.; Fee, J. A. *Biochemistry* **2003**, *42*, 7303.

(44) Berry, E. A.; Guergova-Kuras, M.; Huang, L.; Crofts, A. R. *Annu. Rev. Biochem.* **2000**, *69*, 1005.

(45) Elango, N.; Radhakrishnan, R.; Froland, W. A.; Wallar, B. J.; Earhart, C. A.; Lipscomb, J. D.; Olendorf, D. O. *Protein Sci.* **1997**, *6*, 556.

(46) Rosenzweig, A. C.; Nordlund, P.; Takahara, P. M.; Frederick, C. A.; Lippard, S. *J. Chem. Biol.* **1995**, *2*, 409.

(47) Lovell, T.; Li, J.; Noodleman, L. *Inorg. Chem.* **2001**, *40*, 5251.

(48) Solomon, E. I.; Brunold, T. C.; Davis, M. I.; Kemsley, J. N.; Lee, S.-K.; Lehnert, N.; Neese, F.; Skulan, A. J.; Yang, Y.-S.; Zhou, J. *Chem. Rev.* **2000**, *100*, 235.

(49) (a) Schlegel, H. B. In *Encyclopedia of Computational Chemistry*; Schleyer, P. v. R., Ed.; J. Wiley and Sons: Chichester, England, 1998; pp 1136−1142. (b) te Velde, G.; Bickelhaupt, F. M.; Baerends, E. J.; Guerra, C. F.; Gisbergen, S. J. A. van Snijders, J. G.; Ziegler, T. *J. Comput. Chem.* **2001**, *22*, 931.

(50) Scales, L. E. *Introduction to Non-Linear Optimization*; Springer-Verlag: New York, 1985.

(51) Leach, A. R. *Molecular Modeling: Principles and Applications*; Addison-Wesley Longman: Edinburgh Gate, Harlow, 1996.

(52) Chen, J. L.; Noodleman, L.; Case, D. A.; Bashford, D. *J. Phys. Chem.* **1994**, *98*, 11059.

(53) Bigeleisen, J.; Mayer, M. G. *J. Chem. Phys.* **1947**, *15*, 261.

(54) Dreuw, A.; Cederbaum, L. S. *Chem. Rev.* **2002**, *102*, 181.

(55) Wang, L.-S.; Wang, X.-B. *J. Phys. Chem. A* **2000**, *104*, 1978.

(56) Yang, X.; Wang, X.-B.; Niu, S.; Pickett, C. J.; Ichiye, T.; Wang, L.-S. *Phys. Rev. Lett.* **2002**, *89*, 163401.

(57) Torres, R. A.; Lovell, T. Noodleman, L.; Case, D. A. *J. Am. Chem. Soc.* **2003**, *125*, 1923.

(58) Wang, X.-B.; Wang, L.-S. *Nature* **1999**, *400*, 245.

(59) Stephanovich, E. V.; Boldyrev, A. I.; Truong, T. N.; Simons, J. *J. Phys. Chem. B* **1998**, *102*, 4205.

(60) (a) Noodleman, L.; Baerends, E. J. *J. Am. Chem. Soc.* **1984**, *106*, 2316. (b) Li, J.; Nelson, M. R.; Peng, C. Y.; Bashford, D.; Noodleman, L. *J. Phys. Chem. A* **1998**, *102*, 6311. (c) Mouesca, J.-M.; Chen, J. L.; Noodleman, L.; Bashford, D.; Case, D. A. *J. Am. Chem. Soc.* **1994**, *116*, 11898.

(61) Rosch, N.; Trickey, S. B. *J. Chem. Phys.* **1997**, *106*, 8940.

(62) Ullmann, G. M.; Noodleman, L.; Case, D. A. *J. Biol. Inorg. Chem.* **2002**, *7*, 632.

(63) Lovell, T.; Li, J.; Liu, T.; Case, D. A.; Noodleman, L. *J. Am. Chem. Soc.* **2001**, *123*, 12392.

(64) (a) Slater, J. C. *The Self-Consistent Field for Molecules and Solids: Quantum Theory of Molecules and Solids*; McGraw-Hill: New York, 1974. (b) Slater, J. C. *Adv. Quantum Chem.* **1972**, *6*, 1. (c) Wood, J. H. *Chem. Phys. Lett.* **1977**, *51*, 682. (d) Noodleman, L.; Post, D.; Baerends, E. *J. Chem. Phys.* **1982**, *64*, 159.

(65) Pantazis, D. A.; McGrady, J. E. *Inorg. Chem.* **2003**, *42*, ASAP.

(66) Adams, D. M.; Noodleman, L.; Hendrickson, D. N. *Inorg. Chem.* **1997**, *36*, 3966.

(67) Klamt, A.; Schüürmann, G. *J. Chem. Soc., Perkin Trans.* **1993**, *2*, 799.

(68) (a) Bashford, D.; Gerwert, K. *J. Mol. Biol.* **1992**, *224*, 473. (b) Dillet, V.; Dyson, H. J.; Bashford, D. *Biochemistry* **1998**, *37*, 10298. (c) Tomasi, J.; Persico, M. *Chem. Rev.* **1994**, *94*, 2027.

(69) (a) Chirlian, L. E.; Francl, M. M. *J. Comput. Chem.* **1987**, *8*, 894. (b) Breneman, C. M.; Wiberg, K. B. *J. Comput. Chem.* **1990**, *11*, 361.

(70) Li, J.; Fisher, C. L.; Chen, J. L.; Bashford, D.; Noodleman, L. *Inorg. Chem.* **1996**, *35*, 4694.

(71) Beroza, P.; Fredkin, D. R.; Okamura, M. Y.; Feher, G. *Proc. Natl. Acad. Sci. U.S.A.* **1991**, *88*, 5804.

(72) Warshel, A.; Levitt, M. *J. Mol. Biol.* **1976**, *103*, 227.

(73) Gao, J. In *Reviews in Computational Chemistry*; Lipkowitz, K. B., Boyd, D. B., Eds.; VCH: New York, 1995; Vol. 7.

(74) Field, M. J.; Bash, P. A.; Karplus, M. *J. Comput. Chem.* **1990**, *11*, 700.

(75) Han, W.-G.; Tajkhorshid, E.; Suhai, S. *J. Biol. Struct. Dyn.* **1999**, *16*, 1019.

(76) Monard, G.; Loos, M.; Thery, V.; Baka, K.; Rivail, J. L. *Int. J. Quantum Chem.* **1996**, *58*, 153.

(77) Gao, J.; Amara, P.; Alhambra, C.; Field, M. J. *J. Phys. Chem. A* **1998**, *102*, 4714.

(78) Gordon, M. S.; Freitag, M. A.; Bandyopadhyay, P.; Jensen, J. H.; Kairys, V.; Stevens, W. *J. Phys. Chem. A* **2001**, *105*, 293.

(79) Svensson, M.; Humbel, S.; Morokuma, K. *J. Chem. Phys.* **1996**, *105*, 3654.

(80) Vreven, T.; Morokuma, K.; Farkas, O.; Schlegel, H. B.; Frisch, M. J. *J. Comput. Chem.* **2003**, *24*, 760.

(81) Kaminski, G. A.; Stern, H. A.; Berne, B. J.; Friesner, R. A.; Cao, Y. X.; Murphy, R. B.; Zhou, R.; Halgren, T. A. *J. Comput. Chem.* **2002**, *23*, 1515.

(82) Kollman, P.; Massova, I.; Reyes, C.; Kuhn, B.; Huo, S.; Chong, L.; Lee, M.; Lee, T.; Duan, Y.; Wang, W.; Donini, O.; Cieplak, P.; Srinivasan, J.; Case, C. A.; Cheatham, T. E., III. *Acc. Chem. Res.* **2000**, *33*, 889.

(83) Han, W.-G.; Elstner, M.; Jalkanen, K. J.; Frauenheim, T.; Suhai, S. *Int. J. Quantum Chem.* **2000**, *78*, 459.

(84) Thompson, M. J.; Bashford, D.; Noodleman, L.; Getzoff, E. D. *J. Am. Chem. Soc.* **2003**, *125*, 8186.

(85) Gao, J.; York, D. *Theor. Chem. Acc.* **2003**, *109*, 99.

(86) Salsbury, F. R., Jr.; Han, W.-G.; Noodleman, L.; Brooks, C. L., III. *ChemPhysChem.* **2003**, *4*, 848.

(87) Car, R.; Parrinello, M. *Phys. Rev. Lett.* **1985**, *55*, 2471.

(88) Marx, D.; Hutter, J. In *Modern Methods and Algorithms of Quantum Chemistry*; Grotendorst, J., Ed.; John von Neumann Institute for Computing: Julich, 2000.

(89) (a) Carloni, P.; Rothlisberger, U.; Parrinello, M. *Acc. Chem. Res.* **2002**, *35*, 455. (b) Carloni, P. *Quant. Struct.−Act. Relat.* **2002**, *21*, 166. (c) Tse, J. S. *Annu. Rev. Phys. Chem.* **2002**, *53*, 249.

(90) Laio, A.; VandeVondele, J.; Rothlisberger, U. *J. Chem. Phys.* **2002**, *116*, 6941.

(91) Fischer, E. H.; Charbonneau, H.; Tonks, N. K. *Science* **1991**, *253*, 401.

(92) Hengge, A. C. *Acc. Chem. Res.* **2002**, *35*, 105.

(93) Jackson, M. D.; Denu, J. M. *Chem. Rev.* **2001**, *101*, 2313.

(94) Zhang, Z.-Y. *Acc. Chem. Res.* **2003**, *36*, 385.

(95) Kennelly, P. J. *Chem. Rev.* **2001**, *101*, 2291−2312.

(96) Dillet, V.; Van Etten, R. L.; Bashford, D. *J. Phys. Chem. B* **2000**, *104*, 11321.

(97) (a) Hansson, T.; Nordlund, P.; Aqvist, J. *J. Mol. Biol.* **1997**, *265*, 118. (b) Kolmodin, K.; Nordlund, P.; Aqvist, J. *Proteins: Struct., Funct.u, Genet.* **1999**, *36*, 370. (c) Kolmodin, K.; Aqvist, J. *Int. J. Quantum Chem.* **1999**, *73*, 147.

(98) Alhambra, C.; Wu, L.; Zhang, Z. Y.; Gao, J. *J. Am. Chem. Soc.* **1998**, *120*, 3858.

(99) Czyryca, P. G.; Hengge, A. C. *Biochim. Biophys. Acta* **2001**, *1547*, 245.

(100) Zhang, Z. Y.; Van Etten, R. L. *J. Biol. Chem.* **1991**, *266*, 1516.

(101) Fersht, A. *Enzyme Structure and Mechanism*; W. H. Freeman & Co.: New York, 1985.

(102) (a) Sharp, P. A. *Cell* **1985**, *42*, 397. (b) Strobel, S. A. In *Encyclopedia of Molecular Biology*; Creighton, T. E., Ed.; John Wiley and Sons: New York, 1999; Vol. 4. (c) Flores, R. In *Encyclopedia of Molecular Biology*; Creighton, T. E., Ed.; John Wiley and Sons: New York, 1999; Vol. 4. (d) Garcia-Arenal, F. In *Encyclopedia of Molecular Biology*; Creighton, T. E., Ed.; John Wiley and Sons: New York, 1999; Vol. 4.

(103) (a) Forster, A. C.; Symons, R. H. *Cell* **1987**, *50*, 9. (b) Forster, A. C.; Symons, R. H. *Cell* **1987**, *49*, 211.

(104) Blaskó, A.; Bruice, T. C. *Acc. Chem. Res.* **1999**, *32*, 475.

(105) (a) Kuimelis, R. G.; McLaughlin, L. W. *Nucleic Acids Res.* **1995**, *23*, 4753. (b) Kuimelis, R. G.; McLaughlin, L. W. *Biochemistry* **1996**, *35*, 5308. (c) Dahm, S. C.; Derrick, W. B.; Uhlenbeck, O. C. *Biochemistry* **1993**, *32*, 13040. (d) Dahm, S. C.; Uhlenbeck, O. C. *Biochemistry* **1991**, *30*, 9464.

(106) Westheimer, F. H. *Acc. Chem. Res.* **1968**, *1*, 70.

(107) (a) Slim, G.; Gait, M. J. *Nucleic Acids Res.* **1991**, *19*, 1183. (b) Koizumi, M.; Ohtsuka, E. *Biochemistry* **1991**, *30*, 5145. (c) van Tol, H.; Buzayan, J. M.; Feldstein, P. A.; Eckstein, F.; Bruening, G. *Nucleic Acids Res.* **1990**, *18*, 1971. (d) Usher, D. A. *Proc. Nat. Acad. Sci. U.S.A.* **1969**, *62*, 661. (e) Usher, D. A.; Erenrich, E. S.; Eckstein, F. *Proc. Natl. Acad. Sci. U.S.A.* **1972**, *69*, 115. (f) Usher, D. A.; Richardson, D. I.; Eckstein, F. *Nature* **1970**, *228*, 663.

(108) (a) Bruice, T. C.; Tsubouchi, A.; Dempcy, R. O.; Olson, L. P. *J. Am. Chem. Soc.* **1996**, *118*, 9867. (b) Vanhommerig, S. A. M.; Sluyterman, L. A. Æ.; Meijer, E. M. *Biochim. Biophys. Acta-Prot. Struct. Mol. Enzymol.* **1996**, *1295*, 125. (c) Dempcy, R. O.; Bruice, T. C. *J. Am. Chem. Soc.* **1994**, *116*, 4511.

(109) O'Rear, J. L.; Wang, S.; Feig, A. L.; Beigelman, L.; Uhlenbeck, O. C.; Herschlag, D. *RNA* **2001**, *7*, 537.

(110) Curtis, E. A.; Bartel, D. P. *RNA* **2001**, *7*, 546.

(111) (a) Cowan, J. A. *Chem. Rev.* **1998**, *98*, 1067. (b) Kuimelis, R. G.; McLaughlin, L. W. *Chem. Rev.* **1998**, *98*, 1027. (c) Zhou, D. M.; Taira, K. *Chem. Rev.* **1998**, *98*, 991.

(112) (a) Murray, J. B.; Dunham, C. M.; Scott, W. G. *J. Mol. Biol.* **2002**, *315*, 121. (b) Murray, J. B.; Terwey, D. P.; Maloney, L.; Kerpelsky, A.; Usman, N.; Beigelman, L.; Scott, W. G. *Cell* **1998**, *92*, 665. (c) Scott, W. G.; Finch, J. T.; Klug, A. *Cell* **1995**, *81*, 991. (d) Scott, W. G.; Murray, J. B.; Arnold, J. R. P.; Stoddard, B. L.; Klug, A. *Science* **1996**, *274*, 2065.

(113) (a) Storer, J. W.; Uchimaru, T.; Tanabe, K.; Uebayasi, M.; Nishikawa, S.; Taira, K. *J. Am. Chem. Soc.* **1991**, *113*, 5216. (b) Uebayasi, M.; Uchimaru, T.; Koguma, T.; Sawata, S.; Shimayama, T.; Taira, K. *J. Org. Chem.* **1994**, *59*, 7414. (c) Uchimaru, T.; Tanabe, K.; Nishikawa, S.; Taira, K. *J. Am. Chem. Soc.* **1991**, *113*, 4351. (d) Lim, C.; Karplus, M. *J. Am. Chem. Soc.* **1990**, *112*, 5872.

(114) Boero, M.; Terakura, K.; Tateno, M. *J. Am. Chem. Soc.* **2002**, *124*, 8949.

(115) Torres, R. A.; Himo, F.; Bruice, T. C.; Noodleman, L.; Lovell, T. *J. Am. Chem. Soc.* **2003**, *125*, 9861.

(116) Lyne, P. D.; Karplus, M. *J. Am. Chem. Soc.* **2000**, *122*, 166.

(117) Haake, P. C.; Westheimer, F. H. *J. Am. Chem. Soc.* **1961**, *83*, 1102.

(118) Lahiri, S. D.; Zhang, G.; Dunaway, D.; Allen, K. N. *Science* **2003**, *299*, 2067.

(119) Uhlenbeck, O. C. *Nature* **1987**, *328*, 596.

(120) Fedor, M. J.; Uhlenbeck, O. C. *Biochemistry* **1992**, *31*, 12042.

(121) Dejaegere, A.; Lim, C.; Karplus, M. *J. Am. Chem. Soc.* **1991**, *113*, 4353.

(122) Taira, K.; Uchimaru, T.; Storer, J. W.; Yliniemela, A.; Uebayasi, M.; Tanabe, K. *J. Org. Chem.* **1993**, *58*, 3009.

(123) Torres, R. A.; Bruice, T. C. *Proc. Natl. Acad. Sci. U.S.A.* **1998**, *95*, 11077.

(124) Torres, R. A.; Bruice, T. C. *J. Am. Chem. Soc.* **2000**, *122*, 781.

(125) Singh, H.; Chawla, A. S.; Kapoor, V. K.; Paul, D.; Malhotra, R. K. *Prog. Med. Chem.* **1980**, *17*, 151.

(126) (a) Ostrovskii, V. A.; Pevzner, M. S.; Kofmna, T. P.; Shcherbinin, M. B.; Tselinskii, I. V. *Targets Heterocycl. Syst.* **1999**, *3*, 467. (b) Hiskey, M.; Chavez, D. E.; Naud, D. L.; Son, S. F.; Berghout, H. L.; Bome, C. A. *Proc. Int. Pyrotech. Semin.* **2000**, *27*, 3.

(127) Koldobskii, G. I.; Ostrovskii, V. A. *Usp. Khim.* **1994**, *63*, 847.

(128) (a) Huisgen, R.; Sauer, J.; Sturm, H. J.; Markgraf, J. H. *Chem. Ber.* **1960**, *93*, 2106. (b) Moderhack, D. *J. Prakt. Chem.* **1988**, *340*, 687.

(129) (a) Quast, H.; Bieber, L. *Tetrahedron Lett.* **1976**, *18*, 1485. (b) Krayushin, M. M.; Beskopylnyi, A. M.; Zlotin, S. G.; Lukyanov, O. A.; Zhulin, V. M. *Izv. Akad. Nauk. SSSR, Ser. Khim.* **1980**, *11*, 2668. (c) Zavarzin, I. V.; Zhulin, V. M.; Yarovenko, V. N.; Krayushkin, M. M. *Izv. Akad. Nauk SSSR, Ser. Khim.* **1988**, *5*, 1168. (d) Klaubert, D. H.; Sellstedt, J. H.; Guinosso, C. J.; Bell, S. C.; Capetola, R. J. *J. Med. Chem.* **1981**, *24*, 748.

(130) Carpenter, W. R. *J. Org. Chem.* **1962**, *27*, 2085.

(131) (a) Finnegan, W. G.; Henry, R. A.; Lofquist, R. *J. Am. Chem. Soc.* **1958**, *80*, 3908. (b) Jursic, E.; Zdravkovski, Z. *THEOCHEM* **1994**, *118*, 11.

(132) (a) Titova, I. E.; Poplavskii, V. S.; Koldobskii, G. I.; Ostrovskii, V. A.; Nikolaev, V. D.; Erusalimskii, G. B. *Khim. Geterosikl. Soedin.* **1986**, *8*, 1086. (b) Ostrovskii, V. A.; Poplavskii, V. S.; Koldobskii, G. I.; Erusalimskii, G. B. *Khim. Geterosikl. Soedin.* **1992**, *9*, 1214.

(133) Demko, Z. P.; Sharpless, K. B. *Org. Lett.* **2001**, *3*, 4091.

(134) Himo, F.; Demko, Z. P.; Noodleman, L.; Sharpless, K. B. *J. Am. Chem. Soc.* **2002**, *124*, 12210.

(135) (a) Gallante, R. J. U.S. Patent 5,502,191, 1995. (b) Tokuhara, G.; Yamaguchi, T.; Iwasaki, T. WO Patent 1996-37481, 1996.

(136) Demko, Z. P.; Sharpless, K. B. *J. Org. Chem.* **2001**, *66*, 7945.

(137) Himo, F.; Demko, Z. P.; Noodleman, L.; Sharpless, K. B. *J. Am. Chem. Soc.* **2003**, *125*, 9983.

(138) McCord, J. M.; Fridovich, I. *Free Radical Biol. Med.* **1988**, *5*, 363.

(139) (a) Deng, H.-X.; Hentati, A.; Tainer, J. A.; Iqbal, Z.; Cayabyab, A.; Hung, W.-Y.; Getzoff, E. J.; Hu, P.; Herzfeldt, B.; Roos, R. P.; Wagner, C.; Deng, G.; Soriano, E.; Smith, C.; Parge, H. E.; Ahmed, A.; Roses, A. D.; Hallewell, R. A.; Pericak-Vance, M. A.; Siddique, T. *Science* **1993**, *261*, 1047. (b) Fridovich, I. *Annu. Rev. Biochem.* **1995**, *64*, 97. (c) Fridovich, I. *J. Biol. Chem.* **1997**, *272*, 18515. (d) Miller, A.-F.; Sorkin, D. L. *Comments Mol. Cell. Biophys.* **1997**, *9*, 1.

(140) (a) McCord, J. M.; Fridovich, I. *J. Biol. Chem.* **1969**, *244*, 6049. (b) Yost, F. J.; Fridovich, I. *J. Biol. Chem.* **1976**, *248*, 4905. (c) Keele, B. B., Jr.; McCord, J. M.; Fridovich, I. *J. Biol. Chem.* **1970**, *245*, 6176. (d) Youn, H.-D.; Kim, E.-J.; Roe, J.-H.; Hah, Y. C.; Kang, S.-O. *Biochem. J.* **1996**, *318*, 889.

(141) Deng, H.-X.; Tainer, J. A.; Mitsumoto, H.; Ohnishi, A.; Hung, W.-Y.; Zhao, Y.; Juneja, T.; Hentati, A.; Siddique, T. *Hum. Mol. Genet.* **1995**, *4*, 1113.

(142) Borgstahl, G. E. O.; Parge, H. E.; Hickey, M. J.; Johnson, M. J.; Boissinot, M.; Hallewell, R. A.; Lepock, J. R.; Cabelli, D. E.; Tainer, J. A. *Biochemistry* **1996**, *35*, 4287.

(143) (a) Land, W.; Zweier, J. L. *Transplant. Proc.* **1997**, *29*, 2567. (b) Ambrosone, C. B.; Freudenheim, J. L.; Thompson, P. A.; Bowman, E.; Vena, J. E.; Marshall, J. R.; Graham, S.; Laughlin, R.; Nemoto, T.; Shields, P. G. *Cancer Res.* **1999**, *59*, 602. (c) Mitrunen, K.; Silanpaa, P.; Kataja, V.; Eskelinen, M.; Kosma, V. M.; Benhamou, S.; Uusitupa, M.; Hirvonen, A. *Carcinogenesis* **2001**, *22*, 827.

(144) Fisher, C. L.; Chen, J.-L.; Li, J.; Bashford, D.; Noodleman, L. *J. Phys. Chem.* **1996**, *100*, 13498.

(145) Konecny, R.; Li, J.; Fisher, C. L.; Dillet, V.; Bashford, D.; Noodleman, L. *Inorg. Chem.* **1999**, *38*, 940.

(146) (a) Lavelle, F.; McAdam, M. E.; Fielden, E. M.; Roberts, P. B.; Puget, K.; Michelson, A. M. *Biochem. J.* **1977**, *161*, 3. (b) McAdam, M. E.; Fox, R. A.; Lavelle, F.; Fielden, E. M. *Biochem. J.* **1977**, *165*, 71.

(147) (a) Bull, C.; Niederhoffer, E. C.; Yoshida, T.; Fee, J. A. *J. Am. Chem. Soc.* **1991**, *113*, 4069. (b) Cabelli, D. E.; Guan, Y.; Leveque, V.; Hearn, A. S.; Tainer, J. A.; Nick, H. S.; Silverman, D. N. *Biochemistry* **1999**, *38*, 11686. (c) Hearn, A. S.; Stroupe, M. E.; Cabelli, D. E.; Lepock, J. R.; Tainer, J. A.; Nick, H. S.; Silverman, D. N. *Biochemistry* **2001**, *40*, 12051. (d) Hearn, A. S.; Tu, C.; Nick, H. S.; Silverman, D. N. *J. Biol. Chem.* **1999**, *274*, 24457.

(148) Hsu, J.-L.; Hsieh, Y.; Tu, C.; O'Connor, D.; Nick, H. S.; Silverman, D. N. *J. Biol. Chem.* **1996**, *271*, 17687.

(149) Whittaker, M. M.; Whittaker, J. W. *Biochemistry* **1996**, *35*, 6762.

(150) Whittaker, M. M.; Whittaker, J. W. *Biochemistry* **1997**, *36*, 8923.

(151) Guan, Y.; Hickey, M. J.; Borgstahl, G. E. O.; Hallewell, R. A.; Lepock, J. R.; O'Connor, D.; Hsieh, Y.; Nick, H. S.; Silverman, D. N.; Tainer, J. A. *Biochemistry* **1998**, *37*, 4722.

(152) Hsieh, Y.; Guan, Y.; Tu, C.; Bratt, P. J.; Angerhofer, A.; Lepock, J. R.; Hickey, M. J.; Tainer, J. A.; Nick, H. S.; Silverman, D. N. *Biochemistry* **1998**, *37*, 4731.

(153) Edwards, R. A.; Whittaker, M. M.; Whittaker, J. W.; Baker, E. N.; Jameson, G. B. *Biochemistry* **2001**, *40*, 4622.

(154) Hearn, A. S.; Stroupe, M. E.; Cabelli, D. E.; Ramilo, C. A.; Luba, J. P.; Tainer, J. A.; Nick, H. S.; Silverman, D. N. *Biochemistry* **2003**, *42*, 2781.
(155) Silverman, D. N., private communication.
(156) (a) Vance, C. K.; Miller, A.-F. *Biochemistry* **2001**, *40*, 13079. (b) Vance, C. K.; Miller, A.-F. *J. Am. Chem. Soc.* **1998**, *120*, 461. (c) Yikilmaz, E.; Xie, J.; Brunold, T. C.; Miller, A.-F. *J. Am. Chem. Soc.* **2002**, *124*, 3482.
(157) Bull, C.; Fee, J. A. *J. Am. Chem. Soc.* **1985**, *107*, 3295.
(158) Schwartz, A. L.; Yikilmaz, E.; Vance, C. K.; Vathyam, S.; Koder, R. L., Jr.; Miller, A.-F. *J. Inorg. Biochem.* **2000**, *80*, 247.
(159) Bannister, J. V.; Bannister, W. H.; Rotilio, G. *CRC Crit. Rev. Biochem.* **1987**, *22*, 111.
(160) (a) Osman, R.; Basch, H. *J. Am. Chem. Soc.* **1984**, *106*, 5710. (b) Bertini, I.; Lepori, A.; Luchinat, C.; Turano, P. *Inorg. Chem.* **1991**, *30*, 3363. (c) Djinovic-Carugo, K.; Battistoni, A.; Carri, M. T.; Polticelli, F.; Desideri, A.; Rotilio, G.; Coda, A.; Bolognesi, M. *FEBS Lett.* **1994**, *349*, 93. (d) Djinovic-Carugo, K.; Polticelli, F.; Desideri, A.; Rotilio, G.; Wilson, K. S.; Bolognesi, M. *J. Mol. Biol.* **1994**, *240*, 179.
(161) (a) Klug-Roth, D.; Fridovich, I.; Rabani, J. *J. Am. Chem. Soc.* **1973**, *95*, 2786. (b) Fielden, E. M.; Roberts, P. B.; Bray, R. C.; Lowe, D. J.; Mautner, G. N.; Rotilio, G.; Calabrese, L. *Biochem. J.* **1974**, *499*, 139.
(162) Fee, J. A.; Bull, C. *J. Biol. Chem.* **1986**, *261*, 13000.
(163) (a) Ogihara, N. L.; Parge, H. E.; Hart, P. J.; Weiss, M. S.; Goto, J. J.; Crane, B. R.; Tsang, J.; Slater, K.; Roe, J. A.; Valentine, J. S.; Eisenberg, D.; Tainer, J. A. *Biochemistry* **1996**, *35*, 2316. (b) Murphy, L. M.; Strange, R. W.; Hasnain, S. S. *Structure* **1997**, *5*, 371.
(164) Tanokura, M. *Biochim. Biophys. Acta* **1983**, *742*, 576.
(165) Ellerby, L. M.; Cabelli, D. E.; Graden, J. A.; Valentine, J. S. *J. Am. Chem. Soc.* **1996**, *118*, 6556.
(166) Beinert, H. *FASEB J.* **1990**, *4*, 2483.
(167) (a) Lovenberg, W., Ed. *Iron−Sulfur Proteins*; Academic Press: New York, 1973; 1977; Vols. I, II, and III. (b) *Advances in Inorganic Chemistry*; Cammack, R., Ed.; Academic Press: New York, 1992; Vol. 38.
(168) (a) Mitchell, P. J. *Biochemistry* **1985**, *24*, 1. (b) Han, A. L.; Yagi, T.; Hatefi, Y. *Arch. Biochem. Biophys.* **1989**, *275*, 166.
(169) Spiro, T. G., Ed. *Iron Sulfur Proteins*; Academic Press: New York, 1981.
(170) Crane, B. R.; Getzoff, E. D. *Curr. Opin. Struct. Biol.* **1996**, *6*, 744.
(171) Crane, B. R.; Siegel, L. M.; Getzoff, E. G. *Science* **1995**, *270*, 59.
(172) Adams, M. W. W.; Stiefel, E. I. *Science* **1998**, *282*, 1842.
(173) (a) Stacey, G.; Burris, R. H.; Evans, H. J. *Biological Nitrogen Fixation*; Chapman and Hall: New York, 1992. (b) Steifel, E. I.; Concouvanis, D.; Newton, W. E. *Molydenum Enzymes, Cofactors, and Model Systems*; American Chemical Society: Washington, DC, 1993. (c) Holm, R. H.; Kennepohl, P.; Solomon, E. I. *Chem. Rev.* **1996**, *96*, 2239.
(174) (a) Burgess, B. K.; Lowe, D. J. *Chem. Rev.* **1996**, *96*, 2983 and references therein. (b) Ferguson, S. J. *Curr. Opin. Chem. Biol.* **1998**, *2*, 182.
(175) (a) Tennison, S. R. In *Catalytic Ammonia Synthesis Fundamentals and Practice*; Jennings, J. R., Ed.; Plenum Press: New York, 1991; p 303. (b) Howard, J. B.; Rees, J. B. *Chem. Rev.* **1996**, *96*, 2965. (c) Rawls, R. L. *Chem. Eng. News* **1951**, *29*, 9. (d) Sellmann, D.; Sutter, J. *Acc. Chem. Res.* **1997**, *30*, 460.
(176) Eady, R. R. *Chem. Rev.* **1996**, *96*, 3013.
(177) (a) Rees, D. C. *Curr. Opin. Struct. Biol.* **1993**, *3*, 921. (b) Rees, D. C.; Chan, M. K.; Kim, J. *Adv. Inorg. Chem.* **1993**, *40*, 89. (c) Smith, B. E. *Adv. Inorg. Chem.* **1999**, *47*, 159.
(178) Peters, J. W.; Stowell, M. H. B.; Soltis, S. M.; Finnegan, M. G.; Johnson, M. K.; Rees, D. C. *Biochemistry* **1997**, *36*, 1181.
(179) (a) Thorneley, R. N. F.; Lowe, D. In *Molybdenum Enzymes*; Spiro, T. G., Ed.; Wiley-Interscience: New York, 1985. (b) Thorneley, R. N. F.; Lowe, D. *J. Biol. Inorg. Chem.* **1996**, *1*, 576.
(180) (a) Huynh, B. H.; Munck, E.; Orme-Johnson, W. H. *Biochim. Biophys. Acta* **1979**, *527*, 192. (b) Huynh, B. H.; Henzel, M. T.; Christner, J. A.; Zimmermann, R.; Orme-Johnson, W. H.; Munck, E. *Biochim. Biophys. Acta* **1980**, *623*, 124.
(181) Johnson, M. K.; Thomson, A. J.; Robinson, A. E.; Smith, B. E. *Biochim. Biophys. Acta* **1981**, *671*, 61.
(182) (a) Kim, J.; Rees, D. C. *Nature* **1992**, *360*, 553. (b) Kim, J.; Rees, D. C. *Science* **1992**, *257*, 1677. (c) Chan, M. K.; Kim, J.; Rees, D. C. *Science* **1993**, *260*, 792. (d) Georgiadis, M. M.; Komiya, H.; Woo, D.; Kornuc, J. J.; Rees, D. C. *Science* **1992**, *257*, 1653. (e) Kim, J.; Woo, D.; Rees, D. C. *Biochemistry* **1993**, *32*, 7104. (f) Bolin, J. T.; Ronco, A. E.; Morgan, T. V.; Mortenson, L. E.; Xuong, N. *Proc. Natl. Acad. Sci. U. S.A.* **1993**, *90*, 1078. (g) Mayer, S. M.; Lawson, D. M.; Gormal, C. A.; Roe, S. M.; Smith, B. E. *J. Mol. Biol.* **1999**, *292*, 871. (h) Schindelin, N.; Kisker, C.; Schlessman, J. L.; Howard, J. B.; Rees, D. C. *Nature* **1997**, *387*, 370. (i) Strop, P.; Takahara, P. M.; Chiu, H.-J.; Angove, H. C.; Burgess, B. K.; Rees, D. C. *Biochemistry* **2001**, *40*, 651.
(183) (a) Zimmermann, R.; Munck, E.; Brill, W. J.; Shah, V. K.; Henzyl, M. T.; Rawlings, J.; Orme-Johnson, W. H. *Biochim. Biophys. Acta* **1978**, *537*, 185. (b) Surerus, K. K.; Hendrich, M. P.; Christie, P. D.; Rottgardt, D.; Orme-Johnson, W. H.; Munck, E. *J. Am. Chem. Soc.* **1992**, *114*, 8579.
(184) Lee, H.-I.; Hales, B. J.; Hoffman, B. M. *J. Am. Chem. Soc.* **1997**, *119*, 11395.
(185) True, A. E.; Nelson, M. J.; Venters, R. A.; Orme-Johnson, W. H.; Hoffman, B. M. *J. Am. Chem. Soc.* **1988**, *110*, 1935.
(186) Yoo, S. J.; Angove, H. C.; Papaefthymiou, V.; Burgess, B. K.; Munck, E. *J. Am. Chem. Soc.* **2000**, *122*, 4926.
(187) MacDonnell, F. M.; Rohlandt-Senge, K.; Ellison, J. J.; Holm, R. H.; Power, P. P. *Inorg. Chem.* **1995**, *34*, 1815.
(188) Einsle, O.; Teczan, F. A.; Andrade, S. L. A.; Schmid, B.; Yoshida, M.; Howard, J. B.; Rees, D. C. *Science* **2002**, *297*, 1696.
(189) Lee, H.-I.; Benton, P. M. C.; Laryukhin, M.; Igarashi, R. Y.; Dean, D. R.; Seefeldt, L. C.; Hoffman, B. M. *J. Am. Chem. Soc.* **2003**, *125*, 5604.
(190) Plass, W. *THEOCHEM* **1994**, *315*, 53.
(191) Deng, H.; Hoffmann, R. *Angew. Chem., Int. Ed. Engl.* **1993**, *32*, 1062.
(192) (a) Stavrev, K. K.; Zerner, M. C. *Chem.-Eur. J.* **1996**, *2*, 83. (b) Stavrev, K. K.; Zerner, M. C. *Theor. Chim. Acta* **1997**, *96*, 141. (c) Stavrev, K. K.; Zerner, M. C. *Int. J. Quantum Chem.* **1998**, *70*, 1159.
(193) (a) Dance, I. *Aust. J. Chem.* **1994**, *47*, 979. (b) Dance, I. *Chem. Commun.* **1997**, 165. (c) Dance, I. *Chem. Commun.* **1998**, 523. (d) Dance, I. *J. Biol. Inorg. Chem.* **1996**, *1*, 581.
(194) Siegbahn, P. E. M.; Westerberg, J.; Svensson, M.; Crabtree, R. H. *J. Phys. Chem. B* **1998**, *102*, 1615.
(195) Barriere, F.; Pickett, C. J.; Talarmin, J. *Polyhedron* **2001**, *20*, 27.
(196) (a) Rod, T. H.; Hammer, B.; Nørskov, J. K. *Phys. Rev. Lett.* **1999**, *82*, 4054. (b) Rod, T. H.; Logadottir, A.; Nørskov, J. K. *J. Chem. Phys.* **2000**, *112*, 5343. (c) Rod, T. H.; Nørskov, J. K. *J. Am. Chem. Soc.* **2000**, *122*, 12751.
(197) Szilagyi, R. K.; Musaev, D. K.; Morokuma, K. *Inorg. Chem.* **2001**, *40*, 766.
(198) (a) Durrant, M. C. *Inorg. Chem. Commun.* **2001**, *4*, 60. (b) Durrant, M. C. *Biochem. J.* **2001**, *355*, 569. (c) Durrant, M. C. *Biochemistry* **2002**, *41*, 13946. (d) Durrant, M. C. *Biochemistry* **2002**, *41*, 13934.
(199) (a) Lovell, T.; Li, J.; Case, D. A.; Noodleman, L. *J. Am. Chem. Soc.* **2002**, *124*, 4546. (b) Lovell, T.; Torres, R. A.; Han, W.-G.; Liu, T.; Case, D. A.; Noodleman, L. *Inorg. Chem.* **2002**, *41*, 5744. (c) Lovell, T.; Li, J.; Case, D. A.; Noodleman, L. *J. Biol. Inorg. Chem.* **2002**, *7*, 735. (d) Lovell, T.; Liu, T.; Case, D. A.; Noodleman, L. *J. Am. Chem. Soc.* **2003**, *125*, 8377.
(200) Ullmann, G. M.; Noodleman, L.; Case, D. A. *J. Biol. Inorg. Chem.* **2002**, *7*, 623.
(201) (a) Hinnemann, B.; Norskov, J. K. *J. Am. Chem. Soc.* **2003**, *125*, 1466. (b) Dance, I. *Chem. Commun.* **2003**, 324.
(202) O'Donnell, M. J.; Smith, B. E. *Biochem. J.* **1978**, *173*, 831.
(203) Lee, H.-I.; Thrasher, K. S.; Dean, D. R.; Newton, W. E.; Hoffman, B. M. *Biochemistry* **1998**, *37*, 13370.
(204) (a) Yandulov, D. V.; Schrock, R. R. *Science* **2003**, *301*, 76. (b) Leigh, G. J. *Science* **2003**, *301*, 55.
(205) Benton, P. M. C.; Laryukhin, M.; Mayer, S. W. M.; Hoffman, B. M.; Dean, D. R.; Seefeldt, L. C. *Biochemistry* **2003**, *42*, 9102.
(206) Greenwood, N. N.; Earnshaw, A. *Chemistry of the Elements*, 2nd ed.; Oxford University Press: New York, 2002.
(207) Rosenzweig, A. C.; Frederick, C. A.; Lippard, S. J.; Nordlund, P. *Nature* **1993**, *366*, 537.
(208) Reichard, P. *Science* **1993**, *260*, 1773.
(209) Stubbe, J.; van der Donk, W. A. *Chem. Rev.* **1998**, *98*, 705.
(210) Gütlich, P.; Ensling, J. *Inorganic Electronic Structure and Spectroscopy*; John Wiley and Sons: New York, 1999; Vol. 1, pp 161−212.
(211) Gütlich, P.; Link, R.; Trautwein, A. X.; *Mössbauer Spectroscopy and Transition Metal Chemistry*; Springer-Verlag: Berlin, 1978.
(212) Huynh, B.-H.; Bollinger, J. M., Jr.; Edmondson, D. E. In *Spectroscopic Methods in Bioinorganic Chemistry*; Solomon, E. I., Hodgson, K. O., Eds.; ACS Symposium Series 692; Oxford University Press: New York, 1998; pp 403−422.
(213) (a) Noodleman, L.; Norman, J. G., Jr.; Osbourne, J. H.; Aizan, A.; Case, D. A. *J. Am. Chem. Soc.* **1985**, *107*, 3418. (b) Nemykin, V. N.; Kobayashi, N.; Chenii, V. Y.; Belksy, V. K. *Eur. J. Inorg. Chem.* **2001**, *3*, 733. (c) Ziegler, T. *Chem. Rev.* **1991**, *91*, 651 and references therein. (d) Liu, T.; Case, D. A.; Noodleman, L., manuscript in preparation. (e) Martínez-Pinedo, G.; Schderdtfeger, P.; Caurier, E.; Langanke, K.; Nazarewicz, W.; Söhnnel, T. *Phys. Rev. Lett.* **2001**, *87*, 062701. (f) Lauer, S.; Marathe, V. R.; Trautwein, A. X. *Phys. Rev. A* **1979**, *19*, 1852. (g) Dufek, P.; Blaha, P.; Schwarz, K. *Phys. Rev. Lett.* **1995**, *75*, 3545. (h) Lovell, T.; Li, J.; Noodleman, L. *Inorg. Chem.* **2001**, *40*, 5267. (i) Lovell, T.; Li, J.; Noodleman, L. *J. Biol. Inorg. Chem.* **2002**, *7*, 799. (j) Kuramochi, H.; Case, D. A.; Noodleman, L. *J. Am. Chem. Soc.* **1997**, *119*, 11442. (k) Liu, T.; Lovell, T.; Ullmann, G. M.; Case, D. A.; Noodleman, L. *Inorg. Chem.*, submitted. (l) Zhang, Y.; Mao, J.; Oldfield, E. *J. Am. Chem. Soc.* **2002**, *124*, 7829. (m) Neese,

F. *Inorg. Chim. Acta* **2002**, *337*, 181. (n) Liu, T.; Lovell, T.; Han, W.-G.; Noodleman, L. *Inorg. Chem.* **2003**, *42*, 5244.

(214) (a) Kurtz, D. M., Jr. *Chem. Rev.* **1990**, *90*, 585. (b) Wallar, B. J.; Lipscomb, J. D. *Chem. Rev.* **1996**, *96*, 2625. (c) Stubbe, J.; van der Donk, W. A. *Chem. Biol.* **1995**, *2*, 793.

(215) Baik, M.-H.; Newcomb, M.; Friesner, R. A.; Lippard, S. J. *Chem. Rev.* **2003**, *103*, 2385.

(216) (a) Hanson, R. S.; Hanson, T. E. *Microbiol. Rev.* **1996**, *60*, 439. (b) Anthony, C. In *Biology of Methylotrophs*; Goldberg, I., Rokem, J. S., Eds.; Butterworth-Heinemann: Stoneham, MA, 1991.

(217) Siegbahn, P. E. M.; Blomberg, M. R. A. *Chem. Rev.* **2000**, *100*, 421.

(218) (a) Yoshizawa, K. *Coord. Chem. Rev.* **2002**, *226*, 251. (b) Yoshizawa, K.; Suzuki, A.; Shiota, Y.; Yamabe, T. *Bull. Chem. Soc. Jpn.* **2000**, *73*, 815. (c) Yoshizawa, K.; Ohta, T.; Yamabe, T.; Hoffmann, R. *J. Am. Chem. Soc.* **1997**, *119*, 12311. (d) Shiota, Y.; Yoshizawa, K. *J. Am. Chem. Soc.* **2000**, *122*, 12317. (e) Yoshizawa, K.; Shiota, Y.; Yamabe, T. *Chem.-Eur. J.* **1997**, *3*, 1160. (f) Yoshizawa, K.; Yamabe, T.; Hoffmann, R. *New J. Chem.* **1997**, *21*, 151. (g) Yoshizawa, K.; Hoffmann, R. *Inorg. Chem.* **1996**, *35*, 2409. (h) Yoshizawa, K.; Yokomichi, Y.; Shiota, Y.; Ohta, T.; Yamabe, T. *Chem. Lett.* **1997**, 587. (i) Yoshizawa, K. *J. Biol. Inorg. Chem.* **1998**, *3*, 318. (j) Yoshizawa, K.; Shiota, Y.; Yamabe, T. *J. Am. Chem. Soc.* **1998**, *120*, 564. (k) Yoshizawa, K.; Ohta, T.; Yamabe, T. *Bull. Chem. Soc. Jpn.* **1998**, *71*, 1899. (l) Yoshizawa, K. *J. Inorg. Biochem.* **2000**, *78*, 23. (m) Yoshizawa, K. *J. Organomet. Chem.* **2001**, *635*, 100.

(219) (a) Basch, H.; Mogi, K.; Musaev, D. G.; Morokuma, K. *J. Am. Chem. Soc.* **1999**, *121*, 7249. (b) Basch, H.; Musaev, D. G.; Morokuma, K. *J. Phys. Chem. B* **2001**, *105*, 8452. (c) Torrent, M.; Mogi, K.; Basch, H.; Musaev, D. G.; Morokuma, K. *J. Phys. Chem. B* **2001**, *105*, 8616. (d) Torrent, M.; Musaev, D. G.; Morokuma, K.; Basch, H. *J. Phys. Chem. B* **2001**, *105*, 4453. (e) Basch, H.; Musaev, D. G.; Mogi, K.; Morokuma, K. *J. Phys. Chem. A* **2001**, *105*, 3615. (f) Torrent, M.; Musaev, D. G.; Morokuma, K. *J. Phys. Chem. B* **2001**, *105*, 322. (g) Musaev, D. G.; Basch, H.; Morokuma, K. *J. Am. Chem. Soc.* **2002**, *124*, 4135.

(220) (a) Siegbahn, P. E. M.; Crabtree, R. H. *J. Am. Chem. Soc.* **1997**, *119*, 3103. (b) Siegbahn, P. E. M. *Inorg. Chem.* **1999**, *38*, 2880. (c) Siegbahn, P. E. M. *Chem. Phys. Lett.* **2002**, *351*, 311. (d) Siegbahn, P. E. M.; Crabtree, R. H. *Struct. Bonding* **2000**, *97*, 125. (e) Siegbahn, P. E. M.; Crabtree, R. H.; Nordlund, P. *J. Biol. Inorg. Chem.* **1998**, *3*, 314. (f) Blomberg, M. R. A.; Siegbahn, P. E. M. *J. Phys. Chem. B* **2001**, *105*, 9375. (g) Siegbahn, P. E. M. *J. Biol. Inorg. Chem.* **2001**, *6*, 27.

(221) (a) Ambundo, E. A.; Friesner, R. A.; Lippard, S. J. *J. Am. Chem. Soc.* **2002**, *124*, 8770. (b) Friesner, R. A.; Baik, M.-H.; Gherman, B. F.; Guallar, V.; Wirstam, M.; Murphy, R. B.; Lippard, S. J. *Coord. Chem. Rev.* **2003**, *238*−*239*, 267. (c) Baik, M.-H.; Lee, D.; Friesner, R. A.; Lippard, S. J. *Isr. J. Chem.* **2001**, *41*, 173. (d) Dunietz, B. D.; Beachy, M. D.; Cao, Y. X.; Whittington, D. A.; Lippard, S. J.; Friesner, R. A. *J. Am. Chem. Soc.* **2000**, *122*, 2828. (e) Gherman, B. F.; Dunietz, B. D.; Whittington, D. A.; Lippard, S. J.; Friesner, R. A. *J. Am. Chem. Soc.* **2001**, *123*, 3836. (f) Friesner, R. A.; Dunietz, B. D. *Acc. Chem. Res.* **2001**, *34*, 351. (g) Guallar, V.; Gherman, B. F.; Lippard, S. J.; Friesner, R. A. *Curr. Opin. Chem. Biol.* **2002**, *6*, 236. (h) Guallar, V.; Gherman, B. F.; Miller, W. H.; Lippard, S. J.; Friesner, R. A. *J. Am. Chem. Soc.* **2002**, *124*, 3377. (i) Baik, M.-H.; Gherman, B. F.; Friesner, R. F.; Lippard, S. J. *J. Am. Chem. Soc.* **2002**, *124*, 14608.

(222) Lovell, T.; Han, W.-G.; Liu, T.; Noodleman, L. *J. Am. Chem. Soc.* **2002**, *124*, 5890.

(223) (a) Liu, K. E.; Valentine, A. M.; Wang, D.; Huynh, B. H.; Edmondson, D. E.; Salifoglou, A.; Lippard, S. J. *J. Am. Chem. Soc.* **1995**, *117*, 10174. (b) Liu, K. E.; Wang, D.; Huynh, B. H.; Edmondson, D. E.; Salifoglou, A.; Lippard, S. J. *J. Am. Chem. Soc.* **1994**, *116*, 7465. (c) Lee, S.-K.; Fox, B. G.; Froland, W. A.; Lipscomb, J. D.; Munck, E. *J. Am. Chem. Soc.* **1993**, *115*, 6450. (d) Shu, L.; Nesheim, J. C.; Kauffmann, K.; Munck, E.; Lipscomb, J. D.; Que, L., Jr. *Science* **1997**, *275*, 515. (e) Hsu, H.-F.; Dong, Y.; Shu, L.; Young, V. G., Jr.; Que, L., Jr. *J. Am. Chem. Soc.* **1999**, *121*, 5230.

(224) (a) Noodleman, L. *J. Chem. Phys.* **1981**, *74*, 5737. (b) McGrady, J. E.; Stranger R.; Lovell, T. *J. Phys. Chem. A* **1997**, *101*, 6265.

(225) Lovell, T.; Han, W.-G.; Noodleman, L., unpublished results.

(226) Sjöberg, B. M. *Struct. Bonding* **1997**, *88*, 139.

(227) Sturgeon, B. E.; Burdi, D.; Chen, S.; Huynh, B. H.; Edmondson, D. E.; Stubbe, J.; Hoffman, B. M. *J. Am. Chem. Soc.* **1996**, *118*, 7551.

(228) (a) Bollinger, J. M., Jr.; Edmondson, D. E.; Huynh, B. H.; Filley, J.; Norton, J. R.; Stubbe, J. *Science* **1991**, *253*, 292. (b) Bollinger, J. M., Jr.; Stubbe, J.; Huynh, B. H.; Edmondson, D. E. *J. Am. Chem. Soc.* **1991**, *113*, 6289. (c) Ravi, N.; Bollinger, J. M., Jr.; Huynh, B. H.; Edmondson, D. E.; Stubbe, J. *J. Am. Chem. Soc.* **1994**, *116*, 8007. (d) Bollinger, J. M., Jr.; Tong, W. H.; Ravi, N.; Huynh, B. H.; Edmondson, D. E.; Stubbe, J. *J. Am. Chem. Soc.* **1994**, *116*, 8015; **1994**, *116*, 8024.

(229) (a) Nordlund, P.; Sjoberg, B. M.; Eklund, H. *Nature* **1990**, *345*, 593. (b) Nordlund, P.; Eklund, H. *J. Mol. Biol.* **1993**, *232*, 123. (c) Nordlund, P.; Eklund, H. *Curr. Opin. Struct. Biol.* **1995**, *5*, 758. (d) Logan, D. T.; Su, X. D.; Åberg, A.; Regnström, K.; Hajdu, J.; Eklund, H.; Nordlund, P. *Structure* **1996**, *4*, 1053.

(230) (a) Burdi, D.; Sturgeon, B. E.; Tong, W. H.; Stubbe, J.; Hoffman, B. M. *J. Am. Chem. Soc.* **1996**, *118*, 281. (b) Veselov, A.; Scholes, C. P. *Inorg. Chem.* **1996**, *35*, 3702. (c) Willems, J. P.; Lee, H. I.; Burdi, D.; Doan, P. E.; Stubbe, J.; Hoffman, B. M. *J. Am. Chem. Soc.* **1997**, *119*, 9816. (d) Riggs-Gelasco, P. J.; Shu, L.; Chen, S.; Burdi, D.; Huynh, B. H.; Que, L., Jr.; Stubbe, J. *J. Am. Chem. Soc.* **1998**, *120*, 849. (e) Burdi, D.; Willems, J. P.; Riggs-Gelasco, P. J.; Antholine, W. E.; Stubbe, J.; Hoffman, B. M. *J. Am. Chem. Soc.* **1998**, *120*, 12910.

(231) Siegbahn, P. E. M.; Eriksson, L.; Himo, F.; Pavlov, M. *J. Phys. Chem. B* **1998**, *102*, 10622.

(232) Han, W.-G.; Lovell, T.; Liu, T.; Noodleman, L. *Inorg. Chem.* **2003**, *42*, 2751.

(233) Siegbahn, P. E. M. *Q. Rev. Biophys.* **2003**, *36*, 91.

(234) Han, W.-G.; Lovell, T.; Liu, T.; Noodleman, L. *Inorg. Chem.* **2004**, *43*, 613.

(235) Dong, Y.; Fujii, H.; Hendrich, M. P.; Leising, R. A.; Pan, G.; Randall, C. R.; Wilkinson, E. C.; Zang, Y.; Que, L., Jr.; Fox, B. G.; Kauffmann, K.; Münck, E. *J. Am. Chem. Soc.* **1995**, *117*, 2778.

(236) Dong Y.; Que, L., Jr. *J. Am. Chem. Soc.* **1995**, *117*, 11377.

(237) Ghosh, A.; Almlöf, J.; Que, L., Jr. *Angew. Chem., Int. Ed. Engl.* **1996**, *35*, 770.

(238) Skulan, A. J.; Hanson, M. A.; Hsu, H.; Que, L., Jr.; Solomon, E. I. *J. Am. Chem. Soc.* **2003**, *125*, 7344.

(239) Kuhn, H.; Borngraber, S. In *Lipoxygenases and Their Metabolites*; Nigam, S., Pace-Asciak, C. R., Eds.; Plenum: New York, 1999; pp 5−28.

(240) (a) Siedow, J. N. *Annu. Rev. Plant Physiol. Plant Mol. Biol.* **1991**, *41*, 145. (b) Fort-Hutchinson, A. W.; Gresser, M.; Young, R. N. *Annu. Rev. Biochem.* **1994**, *63*, 383.

(241) (a) Boyington, J. C.; Gaffney, B. J.; Amzel, L. M. *Science* **1993**, *260*, 1482. (b) Minor, W.; Steczko, J.; Stec, B.; Otwinowski, Z.; Bolin, J. T.; Walter, R.; Axelrod, B. *Biochemistry* **1996**, *35*, 10687.

(242) Skrzypczak-Jankun, E.; Amzel, L. M.; Kroa, B. A.; Funk, M. O. J. *Proteins: Struct., Funct., Genet.* **1997**, *29*, 15.

(243) Gillmor, S. A.; Villasenor, A.; Fletterick, R.; Sigal, E.; Browner, M. F. *Nat. Struct. Biol.* **1997**, *4*, 1003.

(244) (a) Pavlosky, M. A.; Solomon, E. I. *J. Am. Chem. Soc.* **1994**, *116*, 11610. (b) Pavolosky, M. A.; Zhang, Y.; Westre, T. E.; Gan, Q. F.; Pavel, E. G.; Campochiaro, C.; Hedman, B.; Hodgson, K. O.; Solomon, E. I. *J. Am. Chem. Soc.* **1995**, *117*, 4316. (c) Solomon, E. I.; Zhou, J.; Neese, F.; Pavel, E. G. *Chem. Biol.* **1997**, *4*, 795.

(245) (a) Zhang, Y.; Gan, Q. F.; Pavel, E. G.; Sigal, E.; Solomon, E. I. *J. Am. Chem.. Soc.* **1995**, *117*, 7422. (b) van der Heijdt, L. M.; Feiters, M. C.; Navaratnam, S.; Nolting, H. F.; Hermes, C.; Veldink, G. A.; Vliegenthar, J. F. G. *Eur. J. Biochem.* **1992**, *207*, 793. (c) Scarrow, R. C.; Trimitsis, M. G.; Buck, C. P.; Grove, G. N.; Cowling, R. A.; Nelson, M. J. *Biochemistry* **1994**, *33*, 15023.

(246) Borowski, T.; Krol, M.; Chruszcz, M.; Broclawik, E. *J. Phys. Chem. B* **2001**, *105*, 12212.

(247) Lehnert, N.; Solomon, E. I. *J. Biol. Inorg. Chem.* **2003**, *8*, 294.

(248) Schenk, G.; Neidig, M. L.; Zhou, J.; Holman, T. R.; Solomon, E. I. *Biochemistry* **2003**, *42*, 7294.

(249) (a) Glickman, M. H.; Klinman, J. P. *Biochemistry* **1995**, *34*, 14077. (b) Nelson, M. J.; Cowling, R. A.; Seitz, S. P. *Biochemistry* **1994**, *33*, 4966. (c) Kohen, A. K.; Klinman, J. P. *Acc. Chem. Res.* **1998**, *31*, 397.

(250) Corey, E. J.; Nagata, R. *J. Am. Chem. Soc.* **1987**, *109*, 8107.

(251) Nelson, M. J.; Seitz, S. P. *Curr. Opin. Struct. Biol.* **1994**, *4*, 878.

(252) Borowski, T.; Broclawik, E. *J. Phys. Chem. B* **2003**, *107*, 4639.

(253) Rostovtsev, V. V.; Green, L. G.; Fokin, V. V.; Sharpless, K. B. *Angew. Chem., Int. Ed.* **2002**, *41*, 2596.

(254) Lewis, W. G.; Green, L. G.; Grynszpan, F.; Radic, Z.; Carlier, P. R.; Taylor, P.; Finn, M. G.; Sharpless, K. B. *Angew. Chem., Int. Ed.* **2002**, *41*, 1053.

CR020625A